

# **Detection of coal fires in Xinjiang (China) using remote sensing techniques**

Chunqing Wang  
February 2002

# Detection of coal fires in Xinjiang (China) using remote sensing techniques

by

**Chunqing Wang**

Thesis submitted to the International Institute for Geo-information Science and Earth Observation in partial fulfilment of the requirements for the degree of Master of Science in Natural Hazard Studies.

Degree Assessment Board

Chairman: Dr. C.Pohl,

External examiner: Prof. S.B.Kroonenberg,

First Supervisor: Dr. B.Maathuis,

Second Supervisor: Dr. A.Prakash,

Member: Dr. P.M.van Dijk



**INTERNATIONAL INSTITUTE FOR GEO-INFORMATION SCIENCE AND EARTH OBSERVATION  
ENSCHEDÉ, THE NETHERLANDS**

## **Disclaimer**

**This document describes work undertaken as part of a programme of study at the International Institute for Geo-information science and earth observation. All views and opinions expressed therein remain the sole responsibility of the author, and do not necessarily represent those of the institute.**

## **Acknowledgements**

I would like to use this opportunity to express my grateful thanks to my organization, the State Bureau of Surveying and Mapping (SBSM), for giving me the permission and support to study in ITC, and very thanks to the Netherlands government to provide scholarship for my study in the Netherlands.

I deeply appreciate the efforts of my first supervisor, Dr. Ben Maathuis, for his patient supervision and editing my thesis writing. Very special thanks to my second supervisor, Dr. Anupma Prakash, who gave me some advice to my research work. And also I would like to give my thanks to Dr. Paul van Dijk and Dr. van Westen, they gave me supervise on geology and recommendation for joining the research team of detection of coal fires in Northern China, respectively.

The contributions of all staffs in Natural Hazards Studies Division and others in ITC are also worth my great thanks for their teaching and what they did for students.

Sincerely thanks to Chinese students in ITC, who gave me help on studying or living, and made me feel friendly to be here.

At last, my great thanks to my wife, Mrs. Xia Hong, who gave me a completely support the best one could. I cannot imagine that I could finish my study here if there were no spiritual encouragement and bearing housewifery from her. I would like to share the happiness with her at the moment.

## Abstract

Coal fires originate at the interface of the coal seams and the atmosphere and have both natural and man-made causes. It is estimated that mostly in the northern half of China up to 200 Mt ( $20^8$  tonnes) of high quality coal are lost every year and this contributes to a loss of coal resources, CO<sub>2</sub> as well as other greenhouse gasses related emissions and air pollution amongst others.

In order to detect the areas affected by coal fires use is made of multispectral ASTER (on-board of the Terra polar orbiting spacecraft) daytime and Landsat 7 ETM+ nighttime images, acquired over a coal fire affected area in Xinjiang. Using the higher resolution optical bands of ASTER in conjunction with the stereoscopic capability, the images facilitated the mapping of the regional geological setting, especially the identification of the synclinal structure in relation to the surface exposed coal seam layers marking its perimeter. Furthermore relevant coal mine related features, such as mine entrances and coal dumps could be identified. This analysis resulted in the identification of potential coal fire areas.

Apart from transforming the ASTER (bands 10-14) and ETM+ (band6, high and low gain) images to kinematic temperatures, in order to get an idea of the real surface temperatures for coal fire type identification, the thermal anomalies due to the actual coal fires were used for further statistical analysis. For both the daytime and nighttime subsets were analyzed to determine the extent of the coal fire affected areas using different confidence levels. Ground truth data was used for validation of the results.

The combined use of daytime ASTER with nighttime Landsat 7 ETM+ allowed for the identification of the actual coal fire areas within the study area. As the temperature anomalies are very subtle it proved to be important to have a good background on potential coal fire locations and these could be provided using the higher resolution visible and near infrared bands of ASTER.

# Table of Contents

## Acknowledgement

## Abstract

Chapter 1 Introduction .....	1
1.1 Background of coal fires .....	1
1.2 Coal fires in China .....	2
1.3 Spontaneous combustion of coal.....	3
1.4 Detection of coal fires .....	5
1.5 Objectives of this study.....	5
1.6 Introduction to the study area.....	6
1.7 Data used for the research .....	8
1.8 Methodology .....	10
1.9 Structure of the thesis.....	10
Chapter 2 Remote sensing methods used for the detection of coal fires .....	12
2.1 Introduction .....	12
2.2 Optical satellite data.....	13
2.3 Thermal satellite data .....	16
2.3.1 Thermal infrared data used in the study of coal fire affected areas.....	17
2.3.2 Temperature and emissivity.....	19
2.3.3 Surface temperature related to the coal fires .....	23
Chapter 3 Data acquisition and image processing .....	24
3.1 Data acquisition.....	24
3.1.1 ASTER data acquisition .....	24
3.1.2 Procedure of downloading ASTER data .....	26
3.2 Description of ASTER data sets .....	27
3.3 Image processing.....	28
3.3.1 Geometric correction and registration .....	28
3.3.2 Image enhancement .....	32
Chapter 4 Feature extraction and image fusion .....	39
4.1 Feature extraction.....	39
4.2 Image interpretation of geology, geomorphology, drainage network and infrastructure	41
4.3 Feature properties of coal fires.....	44
4.4 Calculating temperatures from Landsat7 ETM+ and ASTER TIR data .....	46
4.4.1 Method of temperature calculation from Landsat7 ETM+ band 6 data .....	47
4.4.2 Method of temperature calculation from ASTER TIR data .....	53
4.4.3 Temperature conversion from Landsat7 ETM+ band6 and ASTER TIR images ...	58

4.5 Quantitative methods of detecting coal fire areas .....	66
4.5.1 Statistical method .....	66
4.5.2 Combination method of statistics and probability analysis .....	76
4.6 Classification.....	79
4.6.1 Supervised classification .....	80
4.6.2 Unsupervised classification .....	81
Chapter 5 The accuracy assessment for the detection of coal fires.....	83
5.1 Factors affected the detection results of coal fires .....	83
5.2 Assumption .....	84
5.3 The approach of accuracy assessment for each site (sub-image) .....	85
5.4 The overall accuracy assessment.....	86
5.5 The field data needed for the accuracy assessment .....	87
Chapter 6 Conclusions and recommendations.....	88
6.1 Conclusions .....	88
6.2 Recommendations .....	90
References .....	92

## List of Figures

Figure 1.1 Map of Coal fires in Northern China.....	3
Figure 1.2 Spontaneous combustion of coal.....	4
Figure 1.3 Sketch map of the Kerjian coal fire area, the black clusters are surveyed coal fires. ....	7
Figure 1.4 Framework of Research Work.....	11
Figure 2.1 A combination of ASTER VNIR (a), SWIR (b), and anaglyph images (c) used in the interpretation of this study .....	15
Figure 2.2 Generalized diurnal radiant temperature variations for soils and rocks versus water.....	17
Figure 3.1 Flow chart of image processing.....	29
Figure 3.2 The overlay of five rectified ASTER images (007,008,173,013,037) registered with a Landsat7 ETM+ image together. The square marked area is the study area (unit: km). ....	32
Figure 3.3 The results of spatial enhancement, (a) original Landsat7 ETM+ image, (b) Adaptive filter enhancement, (c) Focal analysis enhancement, (d) Statistical filter enhancement.....	34
Figure 3.4 The results of radiometric enhancement. (a) original ASTER image, (b) enhancement of histogram equalization, (c) enhancement of noise reduction, (d) enhancement of LUT stretch, (e) enhancement of haze reduction, and (f) enhancement of brightness inversion. ....	37
Figure 3.5 The stereo display of study area. ....	37
Figure 3.6 Landsat7 ETM+ band 6 nighttime image, (a) low gain, (b) high gain. ....	38
Figure 3.7 The image enhanced sub-images of Landsat7 ETM+ band 6 nighttime low and high gain data. ....	38
Figure 4.1 (a) ASTER image of study area used for the feature extraction. ....	43
Figure 4.1 (b) Feature extraction of geological map of study area. ....	43
Figure 4.2 Potential coal mining areas extracted from an ASTER visual image. ....	46
Figure 4.3 The relation curve of DN <sub>s</sub> and radiance from Landsat7 ETM+ band6 low and high gain data. ....	49
Figure 4.4 Relation curve of DN <sub>s</sub> and surface temperatures for Landsat7 band 6 data, blue and magenta line are the curve of low gain and high gain data, respectively. ....	52
Figure 4.5 Relation between DN values and radiances of TIR bands .....	53
Figure 4.6 the relation curves of DN <sub>s</sub> and surface temperatures from ASTER TIR data. ....	57
Figure 4.7 The function of temperature conversion from Landsat7 ETM+ band 6 image.....	59
Figure 4.8 The temperature converted image from Landsat7 ETM+ band 6 nighttime low gain image, (a) and (b) are the original image and temperature converted image, (c) and (d) are the relative pixel information of DN <sub>s</sub> and temperatures, respectively. ....	60
Figure 4.9 The temperature converted sub-image (coal fire area) from Landsat7 ETM+ band 6 nighttime high gain image, (a) and (b) are the original image and temperature converted image (low gain), (c) and (d) are the relative pixel information of DN <sub>s</sub> and temperatures, respectively. ....	61
Figure 4.10 The function of temperature conversion from ASTER TIR data. ....	63
Figure 4.11 A temperature converted ASTER TIR image, (a) the original image, (b) the temperature converted image, (c) and (d) are the relative pixel information of DN <sub>s</sub> and temperatures for band13, respectively.....	64

Figure 4.12 A temperature converted sub-image, (a) the original image, (b) the temperature converted image, (c) and (d) are the relative pixel information of DNs and temperatures for band13, respectively (this image was acquired in August, 2001). .....	65
Figure 4.13 The sub-image of Landsat7 ETM+ band 6 low gain image acquired in nighttime. ....	67
Figure 4.14 The histogram of above band6 sub-image, (a) is the results for high gain image, (b) is for low gain image. ....	67
Figure 4.15 The general statistical analysis from DNs of Landsat7 ETM+ TIR data (nighttime), (a) and (c) are the results from low and high gain, (b) and (d) are the related DN contours, respectively. ....	69
Figure 4.16 The histograms for study area from ASTER TIR data, band 10, 12, 13, 14. ....	70
Figure 4.17 The general statistical analysis from DNs of ASTER TIR data (band 10). ....	70
Figure 4.18 The results of classification of site 6 from ASTER TIR band10, band12, band13, and band14, from (a)- (d), respectively. ....	72
Figure 4.19 Histograms of site 6 from ASTER TIR band10, 12, 13, 14. ....	72
Figure 4.20 The results of classification of site 6 from Landsat7 ETM+ band 6 nighttime data, (a) low gain, (b) high gain. ....	73
Figure 4.21 Histograms for site6 of Landsat7 ETM+ band6 data, (a) is for low gain, (b) is for high gain. ....	73
Figure 4.22 The analysis results from ASTER TIR and Landsat7 ETM+ band6 data after the correct based on the histograms. ....	74
Figure 4.23 The final analysis results for site6 from ASTER TIR band13 (the red area) and Landsat7 ETM+ band6 low gain data (the yellow area) overlaying on an ASTER visual image, (a) ASTER TIR sub-image, (b) Landsat7 band6 nighttime sub-image, (c) result from ASTER band13, (d) result from Landsat7 low gain data. ....	75
Figure 4.24 The analysis results in different level of probability from Landsat7 ETM+ band6 nighttime low and high gain data. ....	77
Figure 4.25 The analysis results in different level of probability from ASTER band12 and band13 data. ....	78
Figure 4.26 The result of supervised classification from Landsat7 ETM+ band 5,4,3 (RGB), (a) is the visual image, (b) is the classification result. ....	80
Figure 4.27 The result of unsupervised classification from Landsat7 ETM+ band 5,4,3 (RGB). ....	81

## List of Tables

Table 1.1 Table of Data sets .....	9
Table 3.1 Radiometric sensitivity .....	25
Table 3.2 ASTER data product list.....	27
Table 3.3 ASTER data sets .....	28
Table 3.4 The results of GCPs .....	31
Table 4.1 Two sets of $L_{\min}$ and $L_{\max}$ of Landsat7 ETM+ 1G data. ....	48
Table 4.2 Landsat7 ETM+ Dynamic Range watts / ( $m^2 * sr * \mu m$ ) .....	48
Table 4.3 Temperature calculation from Landsat7 ETM+ band 6 low and high gain data (partly).....	52
Table 4.4 Maximum radiance of 370 K blackbody .....	54
Table 4.5 Unit conversion coefficients.....	55
Table 4.6 Temperature calculation from ASTER TIR data.....	57
Table 4.7 Final temperature calculation of the site 6 from Landsat7 ETM+ band6 and ASTER TIR data.....	76
Table 4.8 The results of probability calculation for site6 from Landsat7 ETM+ band6 nighttime data ASTER TIR data.....	79
Table 6.1 The characteristics of BIRD sensors.....	89

# Chapter 1 Introduction

## 1.1 Background of coal fires

Underground and surface coal fires are serious geological hazards in many coal mine regions in the world. Spontaneous combustion can occur either within the underground coal seams themselves or in piles of stored coal and in spoiled dumps on the surface.

Coal fires can cause grievous economic and environmental problems. Firstly, the coal fires consume a huge amount of coal resources causing economic loss. Secondly, the environmental effects of coal fires are serious problems at both local and global levels. During the burning of coal fires, there are some kinds of noxious gases diffused out, such as sulphur dioxide (SO<sub>2</sub>), nitrogen oxides (NO), carbon monoxide (CO), carbon dioxide (CO<sub>2</sub>), and methane (CH<sub>4</sub>) (Bhattacharya and Reddy, 1994). Unfortunately, these gases contribute to the green house effect. The smoke and windblown ash can plague the areas around coal fires. In general, degradations of the land and vegetation are caused by fires. Furthermore, in some areas, the coal fires may even cause desertification.

Widespread cracking and subsidence of the land surface are other associated problems. Surface collapse may cause extensive damage to infrastructure, such as buildings, roads, railways, etc. Problems caused by coal fires are:

- (1) Loss of coal resource;
- (2) Effect or damage to coal mining infrastructure or surrounding infrastructure;
- (3) Degradation of the land and vegetation and damage to the ecological system;
- (4) Serious environmental pollution;
- (5) Safety and health risk for miners, and local residents.

Coal fires can be classified into 4 groups according to its occurrence:

- (1) Underground mine fire: which is occurring in the areas of underground coal mining. They are restricted to the mines and can be detected by remote sensing techniques only if they are less than 30 meters in depth (Greene et al., 1969) in areas where there are no cracks or fractures to lead the underground heat to the land surface.

- (2) Coal seam fires or coal field fires: normally start due to the spontaneous combustion of a coal seam at the outcrop of the coal seams or at a coal seam at shallow depth. They can also develop from underground coal mine fires spreading to the surface.
- (3) Coal refuse fire: burning mainly due to spontaneous combustion.
- (4) Coal stack fire: more or less similar to the coal refuse fire (Zhang, 1998).

Coal fires also can be classified into 3 types of coal fire according to the depth of the fire:

- (1) Shallow fires, with the depth up to 10 meters;
- (2) Intermediate fires, with the depth from 10-30 meters;
- (3) Deep fires, over 30 meters in depth (Greene, et al., 1969).

This research mainly concentrates on the coal seam fires, which occur in the area of coal mining. Its depth from the land surface is less than 30 meters.

## **1.2 Coal fires in China**

China is the largest country in coal production and consumption. In 1996, its coal production was about 1400 million tons and 75% of the nation's consumption of primary energy was supplied from coal. Forecasts indicate that its share of total energy use will grow in the coming decades.

However, coal fires are a seriously problem in Northern China, where nearly 90% of the nation's coal resources are stored. In this region, many coal fields suffer from scattered, localized or clustered coal fires. The coal fires occur in a belt from the northwest to the northeast, stretching 5000 km in east-west direction and is 1500-1800 km in width (Figure 1.1). The size of the region is nearly 5.3 million km<sup>2</sup>, covering 13 provinces. Each year, the loss of coal resources caused by coal fires is from 10-13.6 million tons and the damage to coal resources affected by coal fires is about 200 million tons (Guan et al., 1997). Therefore, China is the most serious affected country in the world by the spontaneous combustion of coal fires.

The problem of coal fires has been listed in the "21<sup>st</sup> Century Agenda of China" as one of the five most serious geological hazards in 1994 (Guan et al., 1996). Recently, five serious areas of coal fires in Xinjiang Uygur Autonomous Region have been extinguished (URL-1, News, 2000, in Chinese).

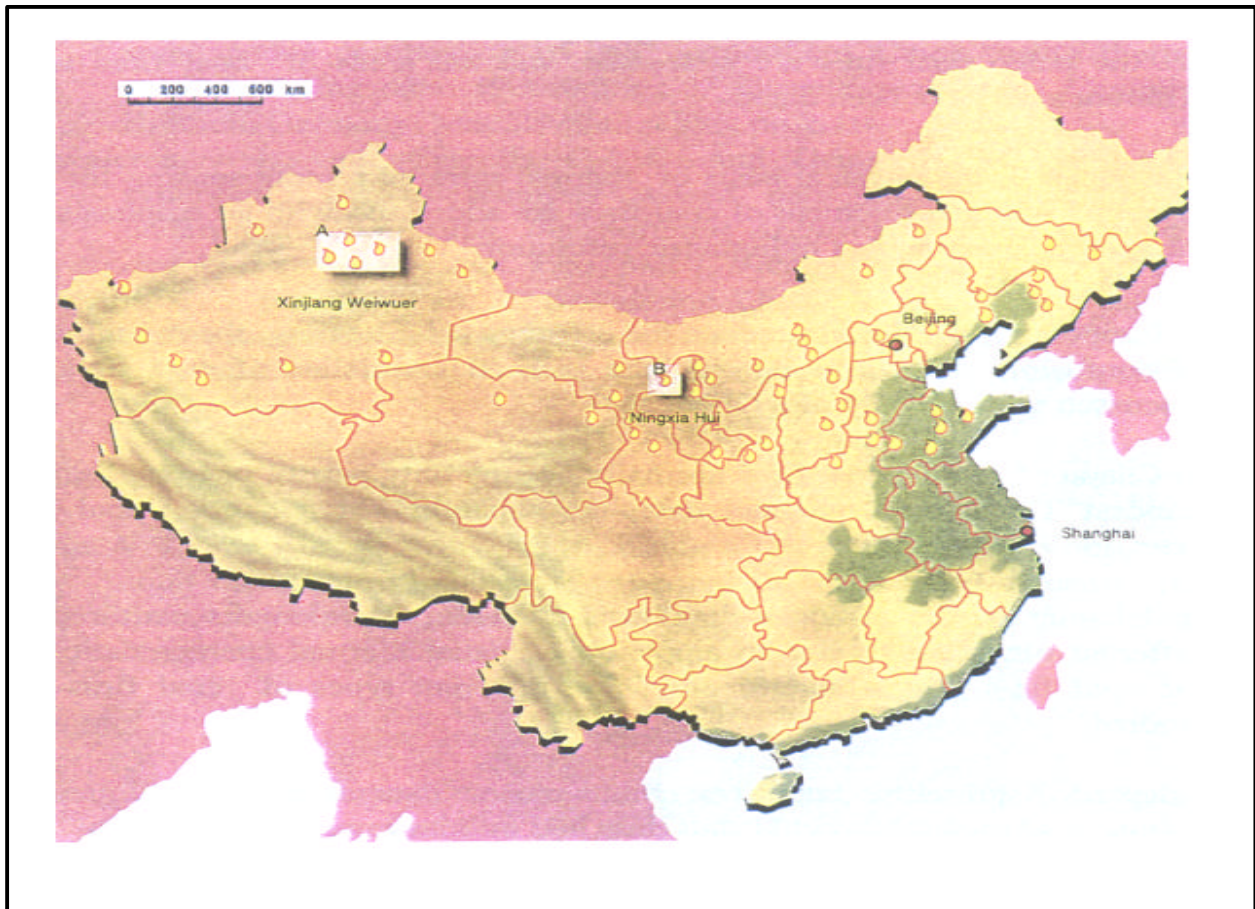


**Figure 1.1 Map of Coal fires in Northern China**

The location of coal fires in the north of China as detected by remote sensing and from other sources. Location A and B are Xinjiang and Ningxia Autonomous Region, respectively, where the coal fires are most serious.

### **1.3 Spontaneous combustion of coal**

Coal is a combustible material, making it susceptible to a variety of ignition scenarios. One of the most frequent and serious causes of coal fires is spontaneous combustion. Fires are controlled by three factors: temperature, fuel and oxygen. The spontaneous combustion of coal is governed by the oxidation of coal. It can be simply expressed as follows (Rosema et al., 1999):



Spontaneous combustion fires usually begin as “hot spots” deep within the reserve of coal. The hot spots appear when coal absorbs oxygen from the air. The coal’s temperature begins to climb above ambient temperature. When the temperature of coal reaches a threshold tempera-

ture, somewhere between 70 and 140 °C a steady reaction, resulting in the production of gaseous products such as carbon monoxide and hydrogen, ensue. The temperature of the coal will certainly continue to rise until 230-280 °C, the reaction becomes rapid and strongly exothermic. In other words, the coal begins ignition or starts to burn. As the heating rate increases in intensity, incipient combustion, and ultimately self-ignition and flame, will occur. Figure 1.2 indicates the influence of these factors on the intensity of the fire.

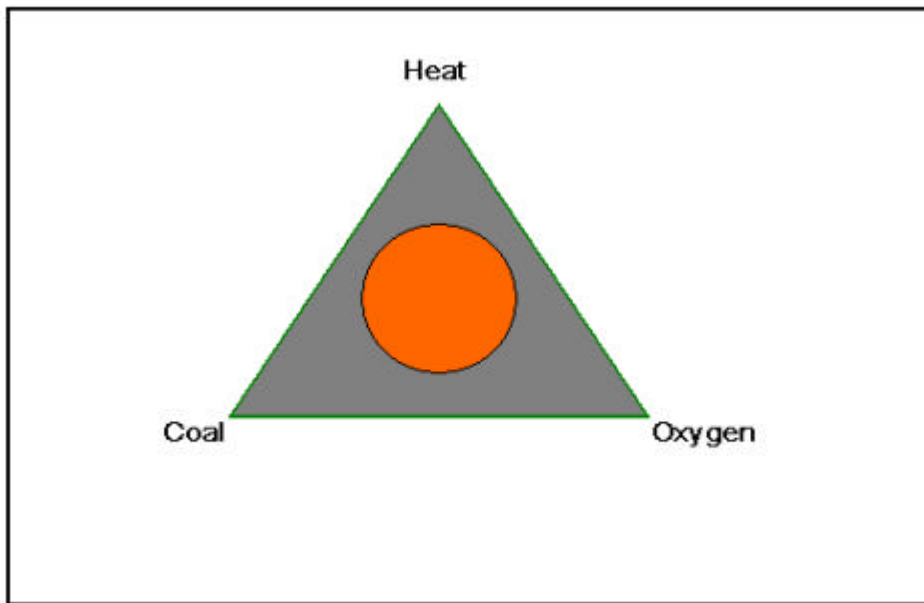


**Figure 1.2 Spontaneous combustion of coal**

Spontaneous combustion of coal relates to the quality of coal and the size of the particles, high-ranking coals (high carbon content) are more prone to burning than the lower-ranking coals; and the larger the effective surface area of the coal particles, the more easily the reaction can proceed (van Genderen and Guan, 1997).

Environmental factors play a main role in the oxidation reaction of coal (Rosema et al., 1999). Oxidation requires adequate supply of air, such as the cracks and fissures caused by coal mining will stimulate the underground coal fires by transmitting the air/oxygen to the coal seams. Besides, the local climate condition is another important factor in the oxidation reaction of coal. Once the threshold temperature is reached, the second stage of the oxidation reaction will begin, the heat generated by the reaction rises at a rapid rate and the temperature of the coal will continue to rise until combustion starts.

## 1.4 Detection of coal fires

There are three main kinds of methods in detection of coal fires, which are borehole temperature measurements, airborne remote sensing, and space-borne remote sensing techniques. The method of borehole temperature measurements has the obvious advantage that the temperatures were close to the fires and measured directly, but it was often difficult to get enough data for a large area, and it is too expensive to carry out. The airborne remote sensing techniques used in detecting coal fires started in 1960's in the USA. The surface thermal anomalies caused by coal fires were detected using the airborne remote sensed thermal infrared imagery. From 1980's, the space-borne remote sensing techniques started to be used in the detection of coal fires. This method has some advantages in comparison to other methods, such as it is possible to detect the coal fires using multi-spectral and/or multi-temporal data, it is practicable to detect/monitor a huge area, and it is relatively much more economic. This study is concentrating on the third method.

A project, called "Environmental monitoring and evaluation of coal fires in Northern China", is presently executed by German, Dutch and Chinese researchers. It is sponsored by German and Chinese governments.

This research is a contribution to this project, it is tried to obtain a better understanding in detecting the area of coal fires using remote sensing techniques.

Aspects that will be studied are:

- (1) How to detect areas of coal mining and coal fires by means of remote sensing techniques?
- (2) Which are the best sensors/ spectral regions for monitoring coal fires?
- (3) What is the best time of acquisition of satellite images for detection of coal fires?
- (4) What is the accuracy and reliability of the results?

## 1.5 Objectives of this study

The main objective for this study is to find a practical method of detecting / monitoring the area of coal fires using multi-spectral and multi-temporal satellite data. In addition to this, other objectives defined are:

- (1) To detect the area of coal mining using satellite data;
- (2) To detect the area of coal fires using satellite data;

- (3) To compare the results of detection using the data acquired from different sensors and at different acquisition times (day/night);
- (4) To analyse the quality and certainty of the results of detection from satellite data.

## **1.6 Introduction to the study area**

The study area was selected based on the availability of data and the goals of the above-mentioned project. Kerjian Coal Mine, in Xinjiang Uygur Autonomous Region, north of China, was selected as the study area. The center point of the study area is N 43°07' and E 88°12', and the size of the area is 30\*30 km. This area is situated on the south piedmont of the Tianshan Mountains and at the northwest border of Turfan Basin region, 110 km from Urumchi located towards the southeast, the capital of Xinjiang. The morphology can be described as hills with wide alluvial fans. The highest hill in this region is 1900 meters. In average this area is 1100 meters. Morphologically, the area around the burning zone rises from southeast to northwest. The PanjiTage River is the only major river crossing the area. Its runoff is 0.13-0.16 m<sup>3</sup>/s. Around 5 km southeast of the burning area a smaller river exists, the Beiyang River (DMT, 2001).

Tuokexun is the biggest town next to the burning area, it is situated 55 km towards the southeast. It is a city with about 100,000 inhabitants, and it has basic infrastructure. There is only a simple highway going to the burning area that is partly in bad conditions. To the east it goes on to the Xiaocao Lake( 22 km away). From there a motorway goes to Urumchi (152 km). 2 km southeast of the burning area the railway Turfan-Aksu crosses the area in east-west direction. It is 80 km away from the line junction in Turfan. There a further railway connection to Xinjiang-Lanzhou (Gansu province) exists.

From north to south the topography in the study area changes from rugged piedmont to alluvial fans into the Turfan Basin. The vegetation there is either sparse or absent due to the minimal annual precipitation, which is less than the potential evaporation. It belongs to a typical continental climate, hot and rainy in summer, cold and dry in winter, and the temperature difference between summer and winter, or between day and night is very large. Normally, the hottest weather concentrates in July, freezing starts from October, and thawing starts in March the following year. The freeze-up period is about 150 days. The average wind speed is about 2.0 m/s, and the wind blows from the northwest to the southeast most time of the year.

The main coal-bearing geological strata of coal mine belong to the Middle Jurassic Xishanyao Group, which consist of freshwater deltaic sediments including mudstone, silstone, sandstone and coal layers (Guan et al., 1997). There are 5-10 layers considered minerable, and

the total thickness of coal layers is about 15 meters. Thick coal seams (>5m ) have a higher spontaneous combustion risk (Guan and van Genderen, 1997). The geological structure of coal seams indicates mainly as folds and buckles. There is a 33 km long bowed fold in the east-west direction in the Kerjian area. The Kerjian coal mine is situated south of this fold (Report from DMT, 2001). Figure 1.3 shows a sketch map and cross section of Kerjian coal mine region (Report from DMT, 2001).

A general geology investigation showed that there are 56 areas affected by coal fires in the north of China, of these 38 areas are located in Xinjiang. The estimated total size of the coal fire areas is about 720 km<sup>2</sup>, the size of burning area is 17-20 km<sup>2</sup>, among which, 10-13 km<sup>2</sup> is situated in Xinjiang (Guan et al., 1997). The coal fires in Kerjian coal mine started to burn in the 1970's. Two primary coal fields and some secondary ones are distributed in this area. There are three more serious areas of coal fires located in Kerjian, 2 to 3 km in depth and the width from 50 to 200 m (relatively narrow).

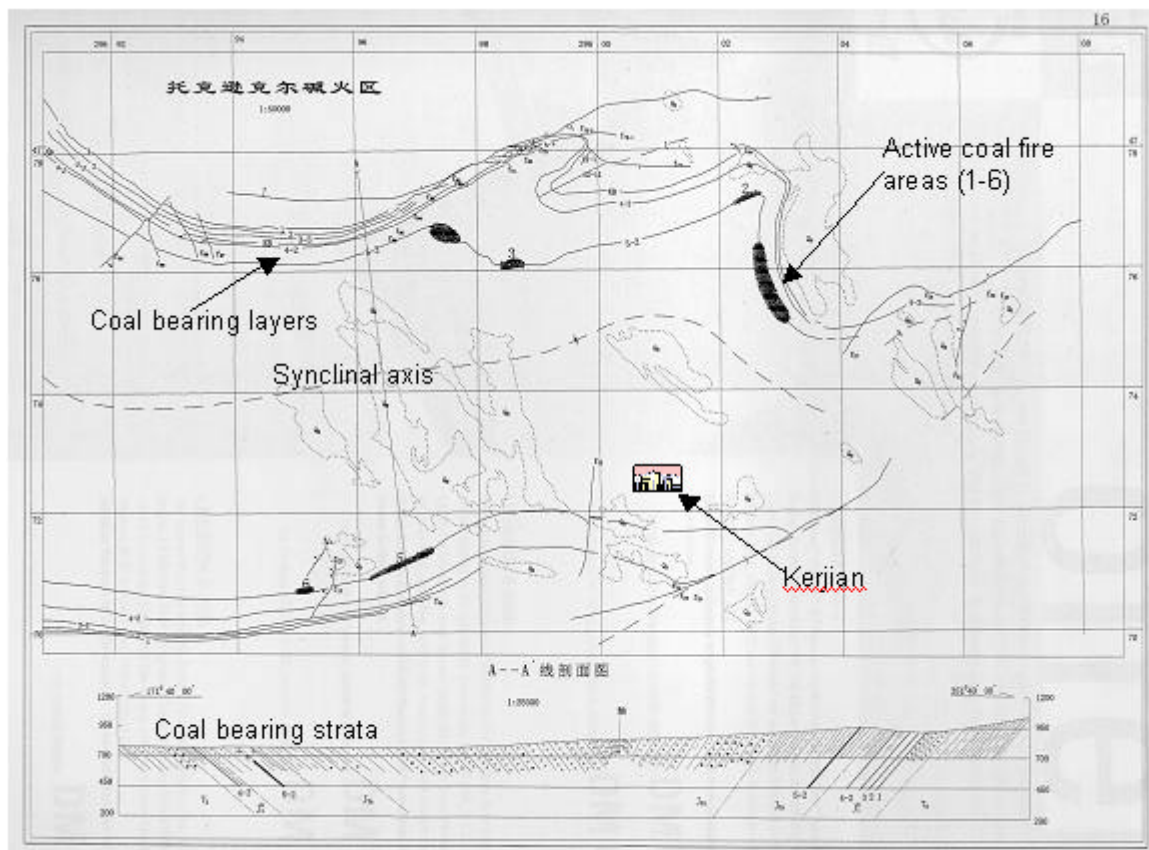


**Figure 1.3 Sketch map of the Kerjian coal fire area, the black clusters are surveyed coal fires.**

## 1.7 Data used for the research

The data collected for this research consists of:

- (1) Landsat7 ETM+ imagery, from band 1 to band 7, and a panchromatic image acquired on 23<sup>rd</sup> of August, 1999;
- (2) Landsat7 ETM+ band 6 nighttime data acquired on 1<sup>st</sup> of February, 2000;
- (3) ASTER data, from band 1 to band 14, including the backward looking band 3b, which can be used to generate a stereoscopic image with the nadir-looking band 3n (the detail of the data acquisition time will be introduced in Chapter 3);
- (4) ERS SAR interferometric data;
- (5) Scanned topographical map, scale of 1:100,000;
- (6) GPS data measured within this study area and related report (DMT, 2001);
- (7) Other information, including literature and thematic maps.

Some data, as Landsat 7 ETM+ images, ERS SAR data, GPS data and related report, are obtained from German researchers who also join the project mentioned above. Other data is collected by author himself. Besides, some field data is surveyed by Chinese researchers within the project. Further details of spectral characteristics of the satellite data and time of acquisition are listed in Table 1.1.

Of the above mentioned satellite data, Landsat 7 ETM+ images and ERS SAR interferometric data could be obtained from the German researchers. ASTER data is downloaded from the Internet (<http://asterweb.jpl.nasa.gov/>). ASTER (Advanced Spaceborne Thermal Emission and Reflection Radiometers) is an advanced multi-spectral sensor on board of the Terra polar orbiting spacecraft. The ASTER instrument was built in Japan for the Ministry of International Trade and Industry (MITI). A Joint US/Japan Science Team is responsible for instrument design, calibration, and validation.

ASTER data covers a wide spectral region from visible to thermal infrared with 14 spectral bands with high spatial, spectral and radiometric resolution. The wide spectral region are covered by three telescopes, three VNIR (Visible and Near Infrared Radiometers) bands with a spatial resolution of 15 m, six SWIR (Short Wave Infrared Radiometers) bands with a spatial resolution of 30 m and five TIR (Thermal Infrared Radiometers) bands with a spatial resolution of 90 m. In addition one more telescope is used to see backward in the near infrared spectral band (band 3B) for stereoscopic capability that will produce a base-to-height ratio of 0.6. ASTER will be used to obtain detailed maps of land surface temperature, emissivity, reflectance and elevation, whose goal is to obtain a better understanding of the interactions between the biosphere, hydrosphere, lithosphere and atmosphere. The ASTER instrument has two types of Level-1 data, Level-1A and Level-1B data, which are free to use. Level-1A data are

formally defined as reconstructed, unprocessed instrument data at full resolution. Level-1B data are generated by applying coefficients for radiometric calibration and geometric resampling. Each group of data are divided into scenes of 60 km in the along-track direction but includes 3 more km of data to provide an overlap of 5 % with neighboring scenes except for backward stereo band 3B. For band 3B the scene size is 81 km, including an additional overlap of 6 km to compensate for the terrain error contribution and a scene rotation for a large cross-track pointing. ASTER provides the user community with Standard Data Products throughout the 6-years life of the mission.

**Table 1.1 Table of Data sets**

<b>Sensor</b>	<b>Spectral bands</b>	<b>Spatial resolution</b>	<b>Spectral region</b>	<b>Time of acquisition</b>
<b>Landsat7 ETM+</b>	Band 1: 0.45-0.52 $\mu$ m	30 M	VNIR	1999-08-23 daytime
	Band 2: 0.53-0.60 $\mu$ m			
	Band 3: 0.63-0.69 $\mu$ m			
	Band 4: 0.75-0.90 $\mu$ m			
	Band 5: 1.55-1.75 $\mu$ m			
	Band 6: 10.4-12.5 $\mu$ m	60 M	TIR	2000-02-01 nighttime
	Band 7: 2.09-2.35 $\mu$ m	30 M	SWIR	1999-08-23 daytime
	Band 8: 0.52-0.90 $\mu$ m	15 M	Panchromatic	
<b>ASTER Sensor (Level 1A/1B)</b>	Band 1:0.52-0.60 $\mu$ m	15 M	VNIR	More details in Chapter 3
	Band 2:0.63-0.69 $\mu$ m			
	Band 3n:0.76-0.86 $\mu$ m			
	Band 3b: 0.76-0.86 $\mu$ m	15 M	VNIR	
	Band 4:1.600-1.700 $\mu$ m	30 M	SWIR	
	Band 5:2.145-2.185 $\mu$ m			
	Band 6:2.185-2.225 $\mu$ m			
	Band 7:2.235-2.285 $\mu$ m			
	Band 8:2.295-2.365 $\mu$ m			
	Band 9:2.360-2.430 $\mu$ m			
	Band10:8.12-8.47 $\mu$ m			
	Band11:8.47-8.82 $\mu$ m			
	Band12:8.92-9.27 $\mu$ m			
	Band13:10.25-10.95 $\mu$ m			
Band14:10.95-11.65 $\mu$ m				
<b>ERS SAR</b>	<b>DEM</b>	25 M		
<b>Scanned topo map</b>		1:100,000(scale)		

ASTER data is downloaded from Internet using Windows Sockets FTP software after the notification was received by email. The downloaded data, in Hierarchical Data Format (HDF), have to be transformed into image files using ENVI 3.4 system.

## **1.8 Methodology**

Through understanding the properties of spontaneous combustion of coal fires, to analyze the relationship between thermal anomalies caused by coal fires and the characteristics of electromagnetic spectrum, further, try to grasp the serious changes caused by coal fires at the land surface. Then, to extract the features related coal mine and coal fires from images according to the spectral characteristics of the thermal anomalies, by means of image processing technology. After feature extraction, the coal mine locations and coal fires are roughly determined. However, these results are deducted from images separately. Hence, the multi-sensor and multi-temporal data analysis techniques will be used to improve the accuracy of those results. Last, the detection results of areas of coal fires have to be validated by the field data and an accuracy assessment has to be performed.

The research work is divided into three steps. The first step is related to data acquisition and image pre-processing. Secondly, to detect areas of coal fires by means of feature extraction, with the help of image processing techniques. Multi-sensor and multi-temporal data image analysis will be carried out. The last step is to confirm the above detection results using field data and other related information. The flow chart of research work is as the Figure 1.4.

## **1.9 Structure of the thesis**

The details of this thesis are presented in the following chapters:

Chapter1 gives a background on coal fires, the approaches and objectives of this research.

Chapter2 describes remote sensing techniques used for the detection of coal fires, a review is given for detecting those features caused by coal fires using different sensors, with emphasis on the detection of thermal anomalies and their correlated influencing factors.

Chapter3 will give a presentation on the data acquisition and image processing, including the geometric correction, image registration, band combination, brightness contrast, and image filtering etc.

Chapter4 introduces the work on the image interpretation, feature extraction, and image analysis for detecting the areas of coal fields and coal fires.

Chapter5 will focus on the method of accuracy assessment for the detection results using field surveying data.

Chapter6 will give conclusions and recommendations.

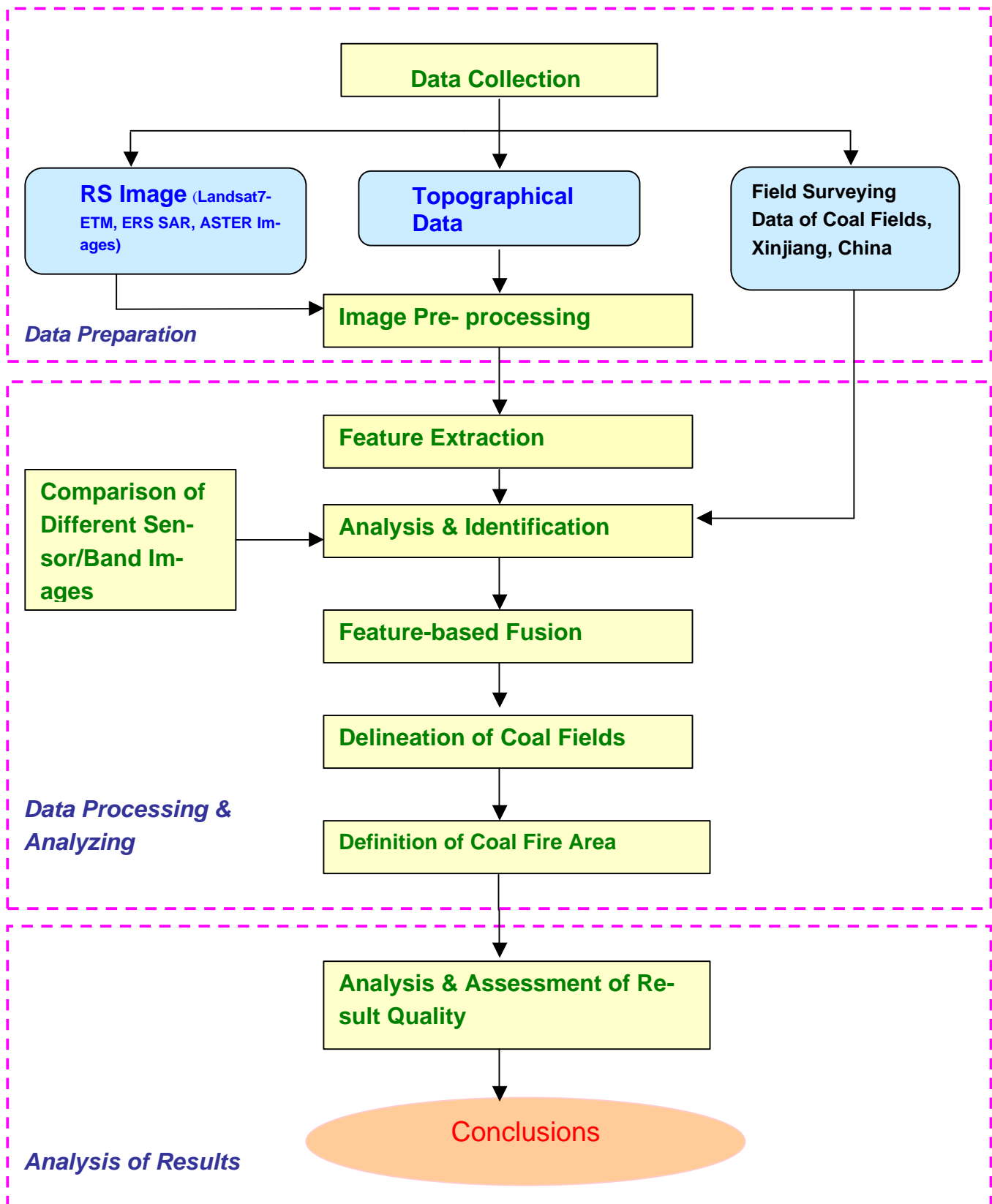


Figure 1.4 Framework of Research Work

# Chapter 2 Remote sensing methods used for the detection of coal fires

## 2.1 Introduction

Remote sensing was first used for the detection of coal fires in America in the 1960s. Surface thermal anomalies detected by Greene (1969) and his colleagues were sufficiently great to be detectable on thermal infrared imagery. In 1972, coal fires in the Burning Mountain, in Australia, were detected using an airborne optical mechanical sensor operating in the infrared wavelength (Ellyett and Fleming). Since the 1980s, remote sensing application for coal fires started in China and India, using airborne and spaceborne sensors. During the last decade, researchers started to study the use of short wavelengths, such as band 7 and band 5 of Landsat 7 ETM+, for the detection of high temperature hot sources and surface coal fires (Reddy, et al., 1993; Prakash, et al., 1997).

The electromagnetic energy measured by airborne or spaceborne platforms can assist in detecting, identifying, and classifying earth features. These sensors acquire data of various earth surface features that emit and reflect electromagnetic energy. These data are analyzed to provide information about the earth surface features under investigation.

Underground coal fires can cause series of changes to the land surface, these include: the increase of temperature, emission of smoking, changes in colour of caprocks, formation and deposition of new materials on the surface, land cracking and subsidence at the surface (Genderen and Guan et al., 1997). The features/ characteristics of these changes can be detected by satellite remote sensing data, for example, in optical imagery, the burnt caprock above the coal fires often display a unique spectral signature as the baked rocks have a different reflectance compared to the natural overburden; the smoke and high density sulfur dioxide plume also can be seen in the satellite image; and the thermal anomalies can be detected using satellite thermal infrared images.

The thermal anomaly of a fire that will occur in the area of coal fires is the most important characteristic in the detection process of coal fires. It can be used as an indicator for the fire area extent, intensity and the amount of coal loss. The thermal anomalies caused by the heat of combustion of the coal are a clear indicator of the existence and outline of coal fires, which can be detected by thermal infrared sensors both on airborne and spaceborne platforms. For a rough understanding of coal fires, the heat impact of the coal fires can be simply indicated using the following equation:

Coal + O<sub>2</sub> → CO<sub>2</sub> + CO + SO<sub>2</sub> + Other Gases + H<sub>2</sub>O + Ash + ?H

Here, ?H is the heat caused by the combustion of coal fires. The heat dissipates into the environment in several ways, such as conduction, convective heat exchange and radiation. It is notable that the tailings of coal mines are prone to catch fire. They can contain a considerable amount of coal throughout the whole body and have a good oxygen supply from all exposed sides (Rosema and Guan, et al., 1999). Because of the high permeability during the heat conduction, which is the main way of heat transportation in the intact rock of the coal seams, the fire can occupy large volumes, so that the thermal anomalies can occur over a large area. For this reason, in the detection of thermal anomalies of coal fires using remote sensed data, the tailings directly next to the area of subsurface fires may be misinterpreted.

Several satellite sensors can partially detect coal fires depending on certain conditions, such as the size of coal fire area, the spatial resolution of the imagery, the depth of fires, the amount of difference between the temperature anomaly in the area of coal fires, and the temperature in the surrounding background, the time of the data acquisition (day or night, season) and prevailing weather conditions, etc. Hence, one of this research objectives is to fuse the pixel based data, features or information extracted (decision based) from each individual sensor source in order to get more complete, robust and reliable results in detecting the areas affected by coal fires.

## **2.2 Optical satellite data**

Experience has shown that many earth surface features of interest can be identified, mapped, and studied on the basis of their spectral characteristics. Thus, to utilize the remote sensing data effectively, one must know and understand the spectral characteristics of the particular features under investigation in any given application. Likewise, one must know what factors influence these characteristics. Because spectral responses measured by remote sensors over various features often permit an assessment of the type and/or condition of the features, these responses have been referred to as spectral signatures. It is more important to understand the nature of the ground area one is looking at with remote sensing data, not only to minimize unwanted spectral variability, but also to maximize this variability when the particular application requires it (Lillesand, Kiefer, 2000), such as the detection of the areas of coal fields and coal fires.

Besides, temporal and spatial effects have to be entered into any analysis of remote sensing data. Temporal effects are factors that change the spectral characteristics of a feature over

time. For example, the thermal anomalies caused by coal fires change evidently in different time of the day and/or year, the spectral characteristics of the surface in coal fire area will also go along with it. Thermal anomalies are more notable if the remotely sensed data is acquired in the nighttime or in winter season because the solar radiation is greatly reduced so that the difference between the temperature of coal fire area and the temperature of surrounding area is much amplified. Generally speaking, the optimum data acquisition time is better in pre-dawn or in winter season because the solar heating effects can be reduced relatively. These changes often influence our collection of sensor data for a particular application.

The changes on the ground surface caused by coal fires can be directly or indirectly detected by the satellite optical data. For example, the color changes of the caprocks, the changes in terrain and relief, the subsidence, the crack, etc., can be directly detected in the optical images. These features can help us to recognize the potential areas of coal fires, even though, these features can be referred to as indirect indicators of coal fires because it is uncertain that such features indicate either present burning underground coal fires or only paleo-coal fires. Thermal anomalies can be detected in short wave infrared spectrum if they have a temperature higher than 160°C (Matoon, Dozies; Ralthey et al., 1995). Besides, the smoke and sulfur dioxide can also be directly detected in satellite optical images.

Earth observation satellite imagery derived from Landsat 7 ETM+ and ASTER sensor are used in this study. Landsat7 ETM+, the Enhanced Thematic Mapper Plus (ETM+), was launched in April of 1999, its role is to make global, high-resolution measurements of land surface and surrounding coastal regions. Landsat7 ETM+ data are collected from a nominal altitude of 705 kilometers in a near-polar, near-circular, sun-synchronous orbit at an inclination of 98.2 degrees, imaging the same 183-km swath of the Earth's surface every 16 days. Landsat7 ETM+ will monitor important natural processes and human land use such as vegetation growth, deforestation, agriculture, coastal and river erosion, snow accumulation and fresh-water reservoir replenishment, and urbanization. The repeated, extensive coverage of Landsat7 ETM+ is excellent for observing seasonal changes on continental and global scales, and its fine resolution is ideal for perceiving important detail in land surfaces. It detects spectrally-filtered radiation at visible, near-infrared, short-wave, and thermal infrared frequency bands from the sun-lit Earth, nominal ground resolutions are 15 meters in the panchromatic band, 30 meters in the 6 visible, near and short-wave infrared bands, and 60 meters in the thermal infrared band (high and low gain).

As indicated above, ASTER has three spectral bands in the visible near-infrared (VNIR), six bands in the short-wavelength infrared (SWIR), and five bands in the thermal infrared (TIR) regions, with 15, 30, and 90 meters ground resolution, respectively. The VNIR subsystem has one backward viewing band for stereoscopic observation in the along track direction.

Because the data has wide spectral coverage and relatively high spatial resolution, we will be able to discriminate a variety of surface materials and reduce problems of some lower spatial resolution data resulting from mixed pixels. The primary science objective of the ASTER mission is to improve understanding of the local and regional scale processes occurring on or near the earth's surface and lower atmosphere, including surface atmosphere interactions. ASTER data has been applied in a large number of research fields, such as land surface climatology, vegetation and ecosystem dynamics, volcano monitoring, natural hazard monitoring, aerosols and clouds study, carbon cycling in the marine ecosystem, hydrology, geology and soil, land surface and land cover change, etc.

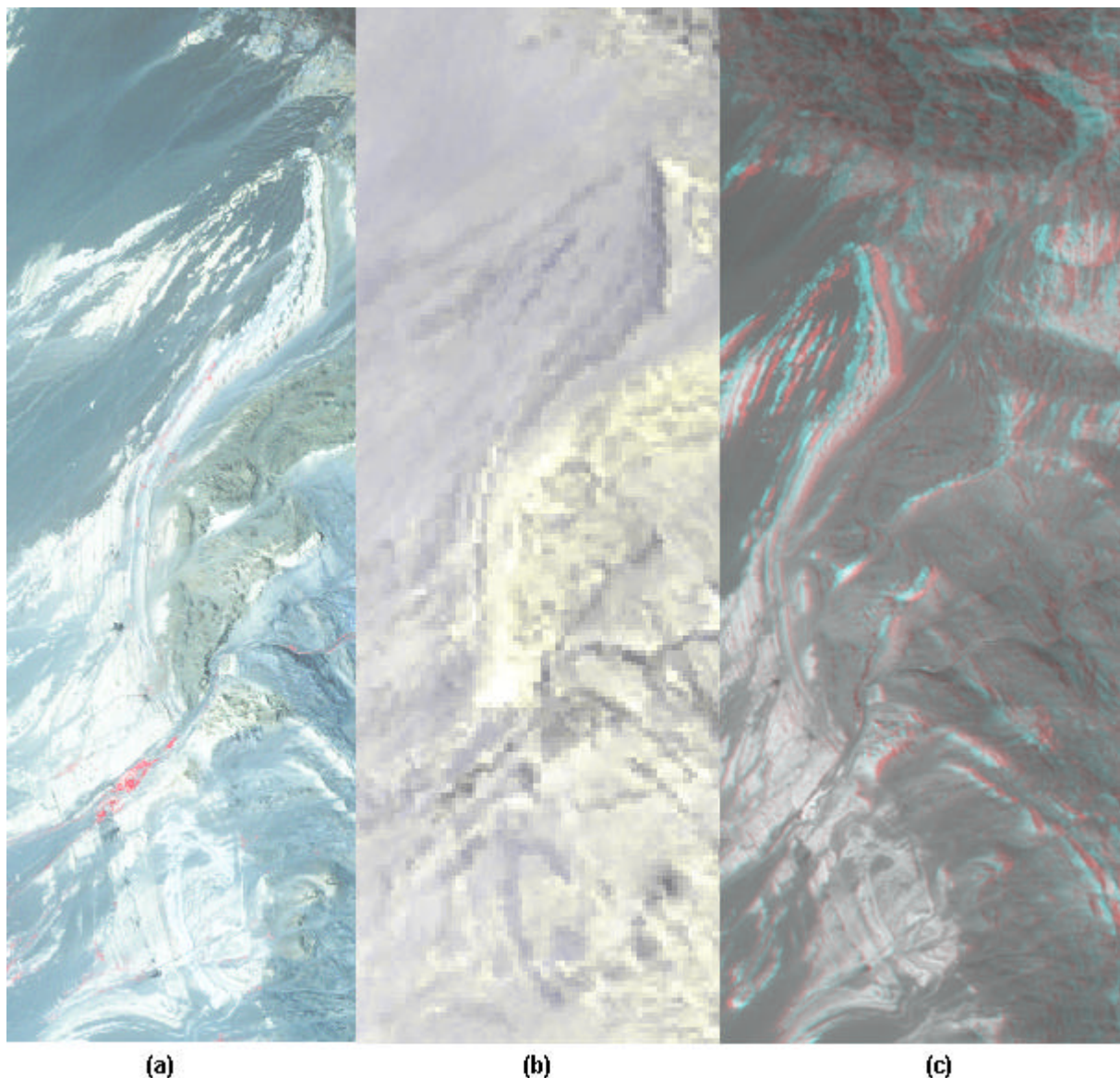


**Figure 2.1 A combination of ASTER VNIR (a), SWIR (b), and anaglyph images (c) used in the interpretation of this study**

The three VNIR bands of ASTER will be especially useful for topographic interpretation because it has along-track stereo coverage in band 3, with nadir (bands 1,2,3N) and backward (band 3B) views with 15 meters spatial resolution. The VNIR bands will also be useful in assessing vegetation and iron-oxide minerals in surface soils and rocks. The spectral range of SWIR bands were selected mainly for the purpose of surface and mineral mapping.

The synoptic overview can also provide great aids in studying the areas of coal fields in their regional geological structure and tectonic settings, especially when using the high resolution data, band 1 to band 3 of ASTER data. The backward- and nadir-looking telescope pair is used for same-orbit stereo imaging (along-track stereo). The two near-infrared spectral bands, 3N and 3B, generate along-track stereo image pair with a base-to-height (B/H) ratio of about 0.6, and an intersection angle of about 27.7 degrees. Producing Digital Elevation Models (DEMs) from satellite data has been a vibrant research and development topic for the last thirty years. Since an error of within plus-or-minus one pixel for the parallax measurements in the automated matching process has been achieved with different stereoscopic data sets (along-track and across-track), the potential accuracy for the along-track stereo derived DEM from ASTER could be in the order of 25 meters (T. Toutin and P. Cheng, 2000). The above authors developed the automatic DEM generation software at PCI, it is possible to generate stereo-DEMs with accuracy less than 25 meters using a stereo pair of ASTER data. If the images and study site are optimal - such as semi-arid area, accuracy can be achieved as high as 10 meters and 17 meters with 83% and 90% levels of confidence, respectively.

The generated stereo view is useful for geomorphologic and terrain classification surveys. It can be combined with data of SWIR and TIR to provide synergic interpretation in studying the areas of coal fires. Anaglyph can be generated in hard copy format or through a screen view on the computer to help in the image interpretation. Figure 2.1 shows the combination of VNIR (a), SWIR (b), and anaglyph images (c) used during the interpretation. With the help of stereo view, using red green glass, the geologic characteristic features, such as fold, fault, stratum etc., and topographic features are easier identified and interpreted.

## **2.3 Thermal satellite data**

There are currently six satellite systems with thermal infrared sensors on board. The first one is NOAA with an Advanced Very High Resolution Radiometer (AVHRR), which has several spectral bands in the thermal infrared region, e.g. channel 3 (3.55-3.93 $\mu$ m), channel 4 (10.3-11.3 $\mu$ m), and channel 5 (11.5-12.5 $\mu$ m) on NOAA-7,9,11,12&14. The spatial resolution varies from 1.1km at nadir up to 8 km at the border of the image. The second satellite data source used for thermal anomaly detection is from the ATSR (Along Track Scanning Radi-

ometer) sensor on board the ESA ERS-1 satellite, which has a spatial resolution of approximately one kilometer. The third one is Russian RESURS-1 with the spatial resolution about 600m. The fourth one is EOS with the Advanced Space-borne Thermal Emission and Reflectance Radiometer (ASTER), launched in 1999, which spans the 8-12 $\mu$ m region with five contiguous bands and enables the possibility of multi-channel split window thermometry at 90m resolution (Kahle *et al.*, 1996). The fifth is Landsat 5 with the Thematic Mapper (TM) band 6 with the spatial resolution of 120 meters and at 10.4 to 12.5 $\mu$ m region of the electromagnetic spectrum. And the sixth is Landsat 7 with the Enhanced Thematic Mapper (ETM) band 6 with the spatial resolution of 60 meters, which was launched in 1999. The advantage of the space-borne remote sensing for coal fire detection is that it is repeatable, cheaper, and with multi-bands. The disadvantage is that the spatial resolution generally speaking is still very coarse.

### 2.3.1 Thermal infrared data used in the study of coal fire affected areas

Thermal anomalies caused by underground and/or surface coal fires are a direct indicator in detecting the area of coal fires, and they can be detected by the thermal infrared spectral data. The detection of underground coal fires using thermal infrared remote sensing is based on the premise that these underground heat sources produce detectable thermal anomalies at the ground surface. If there is a thermal anomaly present at the surface, there are also certain conditions under which it will be detectable on remote sensing data. The ability of detection depends on the resolution of the thermal infrared (TIR) imagery, the size of the area of the thermal anomalies and the difference between the temperature anomalies in the area of coal fires and the temperature of the surrounding background (Zhang, van Genderen, 1996).

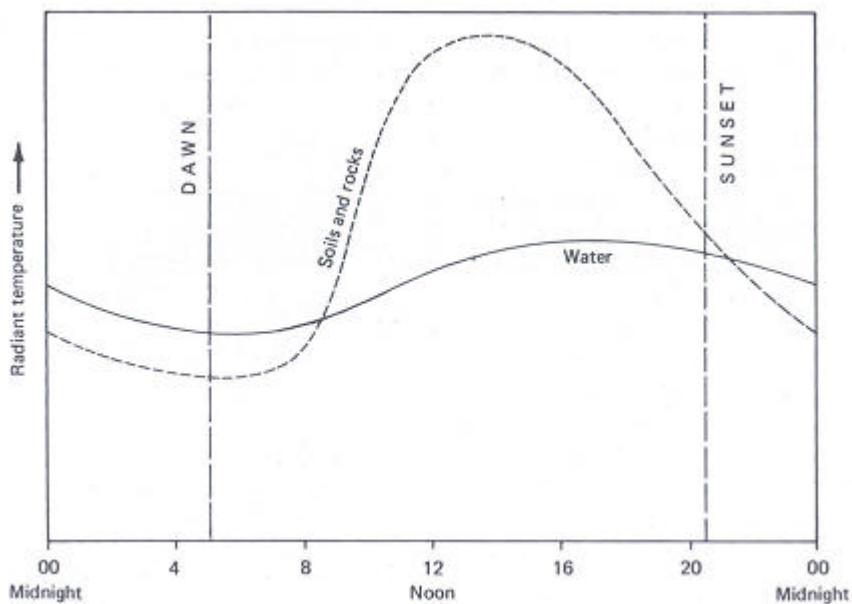


Figure 2.2 Generalized diurnal radiant temperature variations for soils and rocks versus water.

It is notable that land surface temperatures are determined by many factors. The important factors are time of day, time of year, weather conditions, slope aspect and the type of surface present. Surface temperatures usually follow a daily sinusoidal variation and there is a slower annual variation in temperature (Jury et al., 1991). Figure 2.2 illustrates the relative radiant temperatures of soils and rocks versus water during a typical 24-hour period (Lillesand and Kiefer, 2000). It indicates that the radiant temperatures of soils and rocks are small during pre-dawn and at nighttime. It can be seen that the surface temperature from nighttime to pre-dawn is relatively low, therefore, this period is the optimal time of data acquisition.

In the past, the main satellite data set used was Landsat TM band 6 data, which lies in the 10.4-12.5  $\mu\text{m}$  region of the electromagnetic spectrum. Numerous authors have used this data source to detect underground coal fires (Bhattacharya et al, 1991; Mansor et al, 1994; Praksh et al, 1995; van Genderen et al, 1996; Wan and Zhang, 1996). For the China coal fire research, the authors have also used multi-temporal nighttime thermal infrared data from Landsat TM in addition to the daytime data, thus the solar heating effects were greatly reduced or removed from the daytime imagery. However, the ASTER thermal infrared data has not been used for the detection of coal fire areas.

In this research, ASTER data is used as the main data source for the detection of the coal fire areas. In the thermal infrared spectral region, ASTER data has five bands with a spatial resolution of 90 meters, which lies from 8-12  $\mu\text{m}$ . Its spectrum almost covers the whole range of thermal infrared spectra, hence, it can provide much more multispectral information related to temperature. Further, to utilize the five bands of ASTER thermal infrared data, the thermal anomalies can be displayed more clearly with the help of a color composites and other image processing techniques in order to improve interpretation and feature extraction. Besides, Landsat7 ETM+ band 6 data, with a resolution of 60 meters, is also used in this study for the fusion and compared with the results obtained from ASTER data.

Generally, the spectral response patterns of the thermal anomalies derived from thermal infrared imagery will be influenced by temporal, spatial and atmospheric effects. The energy recorded by a sensor is always modified to some extent by these effects. Typically, the best time of data acquisition is pre-dawn because at that time the solar heating effects are relatively smallest and the thermal contrasts are strongest. Thus, not only the solar radiation is greatly reduced but also the spectral characteristic of thermal anomaly caused by coal fire is more distinct. It can improve the ability of detection in the study of coal fires.

In this research only daytime ASTER data was available. Instead of the absence of nighttime ASTER data, the data acquired at local winter season is used in this study. First, feature extraction is carried out from each set of data separately. Then, the results obtained separately

will be compared and fused together (feature-based fusion) in order to improve and increase the reliability and accuracy of the detection results of coal fires.

### **2.3.2 Temperature and emissivity**

The area of coal fires can be detected using remote sensing data because the temperature anomalies caused by coal fires can be detected by the thermal infrared (TIR) scanning, so the land surface temperature is an important direct indicator in the detection of coal fires. However, we can not get the value of temperature directly from thermal infrared imagery, we can only get the digital values (DN) of the measured thermal radiations. TIR radiations vary with both temperature (T) and emissivity (e).

In many applications of thermal scanning techniques, the digital data of surface temperature distributions recorded by a thermal scanner can be processed, analyzed, and displayed in a variety of ways. The calibration relationship can be applied to each point in the digital data set, producing a matrix of absolute temperature values. The precise form of a calibration relationship will vary with the temperature range in question, we assume that a linear fit of the digital data to radiant existence is appropriate. Under this assumption, a digital number, DN, recorded by a scanner, can be expressed by (Lillesand and Kiefer, 2000)

$$DN = A + BeT^4 \quad (2.1)$$

where, A,B = system response parameters determined by sensor calibration

e = emissivity at the point of measurement

T = kinetic temperature at the point of measurement

Once A and B determined, kinetic temperature T for any observed digital number DN is given by

$$T = \left( \frac{DN - A}{Be} \right)^{1/4} \quad (2.2)$$

At a minimum, two corresponding temperature (T) and digital number (DN) values are needed to solve for the two unknowns A and B, here, we assume that the emissivity is known. Once parameters A and B are known, this equation can be used to calculate the kinetic temperature for any ground point for which DN is observed recorded in the imagery.

The emissivity is the ratio of the radiation emitted by a surface to the radiation emitted by a blackbody at the same temperature. In equation (2.2), we assume that the emissivity is known, however, except for water, vegetation, and snow or ice, the emissivity of the land sur-

face is unknown, but must be determined along with the temperature. Especially in coal mine area, the emissivity spectra of geologic materials can be quite complex. Many emissivity studies require as many spectral bands in the TIR window as possible.

The inversion for T and e is undetermined because there is always at least one more unknown than the number of measurements. Separation of T and e data from the measured radiance thus requires additional information, determined independently. In the temperature and emissivity separation (TES) algorithm (Gillespie et al., 1998), the additional constraint comes from the regression of minimum emissivity to spectral contrast calculated from laboratory spectra. At least three or four spectral bands are required to measure the spectral difference in images. Therefore, it is necessary to make multispectral measurements to determine land surface temperatures.

ASTER includes a five-band multispectral TIR scanner designed for recovery of land surface “kinetic” temperatures and emissivities (NASA, 1998). The five TIR bands have spectral ranges of 8.125-8.475  $\mu\text{m}$ , 8.475-8.825  $\mu\text{m}$ , 8.925-9.275  $\mu\text{m}$ , 10.25-10.95  $\mu\text{m}$ , and 10.95-11.65  $\mu\text{m}$ , respectively. ASTER’s estimated TIR radiometric accuracy is 1K at 300K, and 3K at 240K. Radiometric precision (radiometric uncertainty) at 300K is = 0.3K (Fujisada and Ono, 1993).

Temperature is not an intrinsic property of land surface materials; it varies with the irradiance history and meteorological conditions. Emissivity is an intrinsic property of the surface and is independent of irradiance. The radiance from a perfect emitter (i.e., a blackbody for which,  $e = 1$ ) increases approximately exponentially, with temperature, as described by Plank’s Law

$$L_{\lambda T} = C_1 / \{\lambda^5 (e^{c_2/\lambda T} - 1)\} \quad (2.3)$$

where,  $C_1 = 2\pi hc^2 = 3.742 \times 10^{-16} \text{Wm}^2$ ,

$C_2 = hc/k = 0.0144 \text{mK}$ ;

$h = \text{Plank’s constant} = 6.62 \times 10^{-34} \text{Js}$ ,

$c = \text{the velocity of light} = 3 \times 10^8 \text{ m/sec.}$ ,

$k = \text{Boltzmann’s constant} = 1.38 \times 10^{-23} \text{JK}^{-1}$  (Prakash, 1996),

$\lambda$  is the central wavelength in meters,

T is the radiant temperature at sensor.

The radiance R emitted from a real surface, however, is less by the factor e (Gillespie et al., 1998):

$$R_{\lambda} = e_{\lambda} B_{\lambda} \quad (2.4)$$

where,  $B$  is the blackbody radiance and  $\lambda$  is wavelength ( $\mu\text{m}$ ). Within its 90 meter pixels, ASTER integrates radiance emitted from a number of surface elements, potentially having different temperatures and composition. The emitted radiance is attenuated during passage through the atmosphere, which also emits TIR radiation. Some of this radiation emitted is transmitted directly into the scanner, some strikes the ground and is then reflected into the scanner. In ASTER TIR pixels, many terrestrial surfaces consist of multi components having different emissivity spectra and temperature. ASTER TIR measurements for such complex surface are not sufficient to estimate all of the unknowns, instead, it is necessary to determine only an effective  $T$  and  $e$  spectrum for each pixel (Gillespie et al., 1998).

More complete documentation of TES is available from NASA. The significant advance of the TES algorithm is to produce unbiased and precise estimates of emissivities, and therefore, improved estimates of land surface temperatures.

For all materials in ASTER spectral library,  $0.94 < e_{\text{max}} < 1.00$ , therefore, the estimated kinetic temperatures should be within  $\pm 2\text{K}$  at  $273\text{K}$  (Gillespie et al., 1998).

Minimums and Maximum Difference (MMD) model is used to estimate TES emissivities and temperatures (Gillespie et al., 1998):

$$\text{MMD} = \max(\beta_b) - \min(\beta_b), \quad (2.5)$$

where,  $\beta_b$  is the spectral wavelength at a band, for ASTER TIR data,  $b = 10 - 14$ .

An empirical relationship predicting  $e_{\text{min}}$  from MMD is used to convert  $\beta_b$  to  $e_b$ . A regression is established using laboratory reflectance and field emissivity spectra. The first step is to find the spectral contrast according to equation (2.5). From which the minimum emissivity is predicted and used to calculate the TES emissivities.

$$e_{\text{min}} = 0.994 - 0.687 * \text{MMD} * 0.737 \quad (2.6)$$

$$e_b = b_b \left( \frac{e_{\text{min}}}{\min(b_b)} \right) \quad (2.7)$$

However, the actual emissivity contrast in a scene element is much greater than the apparent contrast due only to measurement error. For graybodies (e.g. geology materials), MMD is

dominated by measurement error the apparent MMD pro forma, as specified by Monte Carlo simulations:

$$\text{MMD}' = [\text{MMD}^2 - c\text{NE}^2 e^2]^{-1}, \quad c = 1.52 \quad (2.8)$$

Where  $c = 1.52$ , it is an experiential constant,  $\text{MMD}'$  is the corrected contrast,  $\text{NE}^2 e = 0.0032$  is calculated from  $\text{NE}^2 T = 0.3\text{K}$  at  $300\text{K}$ , and the coefficient  $c$  was determined empirically. Equation (2.8) improves the accuracy of TES for graybodies, but at the expense of precision. If  $\text{MMD} < 0.03$ , the loss of precision becomes unacceptable. In this case,  $\text{MMD}'$  is not calculated, and  $e_{\min}$  is not found from equation (2.6), but instead is set to 0.983, value appropriate for water and close to values for vegetation canopies.

The temperature is calculated from the measured, atmospherically corrected radiances  $R$  and the maximum value of the TES emissivity spectrum,

$$T = \frac{C2}{I_{b'}} \left( \ln \left( \frac{e_{b'} C1}{R_b p I_{b'}^5} \right) + 1 \right)^{-1} \quad (2.9)$$

where  $b'$  is the ASTER band for which emissivity  $e_{b'}$  is maximum (Gillespie et al., 1998).

When using digital thermal infrared data, it is important to set two internal blackbody reference temperatures at realistic features. This is accomplished by using a lower and higher reference temperature for the two internal blackbodies in the thermal infrared scanner. These are then related to digital values ranging from 0 to 255 (in case of Landsat data). Any temperatures above the temperature in higher blackbody pre-set reference temperature will be saturated (Zhang, 1997). This means no quantitative temperature analysis can be done, however, it is not a problem for a simple detection.

The detection of a coal fire means that a coal fires causes a mixed pixel anomaly that can be distinguished from the surroundings. If a coal fire in the thermal remote sensing data can be detected, its digital number (DN) should be larger than the background DN plus a constant. The background DN can be derived from the statistical average of the remote sensing data. The variation of the surface temperature and the heterogeneity can be expressed as the standard deviation of the thermal remote sensing data. The standard deviation or two time of it can be taken as the threshold.

### **2.3.3 Surface temperature related to the coal fires**

Coal fires can cause higher temperature on the land surface than the surrounding background. The temperature caused by surface coal fires is normally 400°C higher than the background. The temperature change caused by underground coal fires varies depending on e.g. location, measuring time, weather conditions, etc.

Surface temperatures measured in the coal fire areas in Xinjiang by using a portable infrared thermometer indicated that there were three levels of thermal anomalies, (1) low thermal anomalies without significant changes in texture and color having surface temperatures of up to 20°C higher than the background; 2) medium thermal anomalies with leakage of tarry substances, haloes of sulphur crystals, micro-cracks, and holes in the surface. They are usually 20°C to 120°C above the background temperature; and 3) high thermal anomalies above the sublimation point of sulphur where salmiac deposition, molten rock, big cracks and collapse holes were observed, with the temperatures of about 120°C to 300°C or higher. The highest temperatures were typically located at hilltops over active coal fires, apparently because the higher topographic elevation ensures a longer chimney system to supply the fire with oxygen. The width of individual high-amplitude thermal anomalies usually does not surpass a few meters. (Zhang, 1998; Guan, and Genderen, 1997).

# Chapter 3 Data acquisition and image processing

## 3.1 Data acquisition

As mentioned above, the data used in this study includes three kinds of data, viz. satellite images, maps and literature. Satellite images include Landsat7 ETM+ images, ERS SAR images and ASTER images. Among them, ASTER images were downloaded from the Internet by the author; others were obtained from German researchers who took part in the project of Environmental Monitoring and Evaluation of Coal Fires in Northern China. Hence, ASTER data acquisition will be further elaborated upon in this chapter.

Maps used in this research include a topographical map of Xinjiang (partly), China, with the scale of 1:100,000. It was produced in Russia in 1982. The projection is WGS84, and the coordination system is UTM WGS84 system. In order to use it, the map was scanned. It was used as a base map for geometric correction and registration of images, due to the absence of more accurate topographical data for this research area. Besides, some general geological sketch maps of Xinjiang were also used in this research.

Some literature related to the research area and coal fires were collected as reference for this study, such as the project report on GPS surveying (from Germany) and a book on the geology investigation of coal fire areas in Northern China (in Chinese), etc.

### 3.1.1 ASTER data acquisition

ASTER, Advance Space-borne Thermal Emission and Reflection Radiometer, a satellite launched in December 1999 as a part of NASA's Earth Observing System (EOS), is the only high spatial resolution instrument on the Terra platform. ASTER will be used to obtain detailed maps of land surface temperature, emissivity, reflectance and elevation, whose goal is to obtain a better understanding of the interactions between the biosphere, hydrosphere, lithosphere and atmosphere. ASTER's ability to serve as a 'zoom' lens for the other instruments will be particularly important for change detection and land surface studies. So that it will be particularly advantageous and helpful in the detection and study on coal fires using remote sensing techniques.

Key features of ASTER compared to other optical imagers are: (1) spectral data acquisition with a high spatial resolution of 15 meters in visible and near infrared (VNIR) regions, (2) stereoscopic capability in along track direction, (3) high spectral resolution in short wave infrared (SWIR) region, and (4) high spectral and spatial resolutions in thermal infrared (TIR) region. The radiometric resolution for the low level input radiance is specified, though it is not included in the user requirements. A decrease in photon noise for the low level input radiance is taken into account. The total noise is expected to decrease down to 70% for VNIR bands and 80% for SWIR bands compared to the noise of the high input radiance in this specification. For TIR bands, the low input radiance is specified as 2.5 K or 1.5K depending on bands by considering that the required accuracy is 3K, and the input radiance for bands 10-12 is very low for 200 K blackbody target. Table 3.1 shows the measured radiometric sensitivities with the specified values for the high and low level input radiances which are defined by signal to noise ratio (S/N) for VNIR and SWIR subsystems and noise equivalent temperature difference (NE<sub>T</sub>) for TIR subsystem. The excellent radiometric performance of ASTER can be expected based on the preflight evaluation of PFM on the ground.

**Table 3.1 Radiometric sensitivity**

Subsystem	Band No.	S/N or NE <sub>T</sub> for high level radiance		S/N or NE <sub>T</sub> for low level radiance	
		Specified value	Measured value	Specified value	Measured value
VNIR	1	≥ 140	370 - 278	≥ 40	170 - 78
	2	≥ 140	306 - 256	≥ 40	122 - 74
	3N	≥ 140	202 - 173	≥ 40	70 - 58
	3B	≥ 140	183 - 150	≥ 40	72 - 56
SWIR	4	≥ 140	466 - 292	≥ 35	368 - 63
	5	≥ 54	254 - 163	≥ 13.5	77 - 45
	6	≥ 54	229 - 150	≥ 13.5	73 - 36
	7	≥ 54	234 - 151	≥ 13.5	72 - 35
	8	≥ 70	258 - 165	≥ 17.5	81 - 34
TIR	9	≥ 54	231 - 156	≥ 13.5	73 - 44
	10	≤ 0.3 K	0.17 - 0.07 K	≤ 2.5 K	1.34 - 0.68 K
	11	≤ 0.3 K	0.14 - 0.09 K	≤ 2.5 K	1.27 - 0.63 K
	12	≤ 0.3 K	0.13 - 0.07 K	≤ 2.5 K	1.05 - 0.42 K
	13	≤ 0.3 K	0.09 - 0.05 K	≤ 1.5 K	0.49 - 0.26 K
	14	≤ 0.3 K	0.13 - 0.09 K	≤ 1.5 K	0.65 - 0.33 K

There are two processing level of ASTER data products that ASTER Ground Data System (GDS) produces and provides: Level-1 and Level-2. The ASTER instrument has two types of Level-1 data, Level-1A and Level-1B data. Each group of data are divided into scenes of 60 km in the along-track direction but includes more than 3 km of data to provide an overlap of 5 % with neighboring scenes except for backward stereo band 3B. For band 3B the scene size is 81 km, including an additional overlap of 6 km to compensate for the terrain error contribution and a scene rotation for a large cross-track pointing. The details of ASTER Level-1 data will be introduced because they are mainly used in this study.

(1) Level-1A (Reconstructed, Unprocessed Instrument Data)

The ASTER Level 1A raw data are reconstructed, unprocessed instrument digital counts with ground resolution of 15 m, 30 m, and 90 m for 3 visible and near infrared (VNIR), 6 short wavelength infrared (SWIR) and 5 thermal infrared (TIR) data, the contiguous electromagnetic spectra range of 0.52-0.86  $\mu\text{m}$ , 1.60-2.43  $\mu\text{m}$  and 8.13-11.65  $\mu\text{m}$ , respectively (ASTER User's Guide, 2001). This product contains depacketized, demultiplexed, and re-aligned instrument image data with geometric correction coefficients and radiometric calibration coefficients appended but not applied. This includes correcting for SWIR parallax as well as registration within and between telescopes. The spacecraft ancillary and instrument engineering data are also included. The radiometric calibration coefficients consisting of offset and sensitivity information is generated from a database for all detectors. The geometric correction is the coordinate transformation for band-to-band coregistration. The Level 1A data product consists of the image data, the radiometric coefficients, the geolocation data, and the auxiliary data. For VNIR, SWIR and TIR images, the sizes of each scene are 4100\*4200, 2048\*2100, and 700\*700 pixels, respectively.

(2) Level-1B (Registered Radiance at Sensor)

The Level 1B product contains radiometrically calibrated and geometrically coregistered data for all ASTER channels. The product is created by applying the radiometric and geometric coefficients to the Level 1A data. The bands have been coregistered both between and within telescopes, and the data have been resampled to apply the geometric corrections. As for the Level 1A product, these Level 1B radiances are generated at 15m, 30m, and 90m resolutions corresponding to the VNIR, SWIR, and TIR channels, and the sizes of each scene are 4980\*4200, 2490\*2100, and 830\*700 pixels, respectively.

### 3.1.2 Procedure of downloading ASTER data

ASTER data is free for use, which can be downloaded from the Internet. There are two addresses (<http://asterweb.jpl.nasa.gov/> , or <http://edcimswww.cr.usgs.gov/pub/imswelcome/>) can be entered to order ASTER data. There are three types of data provided to users, level 1A, level 1B, and level 2 data, displayed as the following Table 3.2.

The raw ASTER data downloaded from Internet is transmitted by File Transfer Protocol(FTP). It has to be transformed into an image file. The main steps of transformation of ASTER raw data using ENVI 3.4 are presented as following:

- (1) Open the ASTER raw data by selecting File/Open External File/Generic Formats/HDF, the HDF Dataset Selection dialog opens.

- (2) Select the image data from the HDF Dataset Selection window, total 15 bands, the Available Bands List dialog opens.
- (3) Select the first band data from the Available Bands List dialog, and then click the Load Band button, the related band data is shown on the view window.
- (4) Select File/Save Files As/ERDAS (.lan) File from ENVI menu bar, Output to ERDAS Input Filename dialog opens. Be careful, the arrow button in this window has to be clicked in order to arrange the order of data as the same as it in Available Bands List dialog.
- (5) Select the band data loaded, Output File to ERDAS dialog opens. The directory and output file name has to be entered, the format of output file is defaulted as .lan.
- (6) Repeat the procedure from step (3) to step (5) till all band data are transformed into ERDAS compatible files.

**Table 3.2 ASTER data product list**

Select	Options...				Data set	Number of Granules	Sources	Sensors
	All	None						
<input checked="" type="checkbox"/>	<a href="#">Data set attributes</a>	<a href="#">Other links</a>	<a href="#">Summary document</a>	<a href="#">Detailed document</a>	ASTER LEVEL 1A DATA SET - RECONSTRUCTED, UNPROCESSED INSTRUMENT DATA V002	100 (of 100)	TERRA	ASTER
<input checked="" type="checkbox"/>	<a href="#">Data set attributes</a>	<a href="#">Other links</a>	<a href="#">Summary document</a>	<a href="#">Detailed document</a>	ASTER LEVEL 1B DATA SET REGISTERED RADIANCE AT THE SENSOR V002	18 (of 18)	TERRA	ASTER
<input type="checkbox"/>	<a href="#">Data set attributes</a>	<a href="#">Other links</a>	<a href="#">Summary document</a>	<a href="#">Detailed document</a>	ASTER LEVEL 2 DECORRELATION STRETCH PRODUCT (SWIR) V002	18 (of 18)	TERRA	ASTER
<input type="checkbox"/>	<a href="#">Data set attributes</a>	<a href="#">Other links</a>	<a href="#">Summary document</a>	<a href="#">Detailed document</a>	ASTER LEVEL 2 DECORRELATION STRETCH PRODUCT (TIR) V002	18 (of 18)	TERRA	ASTER
<input type="checkbox"/>	<a href="#">Data set attributes</a>	<a href="#">Other links</a>	<a href="#">Summary document</a>	<a href="#">Detailed document</a>	ASTER LEVEL 2 DECORRELATION STRETCH PRODUCT (VNIR) V002	16 (of 16)	TERRA	ASTER

### 3.2 Description of ASTER data sets

The ASTER data range of latitude and longitude was selected according to the location of research area, whose coordinate of center point is N 43°07' and E 88°12'. There are seven sets of ASTER data downloaded for using in this study, five sets are level 1A data and 2 sets are level 1B data (Table 3.3). The data acquisition time is limited, hence, there is no nighttime data. However, some data sets acquired in winter season, such as data 007, 013, and 135, can

be used and compared to others. Thus, the multi-temporal detection and analysis can be carried out.

**Table 3.3 ASTER data sets**

<b>Number</b>	<b>Data Sets</b>	<b>Level</b>	<b>Date</b>	<b>Local Time</b>	<b>Quality</b>	<b>Clouds</b>
1	007	Level 1A	2000-12-15	13:20:12	High	Yes
2	008	Level 1A	2001-05-24	12:17:06	High	No
3	013	Level 1A	2000-11-04	13:27:05	High	No
4	030	Level 1A	2001-09-04	12:20:36	High	No
5	037	Level 1A	2000-10-12	12:21:33	High	No
6	135	Level 1B	2000-11-29	13:20:27	Middle	Yes
7	173	Level 1B	2001-08-19	12:21:18	High	No

### **3.3 Image processing**

The goal of image processing is to facilitate image interpretation and feature extraction. Image processing described here mainly focuses on geometric correction, image enhancement (spatial, radiometric and spectral enhancement), band combination (color composite), image filtering, contrast stretching, etc. These image-processing techniques are vital for detecting and/or interpreting the land surface characteristics from the images. The flow chart of image processing is shown in Figure 3.1.

#### **3.3.1 Geometric correction and registration**

##### **3.3.1.1 Introduction**

Geometric correction and registration of remote sensing imagery is primarily important for producing scaled maps, for the fusion of multi-sensed and/or multi-temporal data, for integrating the remote sensing data into a geographical information system, and for proper interpretation of information for a specific purpose, such as detection of coal fires.

Image geometric correction is the process of projecting the data onto a plane and making it conform to a map projection system. Assigning map coordinates to the image data is called georeferencing. Since all map projection systems are associated with map coordinates, geometric correction involves georeferencing. This operation aimed to correct geometric distortion in raw image data. Raw digital images usually contain geometric distortions so significant that they cannot be used directly as a map base without subsequent processing.

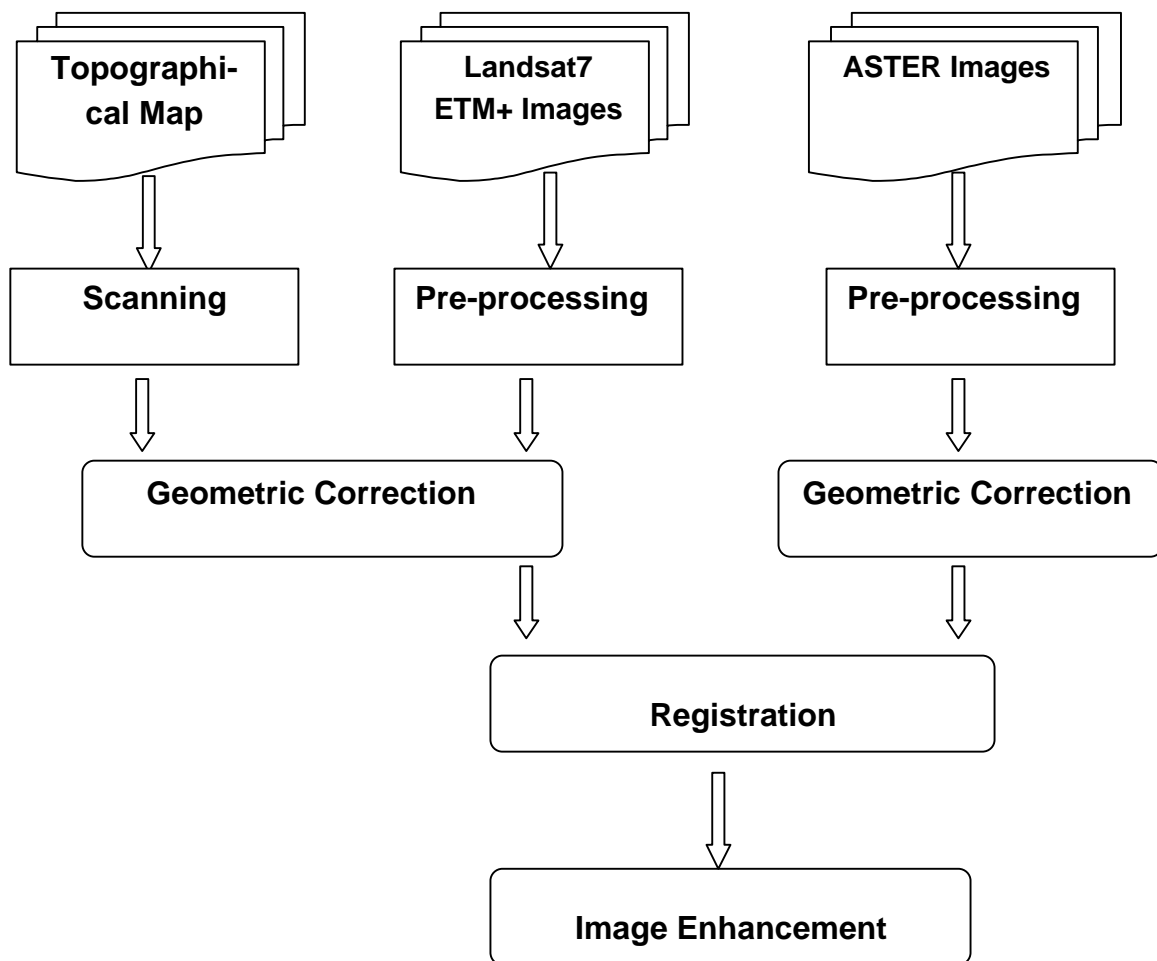


**Figure 3.1** Flow chart of image processing

Registration is for accurate positioning of images relative to a unique coordinate system. This is vital for multi-sensed and/or multi-temporal image data used in detecting or monitoring operations. These different images have to be precisely overlaid sequential data of the same area. In this study, the multi-sensed and multi-temporal image data were registered to the topographical map.

There are several ways of distortions that can occur in a remote sensing image. These distortions can be classified into systematic and non-systematic distortions. The causes and correction of these distortions have been reviewed in literature on image processing. Here, only the method and procedure adopted in this study for image geometric correction and registration are discussed.

### **3.3.1.2 Approach**

In this study, ERDAS Imagine was used as a software tool for geometric correction and registration of images. The data used for geometric correction and registration includes Landsat7 ETM+ images (band1 to band 7, and panchromatic image), ASTER images (band1 to band 14), and the scanned topographical map.

In absence of field control points and other options, the scanned topographical map, with a scale of 1:100,000, served as the base map, which had been georeferenced to the UTM WGS 84 coordinate system. All other data were rectified and registered according to it.

Because it is difficult for the geometric correction from image to the scanned topographical map, Landsat7 TM panchromatic image, with high resolution of 15m, was firstly rectified. After that, other images were rectified using the Landsat7 ETM+ panchromatic image as the master image.

Digital image-to-image rectification basically uses the technique of coordinate transformation. Geometric distortions are corrected by analyzing well-distributed ground control points (GCPs) occurring in two images, respectively. Some distinct features that might make good control points were selected as GCPs. The coordinate transformation equations can be expressed as the following (Lillesand and Kiefer, 2000),

$$x = f_1 (X,Y), \quad y = f_2 (X,Y) \quad (3.1)$$

where, (x,y) = distorted image coordinates

(X,Y) = correct coordinates

$f_1, f_2$  = transformation functions

In ERDAS, there are six geometric correction models provided, among them, a polynomial transformation model was used in image-to-image rectification for this study.

A second order polynomial transformation was selected. The root mean square error (RMS) is calculated and displayed automatically by ERDAS,

X: The X value of the RMS error.

Y: The Y value of the RMS error.

Total: The total value of the RMS error.

The minimum number of GCPs can be calculated according to the following equation:

$$N = (t + 1)(t + 2) / 2 \quad (3.2)$$

where,  $t$  = polynomial transformation parameter, here  $t = 2$ , hence, the minimum number of GCPs equals 6. Six control points, however, may not be sufficient for a scene. In this study, 12 to 14 control points were used.

Great care was taken in selecting the GCPs and efforts were made to keep the root mean square (RMS) error to a minimum in order to achieve the best fitting and desired sub-pixel accuracy of registration. Considering the spatial resolution of ASTER and Landsat7 ETM+ images, all GCPs' RMS errors are less than 1.0 pixel, Figure 3.4 shows a sample of GCPs results.

**Table 3.4 The results of GCPs**

Point #	Point ID	Color	X Input	Y Input	Color	X Ref.	Y Ref.	Type	X Residual	Y Residual
1	GCP #1		2676.546	-2762.489		605742.289	4768471.233	Control	-0.516	-0.388
2	GCP #2		2720.495	-3678.555		603714.514	4754772.027	Control	-0.009	0.009
3	GCP #3		1274.460	-4025.605		581544.707	4753544.132	Control	0.057	-0.222
4	GCP #5		1368.526	-3100.479		585626.221	4767014.643	Control	-0.223	0.290
5	GCP #6		2379.517	-605.503		607707.926	4801273.714	Control	-0.230	0.031
6	GCP #7		1760.510	-3524.502		590125.323	4759664.682	Control	0.256	0.233
7	GCP #10		3854.805	-2029.634		625134.788	4776133.745	Control	0.045	0.021
8	GCP #9		771.506	-1788.522		580735.252	4788073.524	Control	-0.161	-0.122
9	GCP #12		4308.969	-3964.636		626127.215	4746193.765	Control	0.008	0.041
10	GCP #4		1850.498	-1545.507		597236.169	4788764.449	Control	0.639	0.118
11	GCP #8		3672.471	-2635.547		620697.041	4767644.820	Control	0.124	0.022
12	GCP #11		1367.715	-1056.969		591595.192	4797314.659	Control	0.011	-0.033

### 3.3.1.3 Registration

In many cases, images of one area that are collected from different sources must be used together. To be able to compare separate images pixel by pixel, the pixel grids of each image must conform to the other images in the database. The tools for rectifying image data are used to transform disparate images to the same coordinate system. Image-to-image registration involves georeferencing only if the reference image is already georeferenced. Registration is the process of making an image conform to another image. After the geometric correction for all images, registration can be carried out because images have been georeferenced into a unique coordinate system. Figure 3.2 shows an example of registration of five ASTER images and a Landsat7 ETM+ image.

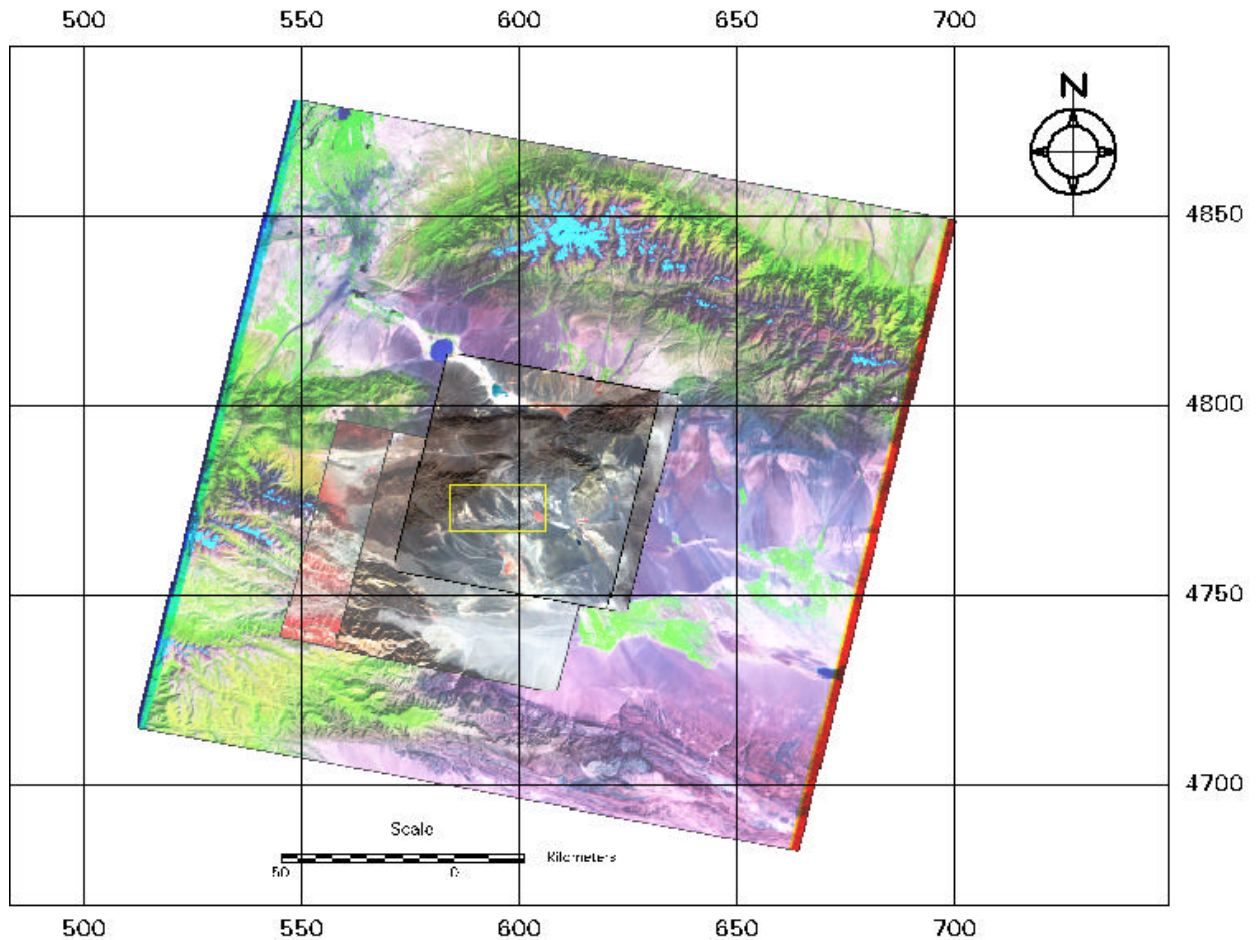


**Figure 3.2** The overlay of five rectified ASTER images (007,008,173,013,037) registered with a Landsat7 ETM+ image together. The square marked area is the study area (unit: km).

### 3.3.2 Image enhancement

Image enhancement is the process of making an image more interpretable for a particular application (Faust, 1989). Enhancement makes important features of raw, remotely sensed data more interpretable to the human eye. Enhancement techniques are often used instead of classification techniques for feature extraction—studying and locating areas and objects on the ground and deriving useful information from images. The techniques to be used in image enhancement depend upon:

Your data—You must know the parameters of the bands being used before performing any enhancement.

Your objective—You must have a clear idea of the final product desired before enhancement is performed.

Your expectations—what you think you are going to find.

Your background—your experience in performing enhancement.

Normally, image enhancement involves techniques for increasing the visual distinctions between features in a scene. The objective is to create “new” images from the original image data in order to increase the amount of information that can be visually interpreted from the data. The enhanced images can be displayed interactively on a monitor or they can be recorded in a hardcopy format. There are no simple rules for producing the single best image for a particular application. Often several enhancements made from the same raw image are necessary.

ERDAS provides three functions for image enhancement, spatial enhancement, radiometric enhancement, and spectral enhancement. The first two are further discussed below.

### **3.3.2.1 Spatial enhancement**

As previously mentioned, the goal of image enhancement is to improve the visual interpretability of imagery. The process of visually interpreting digitally enhanced imagery attempts to optimize the complementary abilities of the human mind and computer. The mind is excellent at interpreting spatial attributes on an image and is capable of selectively identifying obscure or subtle features.

Spatial enhancement functions will enhance images based on the values of individual and surrounding pixels, which includes following,

- (1) Convolution? Use a matrix to average small sets of pixels across an image;
- (2) Non-directional edge? Average the results from two orthogonal 1st derivative edge detectors;
- (3) Focal analysis? Enable you to perform one of several analyses on class values in an image file using a process similar to convolution filtering;
- (4) Texture? Define texture as a quantitative characteristic in an image;
- (5) Adaptive filter? Vary the contrast stretch for each pixel depending upon the DN values in the surrounding moving window;
- (6) Statistical filter? Produce the pixel output DN by averaging pixels within a moving window that fall within a statistically defined range;
- (7) Resolution merge? Merge imagery of differing spatial resolutions;
- (8) Crisp? Sharpen the overall scene luminance without distorting the thematic content of the image.

Some of those functions can help to improve the visual interpretability, such as focal analysis, adaptive filter, statistical filter, but some cannot. Figure 3.3 shows some examples of spatial enhancement functions. The features of coal area (dark spots) are clearer after enhancement using an adaptive filter, focal analysis, and statistical filtering techniques.

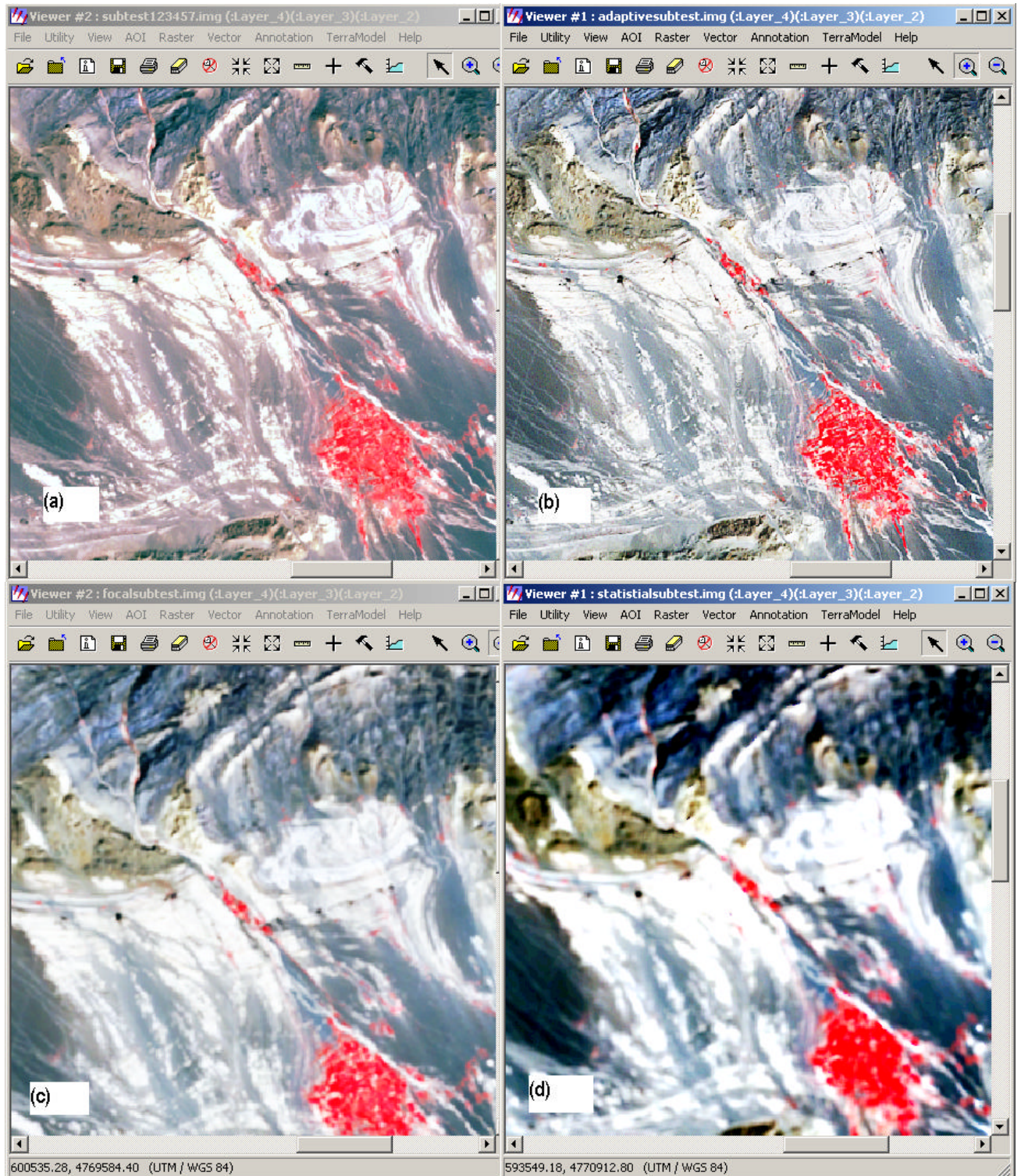


**Figure 3.3** The results of spatial enhancement, (a) original Landsat7 ETM+ image, (b) Adaptive filter enhancement, (c) Focal analysis enhancement, (d) Statistical filter enhancement.

From Figure 3.3, for spatial enhancement, adaptive filter enhancement is the best to be used in the image interpretation because the contrast and edge of features are appropriate and clear, respectively.

### 3.3.2.2 Radiometric enhancement

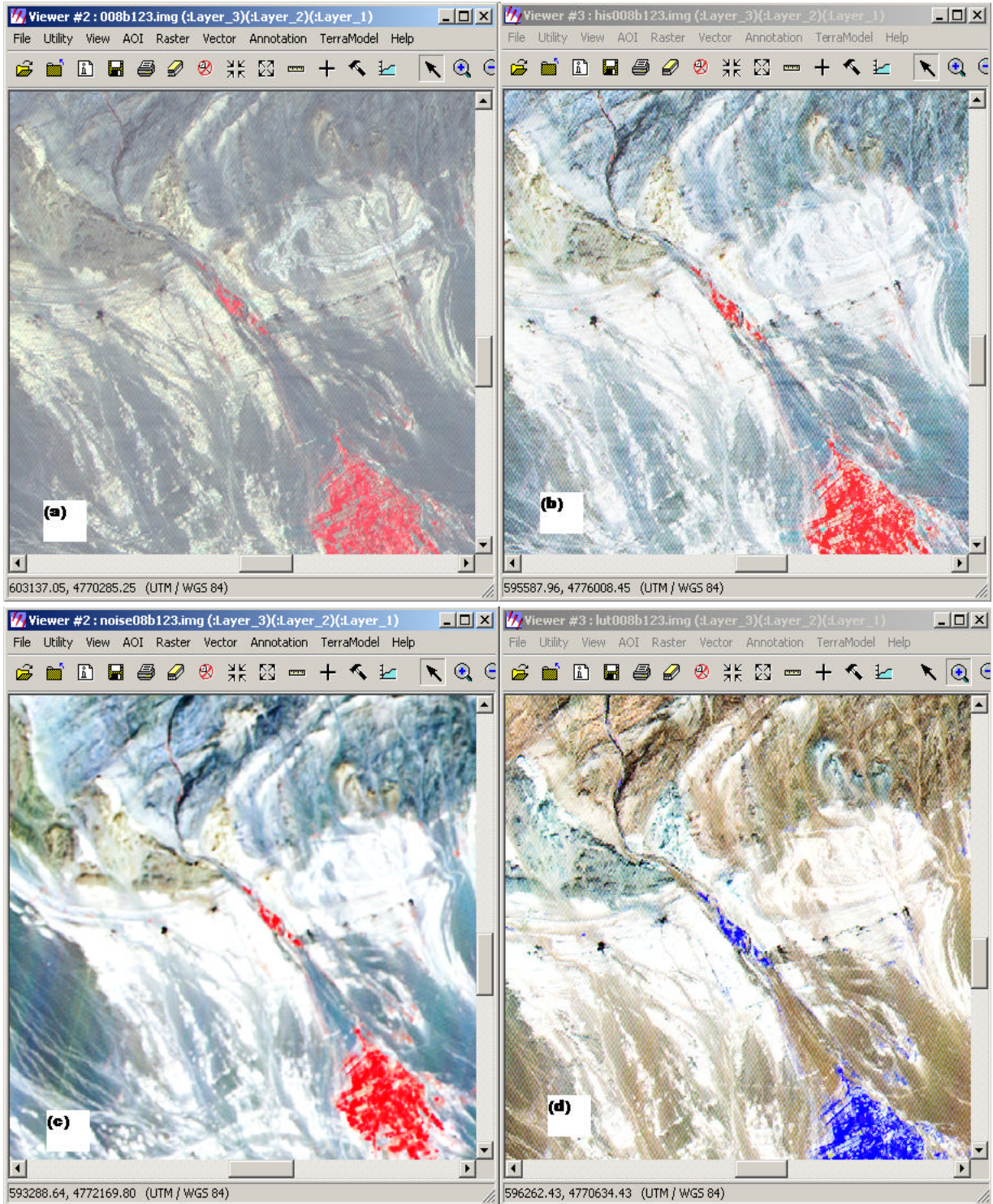
Radiometric enhancement functions enhance the image using the values of individual pixels within each band. These functions involve,

- (1) LUT (Lookup Table) stretch? Create an output image that contains the data values as modified by a lookup table;
- (2) Histogram equalization? Redistribute pixel values with a nonlinear contrast stretch so that there are approximately the same number of pixels with each value within a range;
- (3) Histogram match? Mathematically determines a lookup table that converts the histogram of one image to resemble the histogram of another;
- (4) Brightness inversion? Allow both linear and nonlinear reversal of the image intensity range;
- (5) Haze reduction? Reduce the effect of haze;
- (6) Noise reduction? Remove noise using an adaptive filter;
- (7) Destripe TM data? Remove striping from a raw image data.

Among them, functions as histogram equalization, noise reduction, and haze reduction were continually used for every raw ASTER image. There is an interesting case occurred during operating brightness inversion for a ASTER imagery, some sites of coal fire areas potentially selected are distinctly shown as bright spots, however, the shadows are shown as light yellow colour. But on the original image, the shadows are displayed the same as coal fire areas as black colour. Some results of radiometric enhancement are shown in Figure 3.4. As mentioned above, there is no simple “best” way of enhancement, for example, image (c), (d), (e) in Figure 3.4 are better for image interpretation, these images were enhanced using noise reduction, LUT stretch and haze reduction respectively, and subsequently histogram equalized. After comparing these enhancement results, the LUT stretch image is best for the detection of coal mines and coal seams, which are clearly shown as dark areas.

Meanwhile, on the screen the stereo display generated from band3 nadir and backward images is also used for the interpretation. From the display (shown in Figure 3.5), the geological structure, such as folds, faults and strata, and geomorphology are effectively interpreted.

**DETECTION OF COAL FIRES IN XINJIANG (CHINA) USING REMOTE SENSING TECHNIQUES**



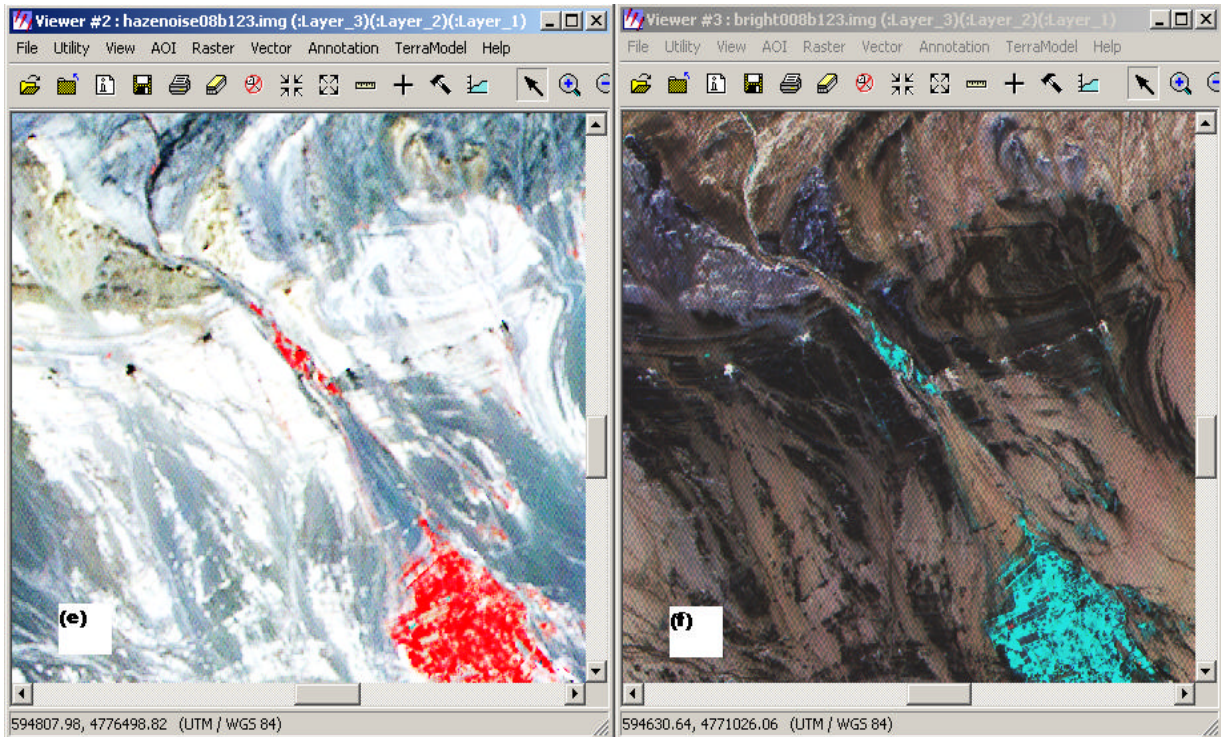


**Figure 3.4** The results of radiometric enhancement. (a) original ASTER image, (b) enhancement of histogram equalization, (c) enhancement of noise reduction, (d) enhancement of LUT stretch, (e) enhancement of haze reduction, and (f) enhancement of brightness inversion.

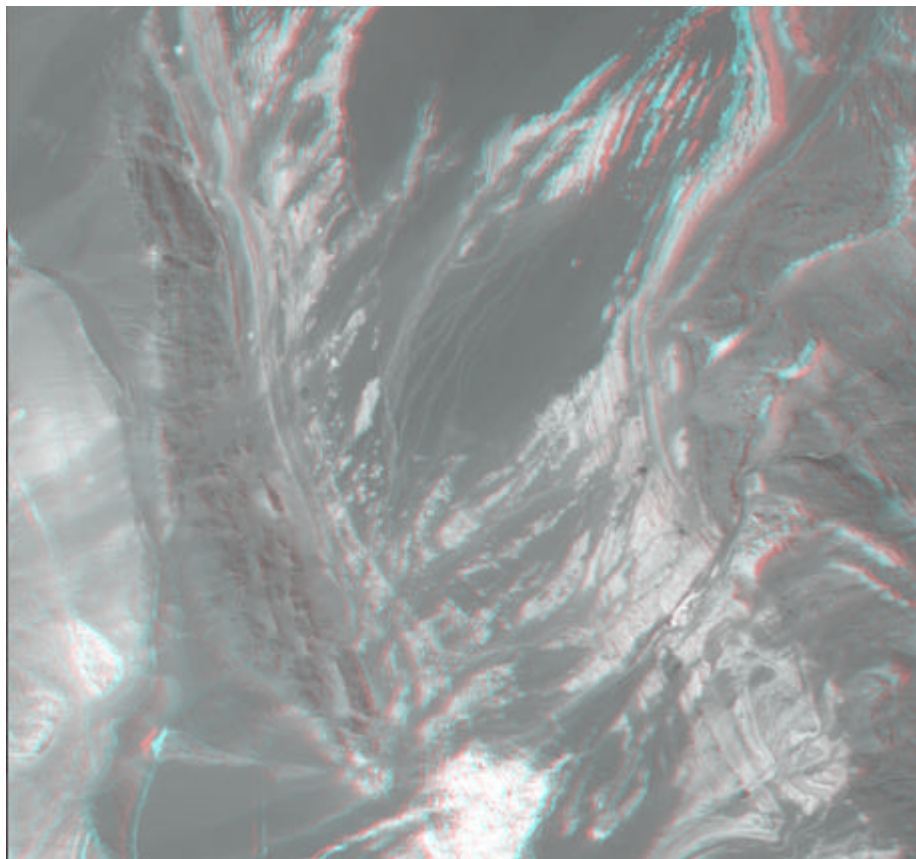


**Figure 3.5** The stereo display of study area.

Image enhancement techniques are also applied to the Landsat7 ETM+ band 6 image. However, for the nighttime band6 image, the original one is better than enhanced one for the detection of thermal anomalies due to the very subtle changes caused by these thermal anomalies, which disappear when the image is enhanced (e.g. histogram equalized). The band6 nighttime data and the sub-images created based on the interpretation of the potential coal fire areas are shown in Figure 3.6 and 3.7.

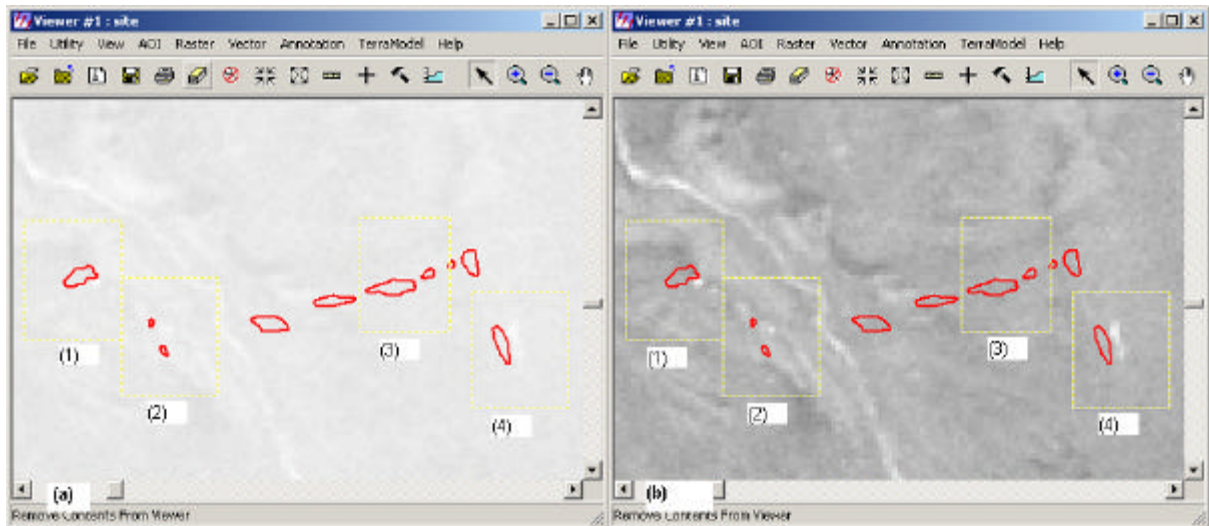


**Figure 3.6 Landsat7 ETM+ band 6 nighttime image, (a) low gain, (b) high gain.**

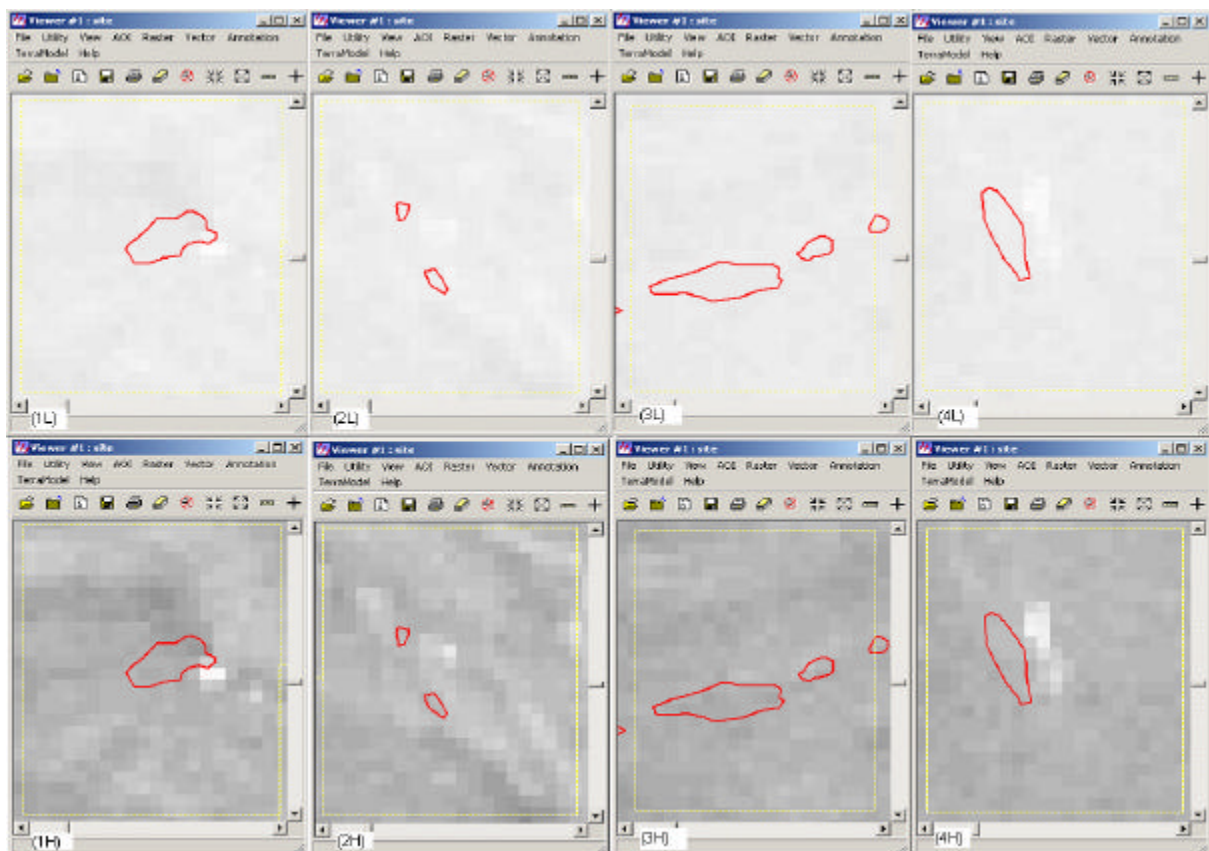


**Figure 3.7 The image enhanced sub-images of Landsat7 ETM+ band 6 nighttime low and high gain data.**

# Chapter 4 Feature extraction and image fusion

## 4.1 Feature extraction

Image classification can be performed through three kinds of modes: spatial pattern recognition, spectral pattern recognition, and temporal pattern recognition. Spatial pattern recognition involves the categorization of image pixels on the basis of their spatial relationship with pixels surrounding them, such as image texture, pixel proximity, feature size shape, directionality, repetition, and context will be considered in this procedure. These types of classification help to make the spatial synthesis done by human analyst during the visual interpretation process. Spectral pattern recognition refers to use pixel-by-pixel spectral information as the basis for land cover classification. Temporal pattern recognition uses time as an aid in feature identification. In fact, these three procedures, as image classifiers, are mostly used in a hybrid mode. For example, during the feature extraction of coal fires, not only the spatial patterns are recognized, such as location, size, texture, and potential directionality, but also the spectral recognition is incorporated during the detection of thermal anomalies with the help of DN value analysis of thermal data.

In this study, only features related to coal fires and some major objects, such as rivers and roads, are extracted. Normally, multispectral data are used to perform the classification, and the spectral pattern present within the data each pixel is used as the numerical basis for categorization. Different feature types manifest different combinations of DNs based on their inherent spectral reflectance and emittance properties (Lillesand and Kiefer, 2000).

Typically, the DNs constituting a digital image are recorded over such numerical ranges as 0 to 255, 0 to 511, 0 to 1023, or higher. These ranges represent the set of integers that can be recorded using computer coding scales, respectively (That is,  $2^8=256, 2^9=512, \dots, 2^{12}=4096$ ). For example, DNs in Landsat7 ETM+ data are recorded in the range of 0 to 255, DNs in ASTER VNIR, SWIR data are recorded in the range of 0 to 255, and TIR data in the range of 0 to 4095.

The use of computer-assisted analysis techniques permits the spectral patterns in remote sensing data to be more fully examined. It also permits the data analysis process to be largely automated, providing cost advantages over visual interpretation techniques. However, just as humans are somewhat limited in their ability to interpret spectral patterns, computers are somewhat limited in their ability to evaluate spatial patterns (Lillesand and Kiefer, 2000). Therefore, the combination approach of visual and numerical techniques will be used in this study for image interpretation.

An image contains a detailed record of features on the ground at the time of data acquisition. The exact characteristics useful for any specific task and the manner in which they are considered depend on the field of application. However, most applications consider the following basic characteristics, or variations of them: shapes, sizes, patterns, tones (or colour), textures, shadows, sites, association, and resolution (Olson, 1960). The process of convergence of evidence used in image interpretation will successfully increase the accuracy and detail of the interpretation.

The image interpretation process can often be facilitated through the use of image interpretation keys, which provide useful reference and help interpreters evaluate the information presented on the images in an organized and consistent manner. It provides guidance about the correct identification of features or conditions on the images. Two general types of image interpretation keys exist, differentiated by the methods of diagnostic features. A selective key contains numerous example images with supporting text. The interpreter selects the example that most nearly resembles the feature or conditions found on the image under study. An elimination key is arranged so that the interpretation proceeds step by step from the general to the specific and leads to the elimination of all features or conditions except the one being identified (Lillesand and Kiefer, 2000). A combination method of the selective key and the elimination key is used in this study. The method will be discussed in chapter 4.3.

During the image interpretation, the linear features as narrow as a few meters can be seen on images due to the reflectance contrasting sharply with that of their surroundings, such as folds, faults, drainage network, and roads. On the other hand, some objects much larger than the ground resolution pixel size may not be apparent if they have a very low reflectance contrast with their surroundings. Features may be visible in one band but not in another, or they may be shown in different colors in different modes of band combinations. These can all be used to interpret the features related to specific applications.

Image enhancement techniques not only enhance the data but also improve the efficiency of classification operations. Images used in feature extraction here all are enhanced to make the image interpretation easier. For ASTER data, the VNIR data, with the high resolution of 15 meters, have some advantage in the image interpretation, especially, band 3 nadir and backward looking image provide a stereo viewing capability, which is very helpful in feature extraction and image interpretation. An increase in the number of bands in the SWIR region from band 4 to 9 will enhance the surface lithologic mapping capability. The addition of 5 spectral bands in TIR spectral region can help to derive accurate surface temperatures and emissivities. Improved radiometric resolutions and accuracies are required to enhance interpretation. Hence, ASTER data, as an important data source, are firstly used in the feature extraction and the image interpretation.

## 4.2 Image interpretation of geology, geomorphology, drainage network and infrastructure

The precondition to detect the area of coal fires is to detect the area of coal seams, which is especially related to the geological features. Besides, the features of coal fires can also be interpreted after analyzing the geological structures and rock features. Hence, the first step of feature extraction is on geology.

The optical band images of Landsat7 ETM+ and ASTER, with high spatial resolution, can be used to study coal fire areas. These images can enhance the data to highlight the major areas of burnt caprock and geological structural features with the help of suitable image processing techniques. Especially, ASTER visible band data, with the high resolution of 15 m and stereo mode, is more useful during image interpretation and feature extraction. For example, in this study area, ASTER VNIR data was stereo displayed on the computer screen or hard copy map, and features related to the geology, geomorphology and major objects on the ground can be seen clearly. Even a subsidence area can be detected in one of roughly expected coal fire areas by means of stereo display on the screen where the area of interest can be enlarged. Many band combinations were tried to produce color composites from the Landsat7 ETM+ and ASTER data. The best view results for geological interpretation were the combinations of TM bands 6,5,4 (Genderen and Guan et al., 1997), and ASTER bands 3,2,1, allocated to red, green and blue respectively. In the view of that combination, the different colors of rocks can generally show the different types of rock.

Feature extraction of geology mainly involves the identification of rock types and rock structures (folds, faults, fractures). The satellite images provide the advantage of large area or synoptic coverage and the ability to analyze multispectral bands quantitatively in terms of DN<sub>s</sub>, which permits the application of computer processing and enhance certain compositional properties of earth materials. There is an obvious syncline in the study area, and the folded rock layers dip inward from both sides toward the axis of it. The syncline axis is directed from west to east. The coal seams are partly surface exposed both south and north of the synclinal axis. The coal seams are mainly distributed within the folds and buckles.

Various terrain characteristics are important for terrain evaluation because the terrain conditions are contributing factors that affect the spontaneous combustion of coal. The principal terrain characteristics that can be estimated by means of visual image interpretation are bedrock type, landform, dip and strike, soil texture, local drainage conditions, etc. For example, the direction and gradient of the folded strata can be interpreted and estimated by means of the stereo viewing of ASTER data and assist to detect potential coal fire areas. Besides, loca-

tion of mines, coal dumps, the roads and other important infrastructure have to be interpreted for a better understanding the local conditions.

Image interpretation for geomorphological identification and evaluation is based on a systematic observation and evaluation of key elements, such as topography, drainage pattern and texture, erosion, image tone, vegetation and land use. For ASTER VNIR images, the drainages and roads can be seen clearly due to the high resolution. The drainage network, roads, railroads, can be extracted from the image with the help of the scanned topographical map. The key elements, such as mountain areas, piedmont areas, alluvial fans, alluvial plains, and urban area can also be identified with the help of an anaglyph and the scanned topographical map.

The result of feature extraction for geology, geomorphology, drainage network and roads are shown in Figure 4.1. It indicates that there is drainage network located on the alluvial fan area. There is little vegetation in the study area, in that case, the atmosphere there would be dryer and the solar heating is relatively large. This can contribute to the spontaneous combustion of coal.

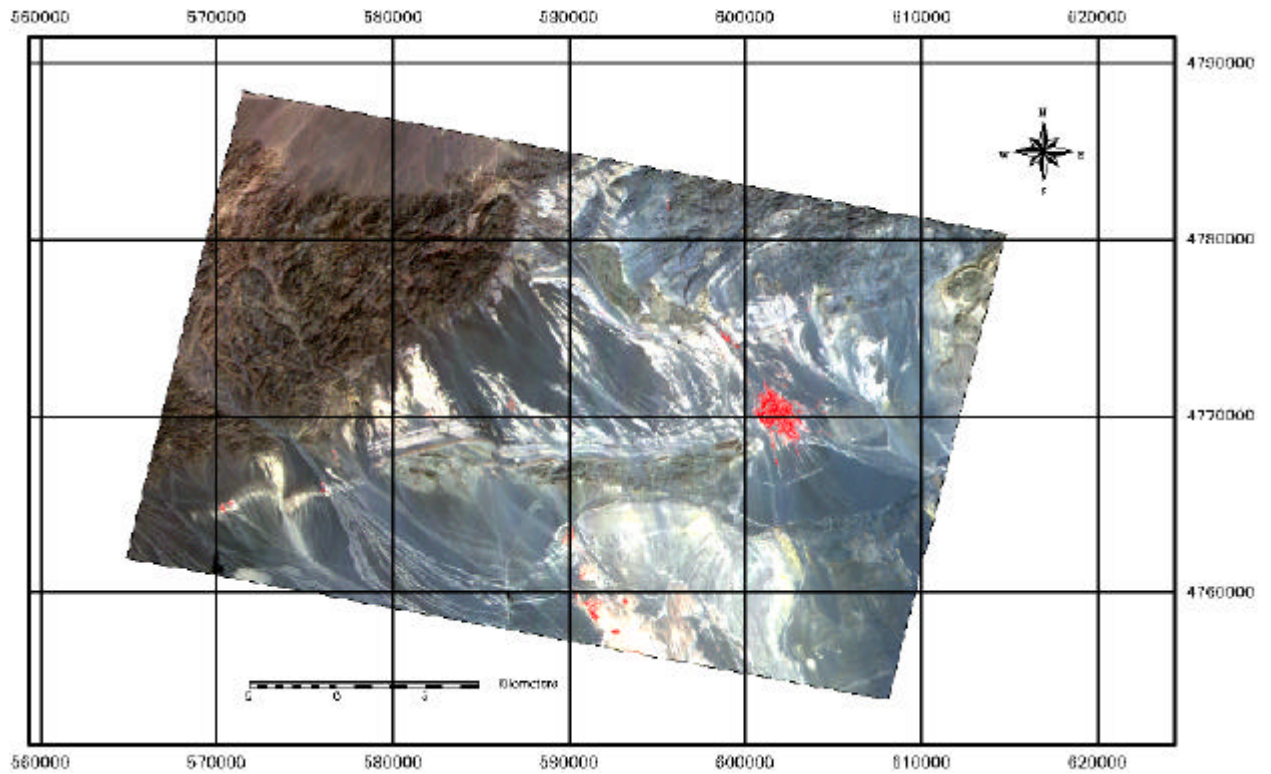


Figure 4.1 (a) ASTER image of study area used for the feature extraction.

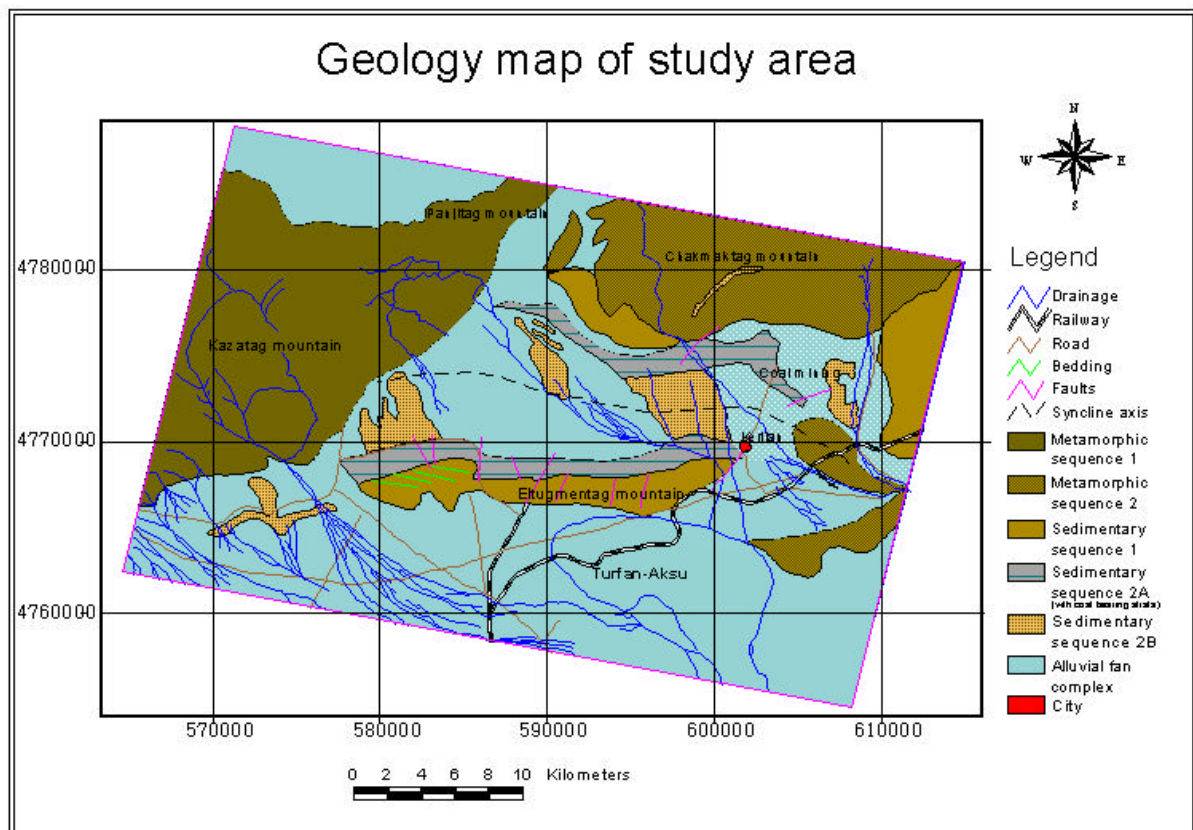


Figure 4.1 (b) Feature extraction of geological map of study area.

### 4.3 Feature properties of coal fires

Detection of coal fires aims to distinguish the characteristics of the coal fires from the surroundings. Remote sensing data acquired in the visible, near infrared and short wave region of the electromagnetic spectrum sometimes can be used for the detection of the reflectance and radiance characteristics caused by the coal fires (Reddy et al., 1993).

Some feature changes caused by coal fires can be directly or indirectly detected by remote sensing data. In coal fire areas, the materials on the land surface can roughly be classified into two groups, one is the material unaffected by the coal fires, such as the original formations, soil and vegetation; the other is the material affected by coal fires, such as the burnt rocks, cracks, subsidence, ashes, etc. Pyro-metamorphic rocks are the rocks metamorphosed by the heat coming from the adjacent combustion of the coal seams. The changes of heating are different and are depending on the distance from the coal fires.

Burnt rock is a general term used in coal fire areas, which describes the thermally metamorphosed rocks originating from heating of the overlying rocks by burning of coal seams. Burnt rocks can be classified according to characteristics, such as color, texture, structure and their metamorphic temperatures (Guan, 1963). Some baked rock still keeps its original texture under a relative low temperature (340-800°C), but change its color because of dehydration and oxidation. Porcelanite is a kind of pyro-metamorphic rock that is formed after the original rock is heated under a medium temperature (600-1400 °C). The rock became very hard and formed a ceramic texture. The color of the original rock has been greatly changed. Molten rock is a kind of pyro-metamorphic rock that is formed after the original rock heated under high temperatures (1500-2000 °C), commonly distributed in the burnt center or near coal seams. The granulated minerals in the rocks smelted to form a kind of black lava (Zhang et al., 2000). The original rocks commonly have dark color and low moisture content. When rock heated by a coal fire at a temperature of 340-800°C, it will induce dehydration and oxidation. Oxidation changes gray, green color rocks to yellow, orange, red or brown color rocks. At the first phase of this stage, rocks are becoming dry and turn into yellow color. At the second phase of this stage, with an increasing amount of heat received the rock becomes purple, brick red or brown. With the temperature continually increasing, the rock will be changing from iron minerals to hematite.

The thermal infrared image of the remote sensing data provides a data source for the detection of the thermal anomalies caused by coal fires. The thermal infrared data from Landsat TM have been used for coal fire detection (Mansor et al., 1994; Sarf et al., 1995; Prakash et al., 1995; Zhang et al., 1995). In this study, the thermal band data from Landsat7 ETM+ and ASTER are used to provide the direct indicators in the detection process of the thermal

anomalies of the coal fires. The data provide information about the temperature of surface materials.

For the thermal infrared, various times of the day can be utilized in data acquisition. Many factors influence the selection of an optimum time for acquiring thermal infrared data. Image analysis must be taken into consideration the effects of diurnal temperature variation.

Comparing to biomaterial fires, coal fires are much more stable and have lower temperatures and smaller sized areas (Robinson, 1991). Solar heating is a main factor in the natural heating process. During the day time, the surface temperatures increase and make the detection of coal fires difficult. The variations of the surface temperatures caused both by topography or by surface heterogeneity make coal fire detection difficult. The thermal anomalies can only be detected from the remote sensing data when the temperatures of coal fires are high enough. Also the spatial resolution of the sensor limits the capability for the detection of coal fires.

DN (digital number) values are the indicators of material radiation on the ground surface. If a coal fire can be detected in the thermal remote sensing data, its DN values should be larger than background DN values plus a constant. The background DNs can be derived from the statistical average of the remote sensing data. The variation of the surface temperature and the heterogeneity can be expressed as the standard deviation ( $s$ ) of the thermal remote sensing data. A simple way to select the constant is the trial and error method in the known fire area (Saraf et al., 1995). The standard deviation or two times of standard deviation can be taken as the constant. However, for the whole area of an image, the factors of topography and heterogeneity are too different to recognize the thermal anomalies accurately; besides, the environmental noise (differential heating due to sun-slope exposure) may be large and also negatively affect possible detection.

In this study, a combination method of selective keys and elimination keys are used for the general interpretation of coalfields and coal fires. Firstly, some potential coal fire areas (36 sites) were selected on ASTER data (Figure 4.2) having the following criteria:

- (1) The coal mine entrances are scattered along the coal bearing layers both at the south and north side of the synclinal axis;
- (2) The dark areas on VNIR image are the potential coal mining areas. In the lower part of the image, there are also three dark areas, one of them (part A in Figure 4.2) is recognized as cloudy shadow because it does not exist in other ASTER VNIR images and Landsat7 ETM+ visible image; part B in Figure 4.2 may be a distribution area for further coal transportation because it is along to a railway line (according to the topog-

raphic map); part C in Figure 4.2 is a shadow caused by a very narrow and deep ravine, which can be interpreted clearly on the stereo model prepared consisting of ASTER band 3 nadir and backward looking data;

- (3) The selected areas locate either at the bottom of slopes or in the strike area;
- (4) GPS data acquired in the field (shown as black colour point cluster in Figure 4.2);
- (5) Literature on the introduction of this study area and the report on general geology.

Figure 4.2 shows the selected potential coal mining areas (magenta polygons), the black point clusters are GPS locations of actual coal fire areas, and the yellow boundary indicates the research area.

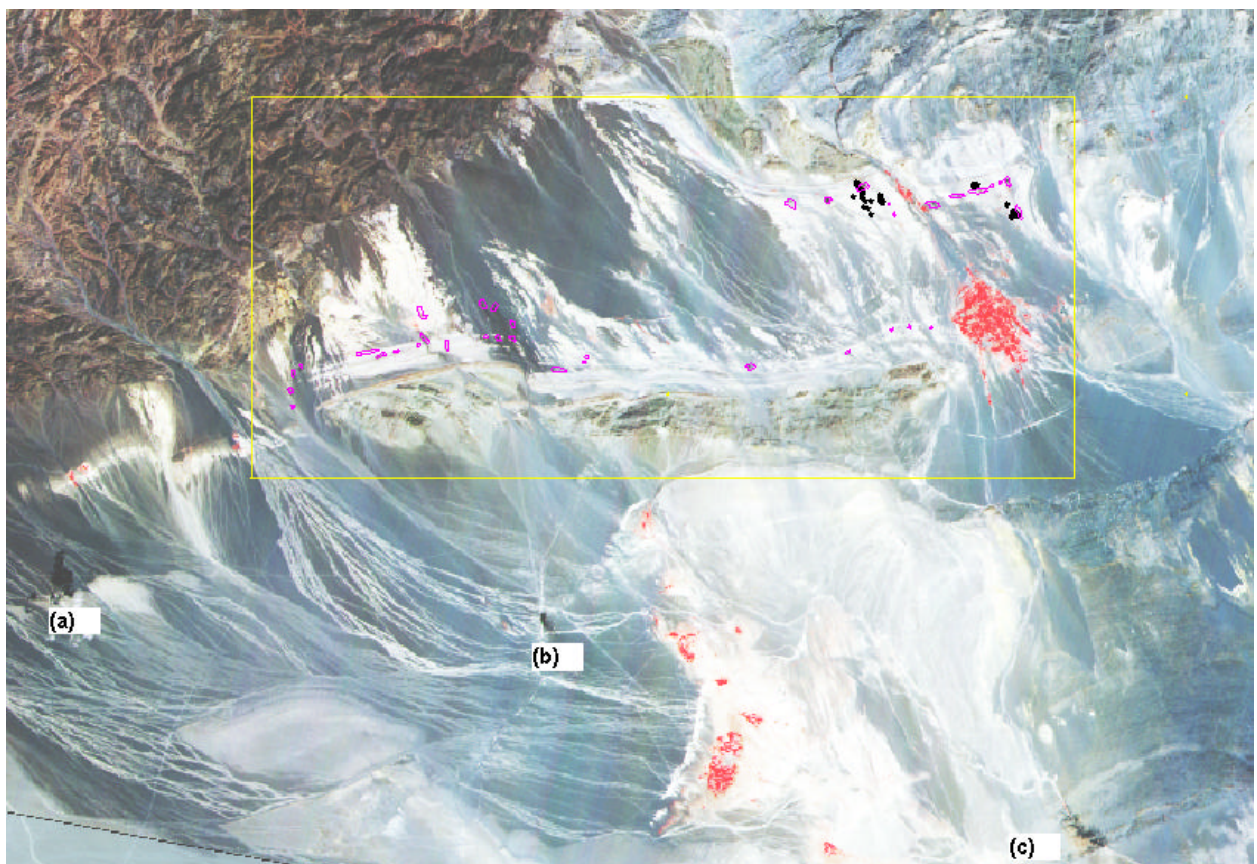


**Figure 4.2 Potential coal mining areas extracted from an ASTER visual image.**

#### **4.4 Calculating temperatures from Landsat7 ETM+ and ASTER TIR data**

Thermal anomalies are a result of coal fires. These anomalies are expressed on the image as higher DN values, on the land surface they indicate higher temperatures compared to the surroundings. However, the ability for the detection of thermal anomalies using space-borne thermal remote sensors is very much depending on the coal fire conditions, e.g. surface ex-

posed fires or deep seated coal fires, with only cracks at the surface. From the introduction on temperature calculation in Chapter 2 temperatures are related to radiances, spectral ranges, and emissivities. Generally, the emissivity changes are in the range of 0.7 to 1.0 according to different materials, for most natural materials the emissivity value is between 0.8-1.0. For sandstone and burnt rocks, the emissivity can be selected as 0.95 (Prakash, 1995). For the different sensors the methods of temperature calculation are different as well. The methods of temperature calculation from Landsat7 ETM+ data and ASTER data are discussed below.

#### 4.4.1 Method of temperature calculation from Landsat7 ETM+ band 6 data

For Landsat7 ETM+ band 6, during 1G product rendering image pixels are converted to units of absolute radiance using 32 bit float point calculations. Pixel values are then scaled to byte values prior to media output. In addition to normally observed saturation (i.e. 0, 255) two other types of detector saturation can occur. An analog to digital converter may saturate below 255 counts at the high end, or above 0 at the low end. The detector saturation parameters identify these levels for each detector. The analog electronic chain may saturate at a radiance corresponding to a level below 255 counts and above 0 counts on the low end. The detector saturation parameters also identify these levels for each detector.

Some researchers have already used Landsat TM band 6 for estimating the surface temperature (Gupta, 1991, Kahle, 1980, Mansor *et al.*, 1994, Saraf *et al.*, 1995, Prakash *et al.*, 1997, and Zhang *et al.*, 1997). The methods of temperature calculation from Landsat7 ETM+ band 6 are according to their research results. The approach of calculation is briefly divided into three steps:

(1) Converting image DN values to spectral radiance

The DN values can be converted back to radiance units using the following equation:

$$\text{Radiance} = \text{gain} * \text{DN} + \text{offset} \quad (4.1)$$

The radiance is also expressed as

$$L_l = \frac{L_{\max} - L_{\min}}{Q_{\text{cal max}} - Q_{\text{cal min}}} * (Q_{\text{cal}} - Q_{\text{cal min}}) + L_{\min} \quad (4.2)$$

where:  $L_l$  = spectral radiance in watts/(meter squared\*ster\* $\mu\text{m}$ ),

$$Q_{\text{cal min}} = 0,$$

$$Q_{\text{cal max}} = 255,$$

$$Q_{\text{cal}} = \text{Digital Number}.$$

The  $L_{min}$  and  $L_{max}$  are the spectral radiances for each band at digital numbers 1 to 255, respectively. It is a representation of how the output Landsat7 ETM+ Level 1G data products are scaled in radiance units. The  $L_{min}$  and  $L_{max}$  correspond to the radiance at the minimum and maximum quantized and calibrated data digital number ( $Q_{calmin} = 0$ ,  $Q_{calmax} = 255$ ), respectively. Two sets of  $L_{min}$  and  $L_{max}$  are listed in Table 4.1. The first set should be used for 1G products created before July 1, 2000 and the second set for 1G products created after July 1, 2000. For band 6 data, they are not changed.

**Table 4.1 Two sets of  $L_{min}$  and  $L_{max}$  of Landsat7 ETM+ 1G data.**

	Low gain		High gain	
	$L_{min}$	$L_{max}$	$L_{min}$	$L_{max}$
Before July 1,2000	0.0	17.04	3.2	12.65
After July 1,2000	0.0	17.04	3.2	12.65

The calibration of band 6 data has been analyzed by two of the Landsat7 Science Team investigators using vicarious calibration methods. The results of the vicarious calibration indicate that though the instrument may be quite stable, there is a consistent bias of about 0.31  $W/(m^2 \cdot sr \cdot \mu m)$  in the absolute calibration. This bias is not neglectable in the conversion of temperature. This value has to be subtracted after the conversion (Landsat7 Program Report for FY 2000, 2000).

It should be noted that Landsat7 ETM+ images are acquired in either low or high gain state. Gain selection is controlled by the Mission Operations Center (MOC) and is performed by changing the reference voltage for the analog to digital convertor. The science goal in switching gain states is to maximize the instrument's 8-bit radiometric resolution without saturating the detectors. This requires matching the gain state for a given scene to the expected brightness conditions. For all bands, the low gain dynamic range is approximately 1.5 times the high gain dynamic range. It makes sense, therefore, to image in low gain mode when surface brightness is high and in high gain mode when surface brightness is lower. Table 4.2 lists the target/specification minimum saturation levels for all bands in both the low and high gain states.

**Table 4.2 Landsat7 ETM+ Dynamic Range watts / ( $m^2 \cdot sr \cdot \mu m$ )**

	Low Gain	High Gain
Band	Minimum Saturation Level	Minimum Saturation Level
1	285.7	190.0
2	291.3	193.7
3	225.0	149.6
4	225.0	149.6

5	47.3	31.5
6	17.21	12.78
7	16.7	11.10
8	235.0	15.63

In this study, the Landsat7 ETM+ data was created in 1999, hence, for the low gain band 6 data, the equation (4.2) can be converted to

$$L_{1l} = \left( \frac{17.04 - 0}{255} \right) * DN + 0 - 0.31 = 6.682 * 10^{-2} * DN - 0.31 \quad (4.3)$$

and for the high gain band 6 data, the equation (4.2) can be converted to

$$L_{1h} = \left( \frac{12.65 - 3.2}{255} \right) * DN + 3.2 - 0.31 = 3.706 * 10^{-2} * DN + 2.89 \quad (4.3)'$$

We can get the relation curve of DN and radiance by radiance calculation according to equation (4.3) and (4.3)', the calculation is shown in Table 4.3, and the curve is illustrated in Figure 4.3.

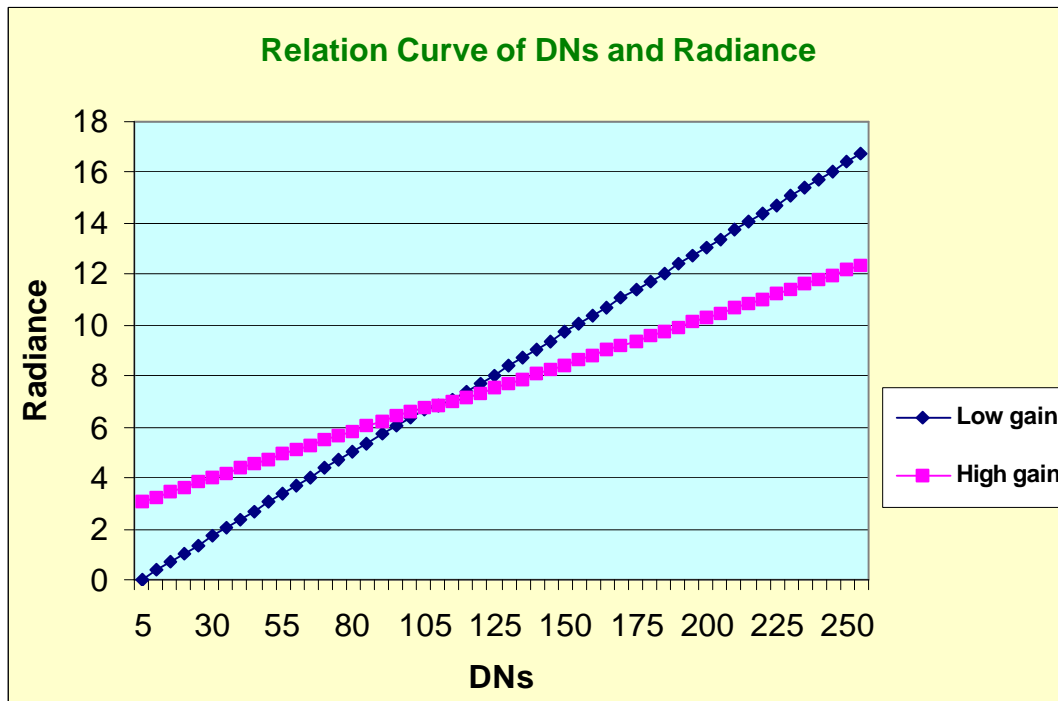


Figure 4.3 The relation curve of DN and radiance from Landsat7 ETM+ band6 low and high gain data.

(2) Converting the spectral radiance to radiant temperature

For Landsat7 ETM+ band 6 data, the radiant temperature can be converted from spectra radiance according to Planck's radiation equation, which expresses the relation between the spectral radiance and the radiant temperature:

$$L_{\lambda} = \frac{eC_1\lambda^{-5}}{\rho \left[ \exp\left(\frac{C_2}{\lambda T}\right) - 1 \right]} \quad (4.4)$$

The radiant temperature can be converted as the following equation:

$$T_R = \frac{C_2}{\lambda \ln \left[ \left( \frac{eC_1\lambda^{-5}}{\rho L_{\lambda}} \right) + 1 \right]} \quad (4.5)$$

where,  $C_1$  and  $C_2$  are constant, and

$$C_1 = 2\pi^5 h^6 c^2 / 15 = 3.742 \times 10^{-16} \text{ Wm}^2,$$

$$C_2 = hc/k = 0.0144 \text{ mK (mentioned in Chapter2);}$$

$\lambda$  is the central wavelength in meters,  $e$  is the emissivity of the object, for the ground materials, a constant  $e = 0.97$  was used in this study.

The radiant temperature, or brightness temperature, is named the effective at-satellite temperature of the viewed Earth-atmosphere system under an assumption of unity emissivity ( $e = 1$ ) and using pre-launch calibration constants listed below. The conversion formula is:

$$T_R = \frac{K_2}{\ln \left( \frac{K_1}{L_{\lambda}} + 1 \right)} \quad (4.6)$$

where,  $T_R$  = effective at-satellite temperature in Kelvin,

$L_{\lambda}$  = spectral radiance in watts/( $\text{m}^2 \cdot \text{sr} \cdot \mu\text{m}$ ),

$K_1$  = calibration constant 1, for Landsat7 ETM+ sensor,  $K_1 = 666.09 \text{ watts}/(\text{m}^2 \cdot \text{sr} \cdot \mu\text{m})$ ,

$K_2$  = calibration constant 2, for Landsat7 ETM+ sensor,  $K_2 = 1282.71 \text{ degree Kelvin (URL-2, 2001)}$ .

Hence, the equation (4.6) can be changed as the following equation:

$$T_R = \frac{1282.71}{\ln\left(\frac{666.09}{L_I} + 1\right)} \quad (4.7)$$

(3) Changing the radiant temperature to the surface temperature

The radiant temperature, or the brightness temperature, can be changed into the kinetic or true temperature of the surface according to the formula below:

$$T_R = e_I^{1/4} T_K \quad (4.8)$$

or, 
$$T_K = T_R * e_I^{-1/4} \quad (4.9)$$

$$T_K' = T_K - 273.16 \quad (4.10)$$

where,  $T_R$  is the radiant temperature,  $T_K$  is the surface temperature (Kelvin),  $T_K'$  is the surface temperature in degree Celsius. During this step, the emissivity on the surface must be known (Becker, 1987; Becker and Raffy 1987; Becker and Li, 1990a, b; Coll *et al.*, 1994; Gaikovich 1994; Hook *et al.*, 1992). Normally the emissivity value is between 0.8-1 for most natural materials except water and snow. For the sandstone, shale and the burnt rocks the emissivity can be selected as 0.97 (Li,1985; Nerry *et al.*, 1990; Salisbury and D'Aria, 1992; Zhang 1998).

The surface temperature can be calculated according to the equations (4.3), (4.3)', (4.7), (4.9) and (4.10). Here is an example of temperature calculation from Landsat7 ETM+ band6 low and high gain data, the results are shown in blue and magenta color, respectively. The emissivity is taken as  $e = 0.97$  (Table 4.2). DN values are ranging from 5 to 255. From the results, the relation curve of DN's and surface temperatures can be obtained, which is shown in Figure 4.4, assuming a constant emissivity ( $e = 0.97$ ). The results in blue and magenta column are from band 6 low gain and high gain, respectively.

Table 4.3 Temperature calculation from Landsat7 ETM+ band 6 low and high gain data (partly).

1	DN	$L_{\lambda l}$	$L_{\lambda h}$	$T_{RI}$	$T_{KI}$	$T_{KI}'$	$T_{RH}$	$TKh$	$T_{KH}'$	J	K	L	M
2	5	0.0241	3.0753		125.424	126.383	146.777	238.305	240.127				
3	10	0.3582	3.2606		170.378	171.680	-101.480	240.912	242.753				
4	15	0.6923	3.4459		186.706	188.134	-85.026	243.426	245.287				
5	20	1.0264	3.6312		198.044	199.557	-73.603	245.857	247.736				
6	25	1.3605	3.8165		207.035	208.618	-64.542	248.212	250.109				
7	30	1.6946	4.0018		214.625	216.266	-56.894	250.496	252.411				
8	35	2.0287	4.1871		221.269	222.960	-50.200	252.717	254.648				
9	40	2.3628	4.3724		227.225	228.962	-44.198	254.877	256.826				
10	45	2.6969	4.5577		232.655	234.433	-38.727	256.983	258.947				
11	50	3.031	4.743		237.668	239.484	-33.676	259.037	261.017				
12	55	3.3651	4.9283		242.341	244.193	-28.967	261.042	263.038				
13	60	3.6992	5.1136		246.730	248.616	-24.544	263.003	265.013				$L_{\lambda l}=6.682*10^{-2}*DN+0.31$
14	65	4.0333	5.2989		250.878	252.796	-20.364	264.922	266.947				$L_{\lambda h}=3.706*10^{-2}*DN+2.89$
15	70	4.3674	5.4842		254.820	256.768	-16.392	266.800	268.840				
16	75	4.7015	5.6695		258.581	260.557	-12.603	268.642	270.695				
17	80	5.0356	5.8548		262.183	264.187	-8.973	270.448	272.515				$T_R = \frac{K_2}{\ln\left(\frac{K_1}{L_\lambda} + 1\right)}$
18	85	5.3697	6.0401		265.644	267.674	-5.486	272.220	274.301				$K1=666.09$
19	90	5.7038	6.2254		268.979	271.035	-2.125	273.961	276.055				$K2=1282.71$
20	95	6.0379	6.4107		272.199	274.280	1.120	275.672	277.779				
21	100	6.372	6.596		275.317	277.421	4.261	277.354	279.474				$T_K = T_R * \epsilon_\lambda^{-1/4}$
22	105	6.7061	6.7813		278.340	280.468	7.308	279.009	281.141				$\epsilon = 0.97$
23	107.5	6.87315	6.87395	279.819	281.958	8.798	279.826	281.965	8.805				
24	110	7.0402	6.9666	281.277	283.427	10.267	280.637	282.783	9.623				$T_K' = T_K - 273.16$
25	115	7.3743	7.1519	284.135	286.307	13.147	282.241	284.399	11.239				
26	120	7.7084	7.3372	286.920	289.113	15.953	283.822	285.991	12.831				
27	125	8.0425	7.5225	289.637	291.851	18.691	285.379	287.561	14.401				
28	130	8.3766	7.7078	292.290	294.524	21.364	286.915	289.108	15.948				
29	135	8.7107	7.8931	294.885	297.139	23.979	288.430	290.635	17.475				
30	140	9.0448	8.0784	297.425	299.698	26.538	289.925	292.141	18.981				
31	145	9.3789	8.2637	299.913	302.205	29.045	291.400	293.628	20.468				
32	150	9.713	8.449	302.352	304.663	31.503	292.857	295.096	21.936				
33	155	10.0471	8.6343	304.746	307.075	33.915	294.297	296.546	23.386				

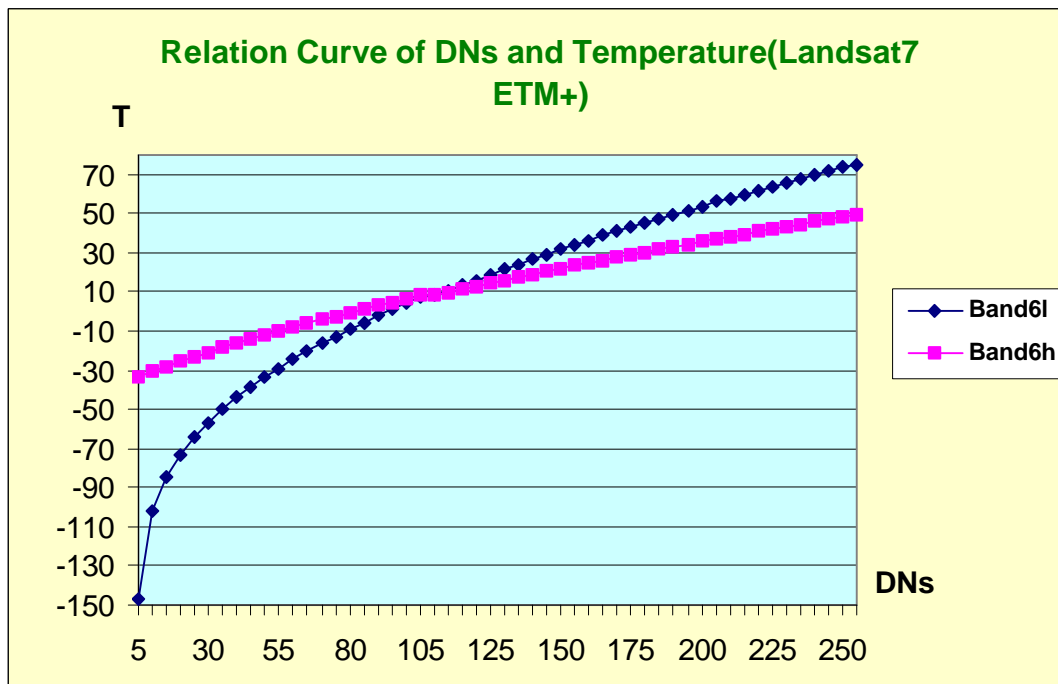


Figure 4.4 Relation curve of DN's and surface temperatures for Landsat7 band 6 data, blue and magenta line are the curve of low gain and high gain data, respectively.

It should be noted that there is a cross point at which DN is equals about 107.5, when DNs less than 107.5, for each pixel (for each radiance value), the DNs on the high gain image are smaller than which on the low gain image; when DNs larger than 107.5, the case is just opposite.

For a pixel on the band6 nighttime image (Row, Column, 646, 1994), the following DN values (82, 61) are given in low and high gain respectively. Using the transfer function the following temperatures are derived,  $-7.56^{\circ}\text{C}$ ,  $-7.76^{\circ}\text{C}$  for the low and high gain bands respectively. The difference is minimal using the two gain settings.

#### 4.4.2 Method of temperature calculation from ASTER TIR data

For ASTER TIR data, there are 5 bands data from band 10 to 14. The temperature is calculated here from ASTER level-1B TIR data because Level-1B product contains radiometrically calibrated data for all ASTER channels. Unit conversion coefficients, which is defined as radiance per 1DN, are used to convert from DN to radiance. Radiance (spectral radiance) is expressed in unit of  $\text{W}/(\text{m}^2 \cdot \text{sr} \cdot \mu\text{m})$ . It is the basic policy that the unit conversion coefficient will be kept in the same values throughout mission life (ASTER user's guide, 2001). The relation between DN values and radiances is shown below and illustrated in Figure 4.5.

- (1) A DN value of zero is allocated to dummy pixels.
- (2) A DN value of 1 is allocated to zero radiance.
- (3) A DN value of 254 is allocated to the maximum radiance for VNIR and SWIR bands.
- (4) A DN value of 4094 is allocated to the maximum radiance for TIR bands.
- (5) A DN value of 255 is allocated to saturated pixels for VNIR and SWIR bands.
- (6) A DN value of 4095 is allocated to saturated pixels for TIR bands.

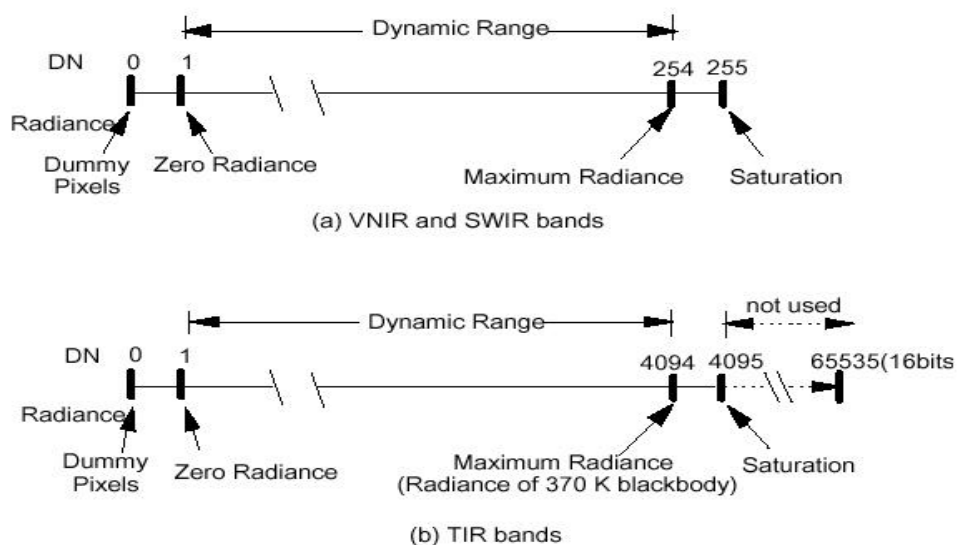


Figure 4.5 Relation between DN values and radiances of VNIR, SWIR bands (a) and TIR bands (b).

Similarly, the temperature calculation from ASTER level-1B TIR data is also divided into three steps.

(1) Converting the radiance values (DNs) to spectral radiance

The maximum radiances depend on both the spectral bands and the gain settings, which are shown in Table 4.4. Maximum radiances for high and low gains are basically defined as those for normal gain divided by nominal gain except for band 3N and 3B for high gain. For band 3N and 3B, the maximum radiance is slightly smaller than the value calculated above which may be saturated because of a large offset.

The unit conversion coefficients can be calculated as follows:

$$L_{ni} = L_{maxi} / 253 \text{ (VNIR and SWIR bands)} \quad (4.11)$$

$$L_{ni} = L_{maxi} / 4093 \text{ (TIR bands)} \quad (4.12)$$

where  $L_{ni}$  : the unit conversion coefficient from DN to radiance of band  $i$ ,

$L_{maxi}$  : the maximum radiance of band  $i$ .

**Table 4.4 Maximum radiance of 370 K blackbody**

Band No.	Maximum radiance (w/m <sup>2</sup> .sr.μm)			
	High gain	Normal gain	Low gain 1	Low gain 2
1	170.8	427	569	N/A
2	179.0	358	477	
3	106.8	218	290	
4	27.5	55.0	73.3	73.3
5	8.8	17.6	23.4	103.5
6	7.9	15.8	21.0	98.7
7	7.55	15.1	20.1	83.8
8	5.27	10.55	14.06	62.0
9	4.02	8.04	10.72	67.0
10	N/A	28.17	N/A	N/A
11		27.75		
12		26.97		
13		23.30		
14		21.38		

For example, for band 10,

$$L_{ni} = 28.17 / 4093 = 0.006882 = 6.882 \cdot 10^{-3}$$

Therefore, the unit conversion coefficients from DN to radiance of each TIR band can be calculated. Table 4.5 shows the calculated unit conversion coefficients of each band.

**Table 4.5 Unit conversion coefficients**

Band No.	Coefficient (W/(m <sup>2</sup> •sr•μm)/DN)			
	High gain	Normal gain	Low gain 1	Low gain 2
1	0.676	1.688	2.25	N/A
2	0.708	1.415	1.89	
3	0.423	0.862	1.15	
4	0.1087	0.2174	0.290	0.290
5	0.0348	0.0696	0.0925	0.409
6	0.0313	0.0625	0.0830	0.390
7	0.0299	0.0597	0.0795	0.332
8	0.0209	0.0417	0.0556	0.245
9	0.0159	0.0318	0.0424	0.265
10	N/A	<b>6.882*10<sup>-3</sup></b>	N/A	N/A
11		<b>6.780*10<sup>-3</sup></b>		
12		<b>6.590*10<sup>-3</sup></b>		
13		<b>5.693*10<sup>-3</sup></b>		
14		<b>5.225*10<sup>-3</sup></b>		

From the relation mentioned above the radiance value can be obtained from DN values as follows.

$$L_{\lambda i} = (DN-1) * L_{ni} \tag{4.13}$$

Where,  $L_{\lambda i}$  is the radiance value of band i with the unit of W/(m<sup>2</sup>•sr•μm).

(2) Converting the spectral radiance to radiant temperature

The brightness temperature product is at its core a conversion from radiance to temperature units. For a given wavelength, this relationship is explicitly defined by the Planck function. For an ASTER thermal infrared channel, the Planck function must be integrated with the normalized spectral response function for that channel. Assuming that the spectral response function is known, this computation can be evaluated to be within any practical precision limit, certainly well within the limits of the precision of the input radiance data. Since the dominant sources of imprecision and error are

the uncertainty of the input radiance data (Level-1B product) and the uncertainty of the spectral response functions, which are themselves tied to the validation of the Level 1B product, validation of this product is "piggy-backed" to the validation of the Level-1B, radiance at sensor product (ASTER user's guide, 2001). It should be noted that the quantity being reported by this product is "at sensor", not "at surface". As such, strict agreement with ground measurements is not an issue, and field experiments are not envisioned.

The radiant temperature, or brightness temperature, is the apparent observed temperature, assuming a surface emissivity of 1.0 (i.e., as if the object were a blackbody). The calculations are performed using the radiance at sensor as input, *no atmospheric correction* is included for this procedure. It can be calculated according to equation (4.5) and (4.6). However, for ASTER data, K1 and K2 have to be calculated according to the following equations:

$$K_{1i} = \frac{eC_1 I_i^{-5}}{p} \quad (4.14)$$

$$K_{2i} = \frac{C_2}{I_i} \quad (4.15)$$

where,  $\lambda_i$  is the central wavelength in meter of each TIR band,  $K_{1i}$  and  $K_{2i}$  are the calibration constants for each TIR band. Here,  $e = 1$  (blackbody).  $C_1$  and  $C_2$  are constants as the same as above.

ASTER TIR subsystem was designed to record 200 to 370 degrees Kelvin. The algorithm is constrained only by the fact that it requires unsaturated input radiance values. The algorithm should work on TIR data acquired during the day or night and over land, clouds, water, or anything else not hotter than about 120°C or colder than about -100°C (ASTER user's guide, 2001).

### (3) Changing the radiant temperature to the surface temperature

Similarly, this conversion can be performed based on the equations (4.9) and (4.10).

Here is an example is given of surface temperature calculation from ASTER TIR data. The results listed in Table 4.6 were calculated from band 10 data, the calculations from other bands are similar to it (the results calculated from band11 to band14 are not listed here). The surface temperatures calculated from each band are shown in Figure 4.6. It indicates that the temperatures related to a certain DNs are degressive.

Table 4.6 Temperature calculation from ASTER TIR data

1	A	B	C	D	E	F	G	H	I	J	K	L
DN	$L_{\lambda 10}$	$L_{\lambda 10}$	$\lambda_{10}$	$K_{110}$	$K_{210}$	$T_{R10}$	$T_{K10}$	$T_{k10}'$				
2	1500	6.882E-03	10.316	8.295E-06	3032.999	1735.986	305.255	307.589	34.429			
3	1550	6.882E-03	10.660	8.295E-06	3032.999	1735.986	307.021	309.367	36.207			
4	1600	6.882E-03	11.004	8.295E-06	3032.999	1735.986	308.749	311.109	37.949		$L_{\lambda i} = (DN-1) * L_{\lambda i}$	
5	1650	6.882E-03	11.348	8.295E-06	3032.999	1735.986	310.443	312.816	39.656		Ln10	$6.882 * 10^{-3}$
6	1700	6.882E-03	11.693	8.295E-06	3032.999	1735.986	312.104	314.489	41.329		Ln11	$6.780 * 10^{-3}$
7	1750	6.882E-03	12.037	8.295E-06	3032.999	1735.986	313.733	316.132	42.972		Ln12	$6.590 * 10^{-3}$
8	1800	6.882E-03	12.381	8.295E-06	3032.999	1735.986	315.333	317.744	44.584		Ln13	$5.693 * 10^{-3}$
9	1850	6.882E-03	12.725	8.295E-06	3032.999	1735.986	316.905	319.327	46.167		Ln14	$5.225 * 10^{-3}$
10	1900	6.882E-03	13.069	8.295E-06	3032.999	1735.986	318.449	320.884	47.724			
11	1950	6.882E-03	13.413	8.295E-06	3032.999	1735.986	319.968	322.414	49.254			
12	2000	6.882E-03	13.757	8.295E-06	3032.999	1735.986	321.462	323.920	50.760		$K_{1i} = \frac{\epsilon C_1 \lambda_i^{-5}}{\pi}, \epsilon = 1$	
13	2050	6.882E-03	14.101	8.295E-06	3032.999	1735.986	322.933	325.401	52.241		$K_{2i} = \frac{C_2}{\lambda_i}$	
14	2100	6.882E-03	14.445	8.295E-06	3032.999	1735.986	324.381	326.860	53.700		$C1 = 3.742 * 10^{-16} Wm^2$	
15	2150	6.882E-03	14.789	8.295E-06	3032.999	1735.986	325.807	328.298	55.138		$C2 = 0.0144 mK$	
16	2200	6.882E-03	15.134	8.295E-06	3032.999	1735.986	327.213	329.714	56.554		$T_R = \frac{K_2}{\ln\left(\frac{K_1}{L_2} + 1\right)}$	
17	2250	6.882E-03	15.478	8.295E-06	3032.999	1735.986	328.598	331.110	57.950		$T_K = T_R * \epsilon_{\lambda}^{-\frac{1}{K}}, \epsilon = 0.97$	
18	2300	6.882E-03	15.822	8.295E-06	3032.999	1735.986	329.965	332.487	59.327		$T_K' = T_K - 273.16$	
19	2350	6.882E-03	16.166	8.295E-06	3032.999	1735.986	331.312	333.845	60.685			
20	2400	6.882E-03	16.510	8.295E-06	3032.999	1735.986	332.642	335.185	62.025			
21	2450	6.882E-03	16.854	8.295E-06	3032.999	1735.986	333.955	336.508	63.348			
22	2500	6.882E-03	17.198	8.295E-06	3032.999	1735.986	335.251	337.814	64.654			
23	2550	6.882E-03	17.542	8.295E-06	3032.999	1735.986	336.531	339.104	65.944			
24	2600	6.882E-03	17.886	8.295E-06	3032.999	1735.986	337.796	340.378	67.218			
25	2650	6.882E-03	18.230	8.295E-06	3032.999	1735.986	339.046	341.637	68.477			
26	2700	6.882E-03	18.575	8.295E-06	3032.999	1735.986	340.281	342.882	69.722			
27	2750	6.882E-03	18.919	8.295E-06	3032.999	1735.986	341.502	344.113	70.953			
28	2800	6.882E-03	19.263	8.295E-06	3032.999	1735.986	342.710	345.330	72.170			
29	2850	6.882E-03	19.607	8.295E-06	3032.999	1735.986	343.904	346.533	73.373			
30	2900	6.882E-03	19.951	8.295E-06	3032.999	1735.986	345.086	347.724	74.564			
31	2950	6.882E-03	20.295	8.295E-06	3032.999	1735.986	346.255	348.902	75.742			
32	3000	6.882E-03	20.639	8.295E-06	3032.999	1735.986	347.412	350.068	76.908			

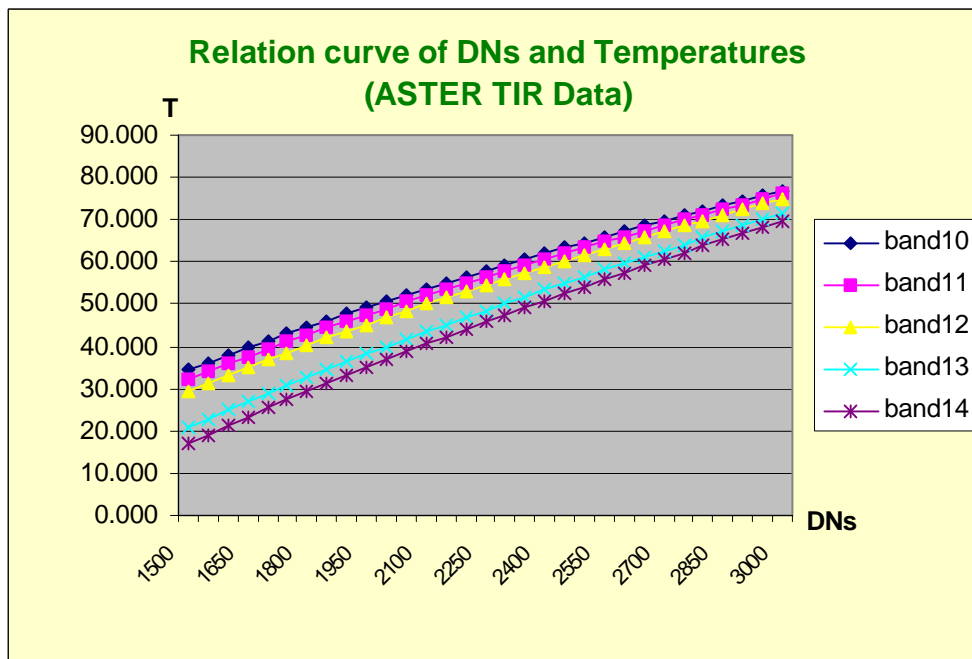


Figure 4.6 the relation curves of DN and surface temperatures from ASTER TIR data.

For the same pixel mentioned above on the ASTER TIR image (Row, Column, 874,274), the following DN values of 1616, 1616, 1803, 2169, and 2238 are given in band10 to band14 respectively. Using the transfer function the following temperatures are derived, 38.50°C, 36.41°C, 40.36°C, 45.77°C, and 45.40°C, respectively. The differences of temperature results between Landsat7 and ASTER TIR data is mainly due to the fact that the data is acquired during different seasons.

#### **4.4.3 Temperature conversion from Landsat7 ETM+ band6 and ASTER TIR images**

According to above methods of temperature calculation from Landsat7 ETM+ band6 and ASTER TIR data, the thermal infrared image can be converted to the temperature-image, from which the temperature information for each pixel is shown on the image, in other words, the surface temperatures of each pixel can be directly obtained from that image. This conversion can be carried out using the function of Model Maker of ERDAS.

The function of temperature conversion from Landsat7 ETM+ band6 nighttime image is indicated below (Figure 4.7). The function can be expressed as the following according to the equations mentioned above:

For high gain image:

$$1282.71 / \text{LOG} ( 666.09 / ( 3.706 * 10^{\text{POWER} - 2 * \$n1\_nightsub1(2) + 2.89} + 1 ) * 0.97 \\ \text{POWER} - 0.25 - 273.16;$$

For low gain image:

$$1282.71 / \text{LOG} ( 666.09 / ( 6.682 * 10^{\text{POWER} - 2 * \$n1\_nightsub1(1) - 0.31} + 1 ) * 0.97 \\ \text{POWER} - 0.25 - 273.16.$$

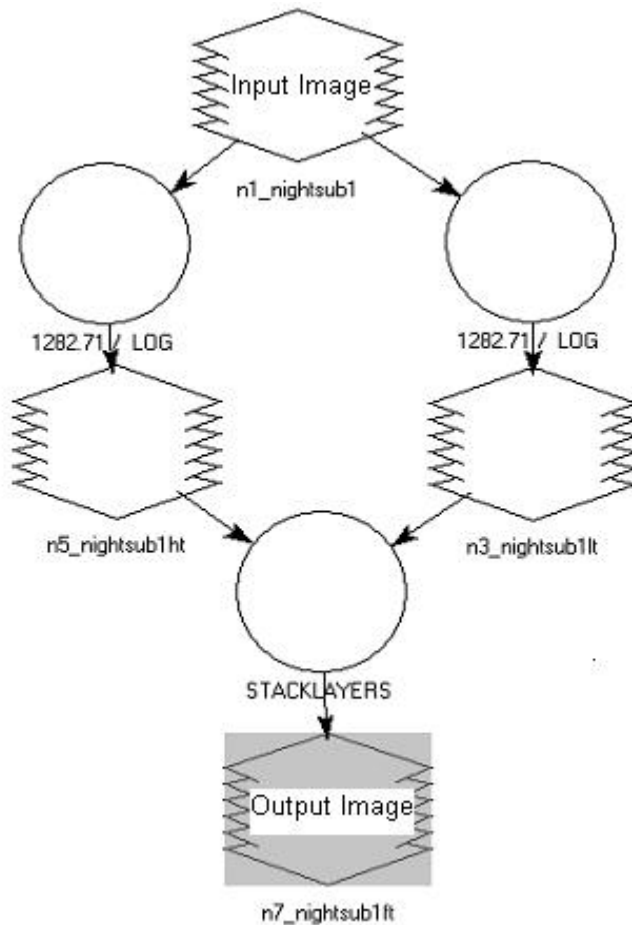


**Figure 4.7** The function of temperature conversion from Landsat7 ETM+ band 6 image.

The temperature converted band6 image, a sub-image (potential coal fire area) and their pixel information are shown below in Figure 4.8 and Figure 4.9, respectively. For a pixel in the potential coal fire area on that sub-image (Row, Column, 200, 54), the following DN values 80, 57 are given in low and high gain image respectively, and the converted temperatures are  $-8.973^{\circ}\text{C}$  and  $-9.327^{\circ}\text{C}$ , respectively. For another pixel (Row, Column, 196, 60), which is located outside of the potential coal fire area, the following DN values are given 75, 48 in low and high gain image respectively. The converted temperatures are  $-12.603^{\circ}\text{C}$ ,  $-12.965^{\circ}\text{C}$ , respectively. The temperature difference between coal fire area and background is about  $3.6^{\circ}\text{C}$ . It indicates that even though the surface temperatures are lower, the thermal anomalies caused by coal fires can be detected.

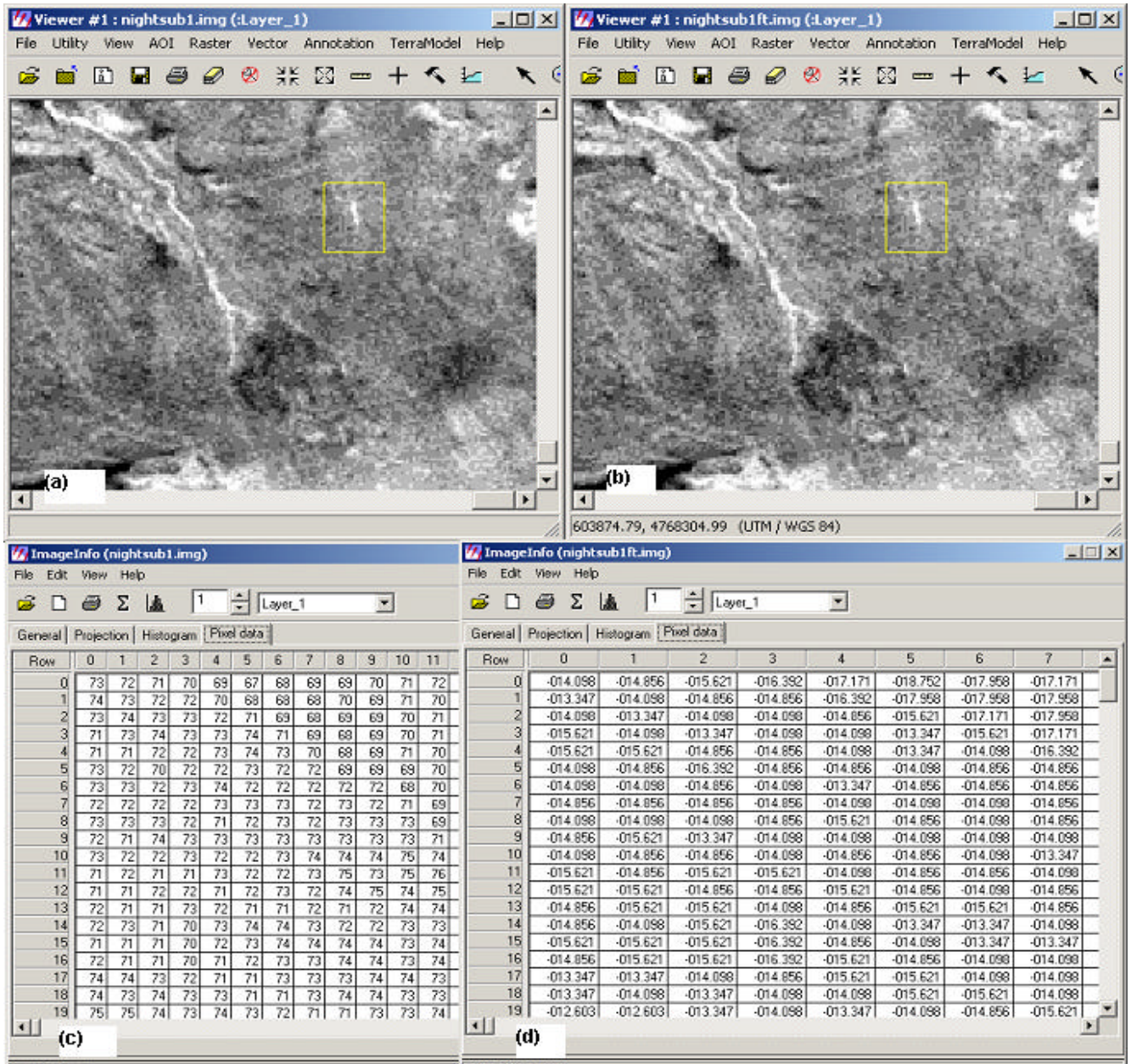


Figure 4.8 The temperature converted image from Landsat7 ETM+ band 6 nighttime low gain image, (a) and (b) are the original image and temperature converted image, (c) and (d) are the relative pixel information of DNs and temperatures, respectively.

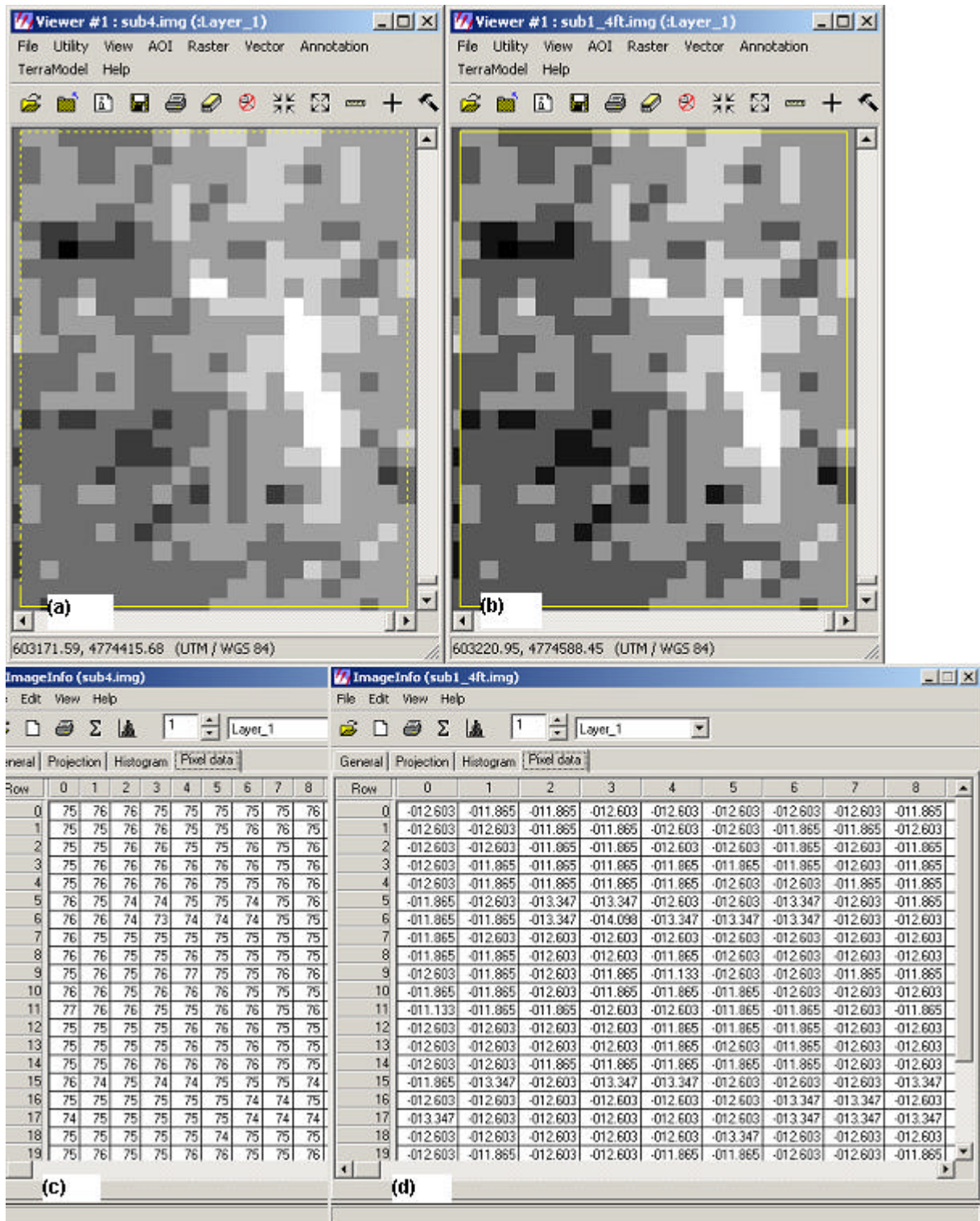


Figure 4.9 The temperature converted sub-image (coal fire area) from Landsat7 ETM+ band 6 nighttime high gain image, (a) and (b) are the original image and temperature converted image (low gain), (c) and (d) are the relative pixel information of DN and temperatures, respectively.

There are five bands for ASTER TIR image, for each band, the temperature conversion can be performed based on the equations mentioned above. The function of temperature conver-

sion from ASTER thermal infrared data is shown in Figure 4.10. The temperature converted image is illustrated in Figure 4.11, the sub-image of a potential coal fire area (within the yellow boundary) also can be converted into temperature image, the relative results are shown in Figure 4.12.

For ASTER TIR band10 to band14 image, the function can be indicated as following,

Band10:  $1735.986 / \text{LOG} ( 3032.999 / ( (\$n1\_sub173b10(1)-1)*6.882 * 10^{\text{POWER} - 3} + 1 )$   
 $* 0.97^{\text{POWER} - 0.25} - 273.16;$

Band11:  $1665.703 / \text{LOG} ( 2466.774 / ( (\$n1\_sub173b10(2)-1)*6.78 * 10^{\text{POWER} - 3} + 1 )$   
 $* 0.97^{\text{POWER} - 0.25} - 273.16;$

Band12:  $1583.288 / \text{LOG} ( 1913.995 / ( (\$n1\_sub173b10(3)-1)*6.59 * 10^{\text{POWER} - 3} + 1 )$   
 $* 0.97^{\text{POWER} - 0.25} - 273.16;$

Band13:  $1358.491 / \text{LOG} ( 890.072 / ( (\$n1\_sub173b10(4)-1)*5.693 * 10^{\text{POWER} - 3} + 1 )$   
 $* 0.97^{\text{POWER} - 0.25} - 273.16;$

Band14:  $1274.336 / \text{LOG} ( 646.490 / ( (\$n1\_sub173b10(5)-1)*5.225 * 10^{\text{POWER} - 3} + 1 )$   
 $* 0.97^{\text{POWER} - 0.25} - 273.16.$

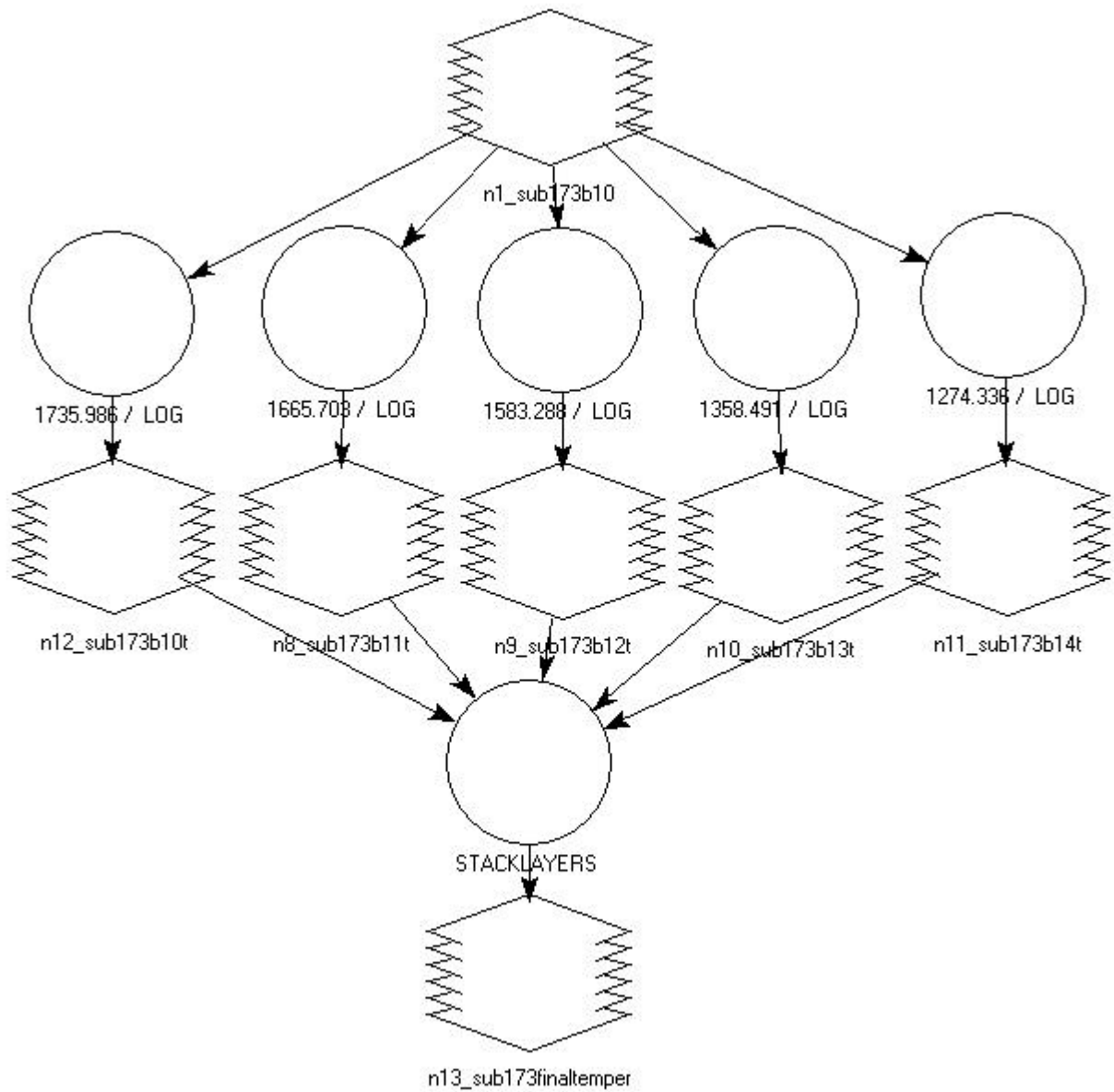


Figure 4.10 The function of temperature conversion from ASTER TIR data.

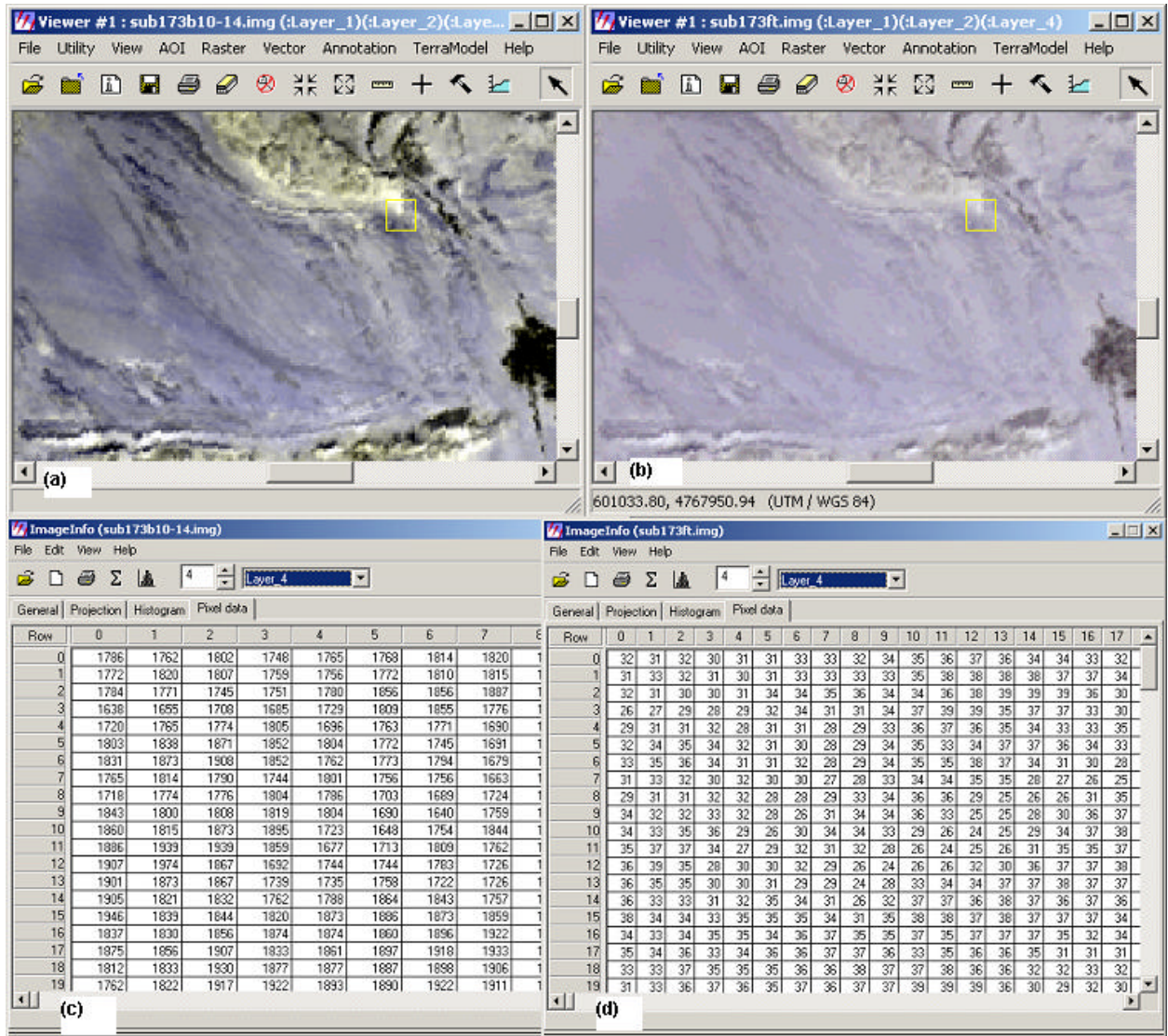


Figure 4.11 A temperature converted ASTER TIR image, (a) the original image, (b) the temperature converted image, (c) and (d) are the relative pixel information of DN values and temperatures for band 13, respectively.

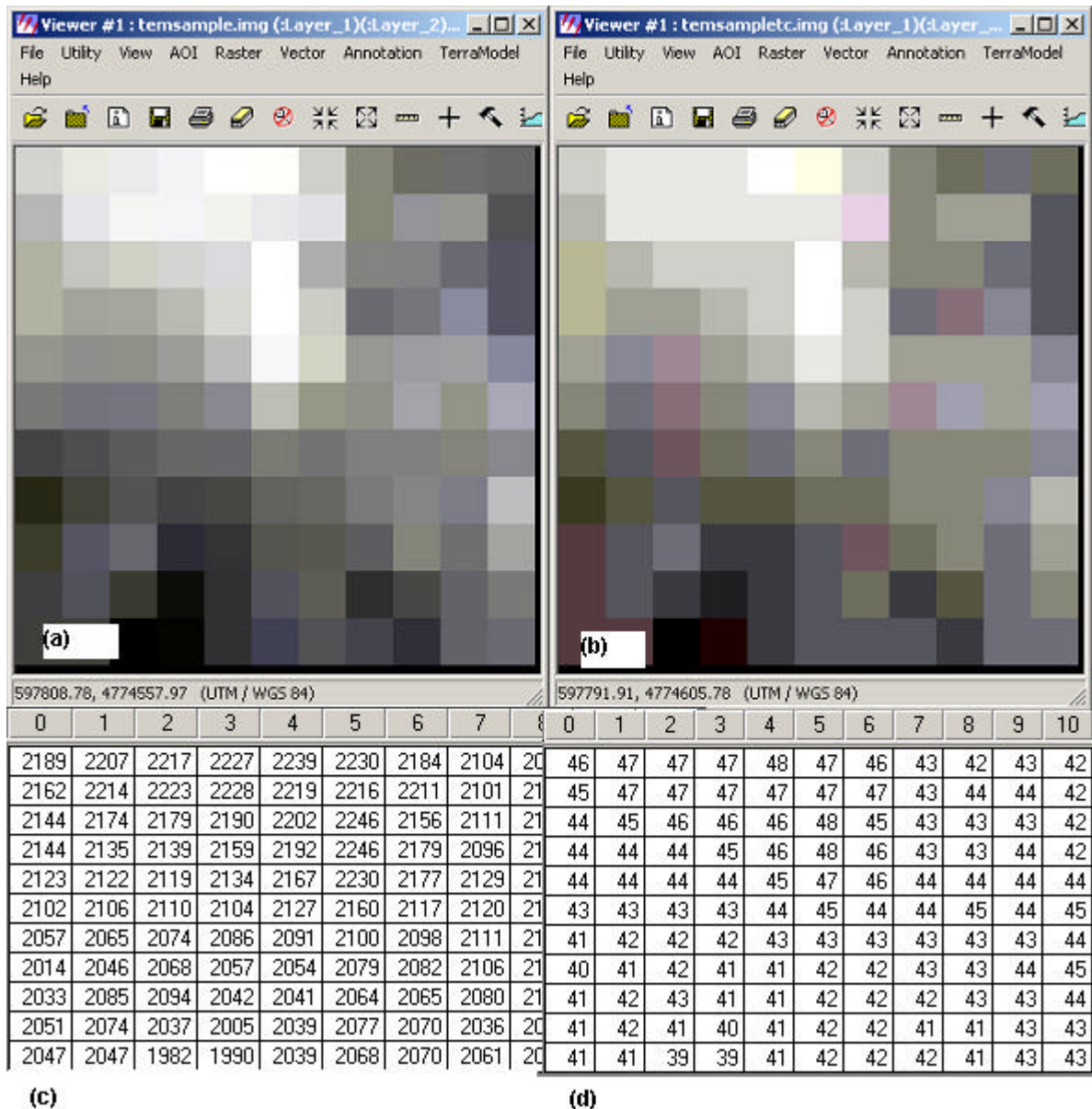


Figure 4.12 A temperature converted sub-image, (a) the original image, (b) the temperature converted image, (c) and (d) are the relative pixel information of DNs and temperatures for band13, respectively (this image was acquired in August, 2001).

From above temperature converted image, for a pixel in the potential coal fire area (Row, Column, 293, 44) and a pixel outside that area (Row, Column, 293, 49), the following DN values are given 1765, 1736 in band13 respectively. The temperatures derived are “31.325°C, 30.219°C” for the band13 respectively. It indicates the temperature difference between coal fire area and background is about 1°C. The temperatures from ASTER data and Landsat7 ETM+ band6 nighttime image are very different due to the different data acquisition time. The first data set was acquired in August 2001, the latter was acquired in February 2000. On both thermal anomalies can be detected. Although absolute temperatures derived are different, still the thermal anomalies exist and can be used for subsequent analysis.

## 4.5 Quantitative methods of detecting coal fire areas

Some potential coal fire areas were selected as described in Chapter 4.3. If coal fire is presents there, are thermal anomalies caused by fire detectable. How much is the thermal anomaly caused by coal fire? How to decide the size of the coal fire area? The thermal anomalies on the remote sensing data are derived by setting a threshold. There are three ways to select the threshold: (1) trial and error (Saraf et al., 1995; Prakash et al., 1995); (2) exclusion method; and (3) statistical method (Zhang et al., 1997). In the first method, field measurement results are used. The second method selects a threshold to check the coal fire areas, which exclude all pixels outside the coal seam areas. It should take care that some pixels of thermal anomalies caused by coal fires located in the area nearby the coal seam area would be neglected, because sometime thermal anomalies caused by subsurface or underground coal fires locate along the coal seams and may be outside the area you selected. Hence, this method should be carefully carried out with the help of the detection on nighttime image. In this study, the statistical method provides the threshold based on the statistical data and sub-image analysis.

### 4.5.1 Statistical method

#### (1) General statistical analysis

In this study, the research area is selected as the source data of general statistical analysis instead of the whole image, because in that case there is too much noise to identify the change and trend of thermal anomalies caused by coal fires. For instance, there are sloping areas where the DN values are larger than the potential coal fire areas because the slope is directly irradiated by the sun, These thermal anomalies due to difference in solar heating affect the detection of coal fire areas. It should be noted that the result of detection of coal fire areas would be correlative to the size of analyzing area, if the size was larger, the environmental noise will affect the analyzing result. The nighttime thermal image would be much better because it can effectively reduce the affect of solar heating.

The Figure 4.13 shows that part of Landsat7 ETM+ band 6 low gain image (nighttime) overlaid on the Landsat7 visual image, the part within yellow boundary is the test area of the whole band 6 nighttime image, and the areas circled by red polygons are potentially selected coal fire areas. From the histogram and statistical information of this sub-image, it is known that, for high gain image,  $DN_{\min} = 32$ ,  $DN_{\max} = 63$ ,  $DN_{\text{mean}} = 49$ , the Std.Dev.= 3, the statistical results are indicated as histograms in Figure 4.14.

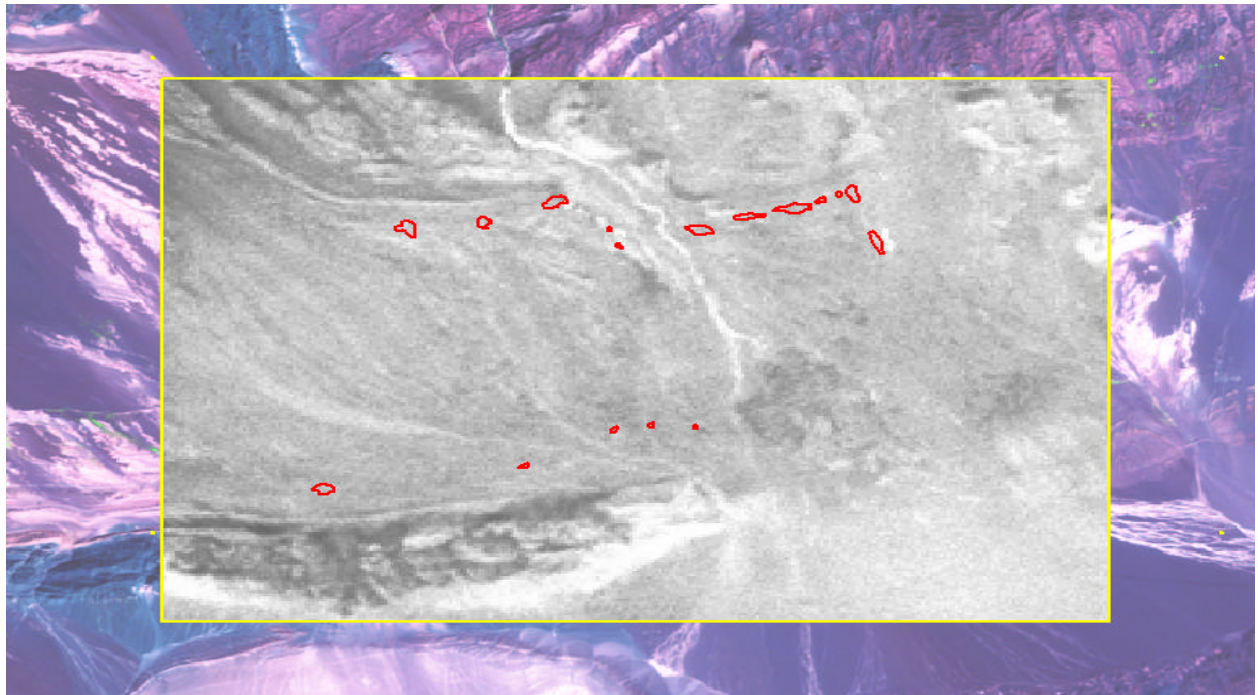


Figure 4.13 The sub-image of Landsat7 ETM+ band 6 low gain image acquired in nighttime.

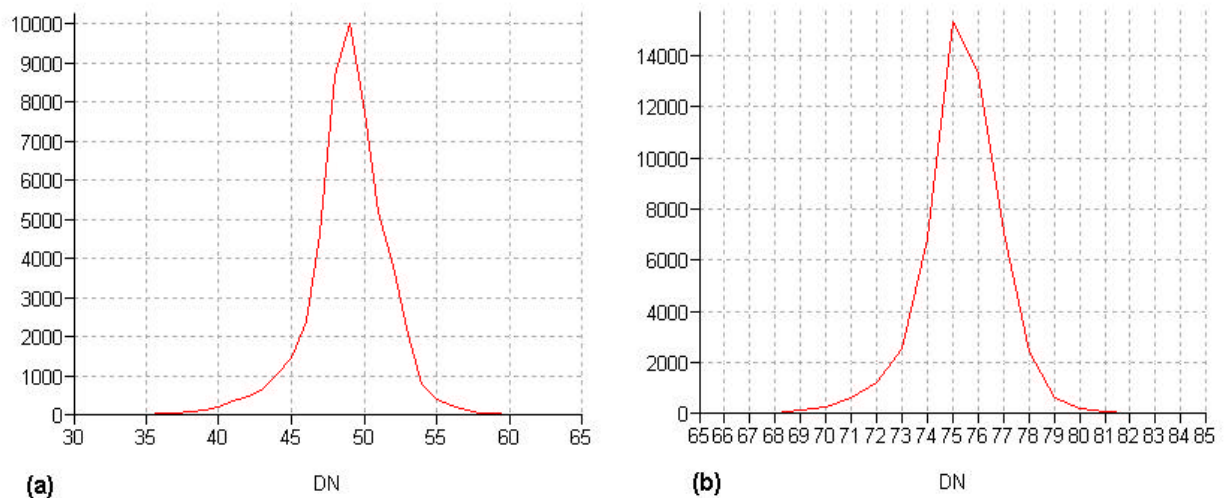


Figure 4.14 The histogram of above band6 sub-image, (a) is the results for high gain image, (b) is for low gain image.

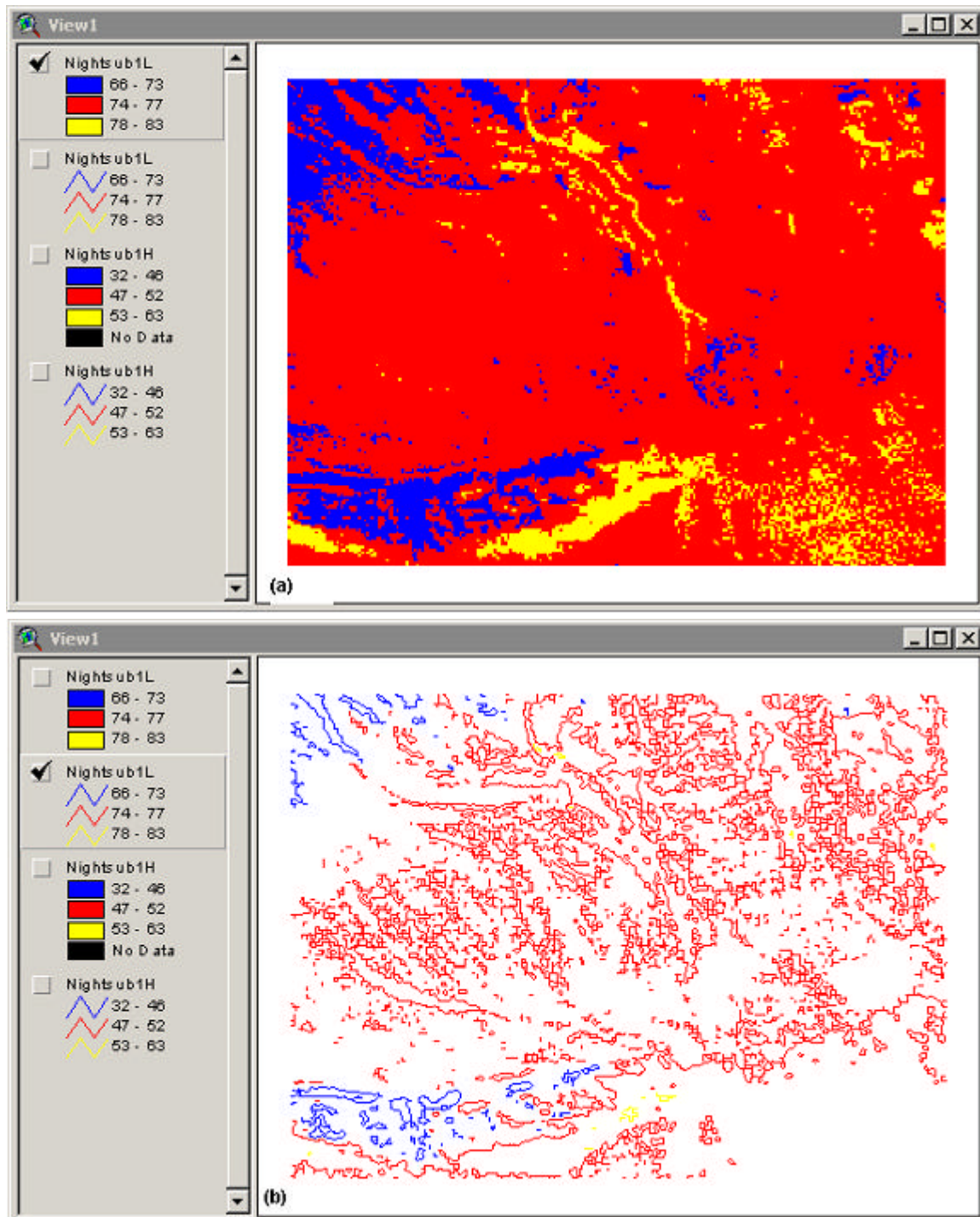
More information can be obtained to perform statistical analysis using ArcView GIS system. The results of analyzing DNs from above data are classified into 3 classes according to the standard deviation (D) as following:

$$\text{Class1: } DN_{\min} < DN_i = (DN_{\text{mean}} - D),$$

$$\text{Class2: } (DN_{\text{mean}} - D)+1 < DN_i = (DN_{\text{mean}} + D),$$

$$\text{Class3: } (DN_{\text{mean}} + D)+1 < DN_i = DN_{\max}.$$

It shows that the classification is too general to identify the coal fire areas, and it implies that the thermal anomalies caused by coal fires are relatively small, which are difficult to separate with a background covering such a large area. The classified results of DN<sub>s</sub> also can be expressed using a contour of DN<sub>s</sub>, from which the change trend of temperatures within the study area is shown clearly. This classification is affected by some noise caused by solar heating; therefore, the general analysis is meaningless for the detection of coal fire areas. The statistical analysis from DN<sub>s</sub> of TIR data would be better performed using a smaller area. Figure 4.15 shows the general statistical analysis from Landsat7 ETM+ TIR data (nighttime).



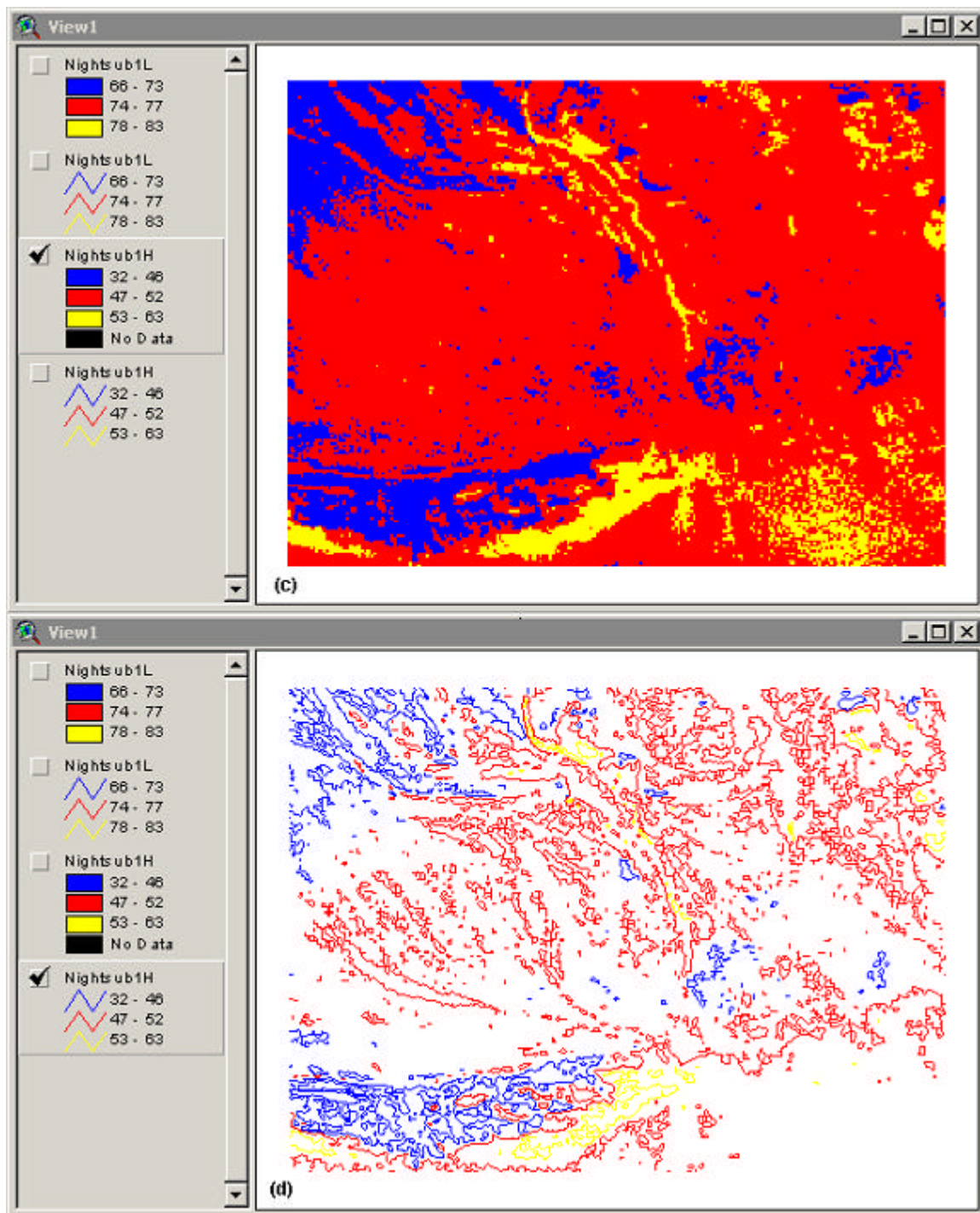


Figure 4.15 The general statistical analysis from DNs of Landsat7 ETM+ TIR data (nighttime), (a) and (c) are the results from low and high gain, (b) and (d) are the related DN contours, respectively.

For ASTER TIR data, band 10, for example, in the whole study area,  $DN_{\min} = 1148$ ,  $DN_{\max} = 1787$ ,  $DN_{\text{mean}} = 1533$ ,  $\text{Std.Dev.} = 70$ . For other TIR band data, the above statistical results are different, for instance, band 14,  $DN_{\min} = 1687$ ,  $DN_{\max} = 2416$ ,  $DN_{\text{mean}} = 2169$ ,  $\text{Std.Dev.} = 88$ . Figure 4.16 shows those results in histogram. The case is as the same as in Landsat7 data, it is

difficult to determine the threshold for the detection of coal fire areas. The result of similar analysis using ArcView GIS system is shown in Figure 4.17.

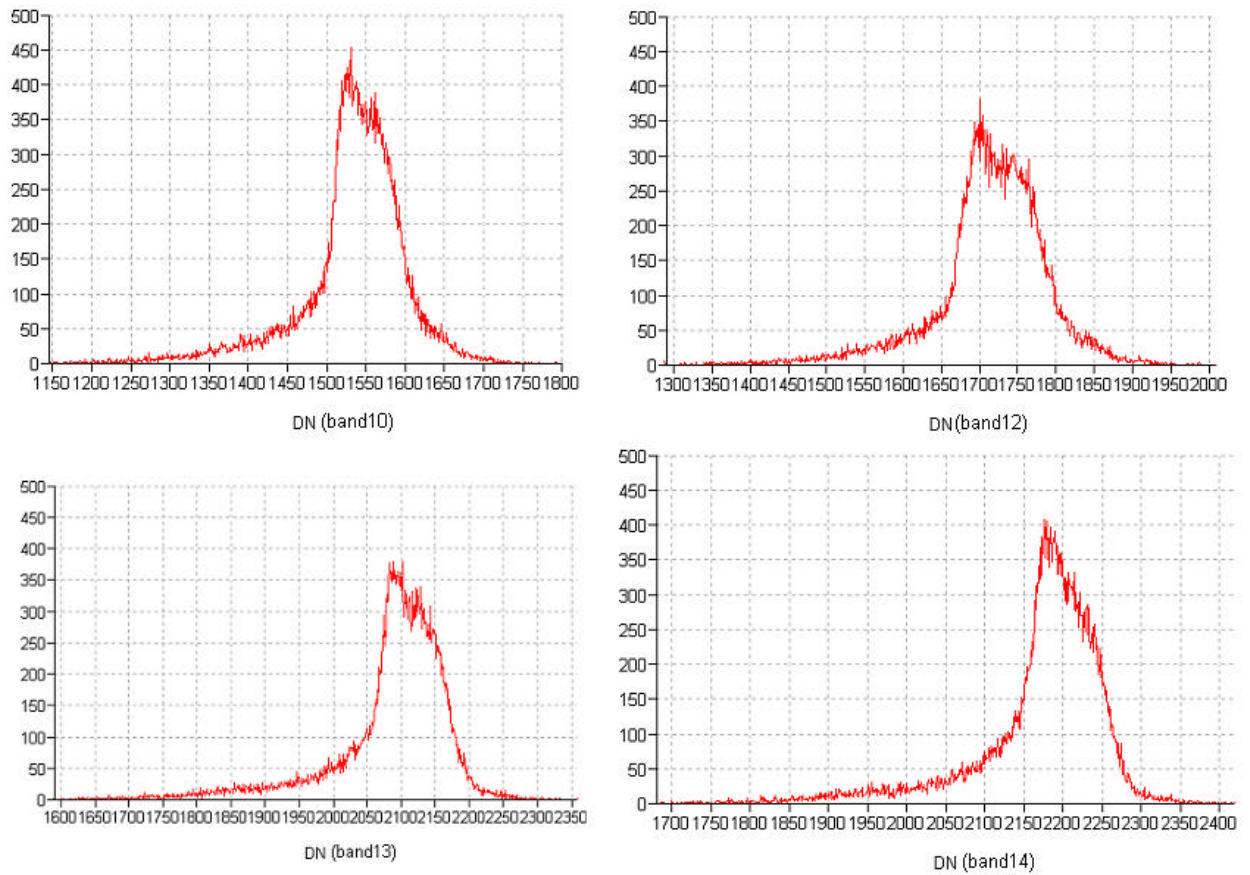


Figure 4.16 The histograms for study area from ASTER TIR data, band 10, 12, 13, 14.

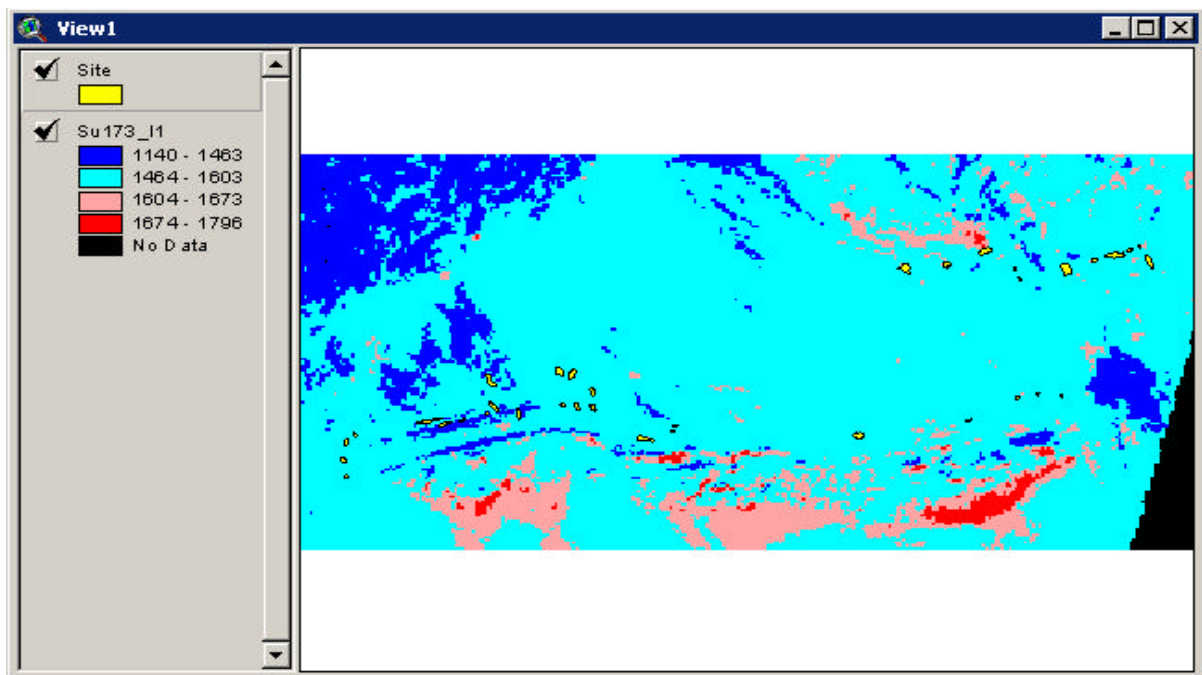


Figure 4.17 The general statistical analysis from DN's of ASTER TIR data (band 10).

Because there is much noise on the imagery of the study area for the detection of coal fire areas, in this study, the statistical analysis is considered to be performed based on smaller sub-images, (10\*10 pixels on ASTER TIR images). Before the analysis using ArcView system, the image files have to be transformed into GRID files, to be used in ArcView.

However, the above general analysis indicates that, in some potential coal fire areas, the DN's of thermal anomalies are more like the DN mean value of the whole study area. For example, within a small area near the water-body, the thermal anomalies caused by subsurface coal fires may be smaller than those caused by the emittance of the water-body. Therefore, the general statistical analysis over a large area has little meaning for the detection of coal fires.

## (2) Sub-image statistical analysis

The statistical analysis is performed based on the sub-image, identified of each potential coal fire area. For example for the analysis of ASTER TIR data, sub-images are created for each selected site based on a sub-window of 10\*10 pixels from TIR imagery. In that case, for each sub-image, there are at least 100 DN values provided for the analysis (for the same sub-window, there are at least 225 DN values on Landsat7 band 6 image). In the statistical analysis, the DN's within each sub-image will be classified into 3 classes based on the values of DN's mean and standard deviation (D), as described above. From the results of classification, we select the area located in Class3 (the yellow area) as the fire area, because thermal anomalies are considered presenting in the "hottest" area. It should be noted that the analysis using different bands of ASTER TIR data are different, except band11 (DN's on band10 and 11 are same), however, the trend and potential area can be defined based on them, this has been illustrated in Figure 4.6, the relation curves of DN's and surface temperatures from ASTER TIR data.

Given time limitations it was not possible to complete a full statistical analysis of all the potential sites identified. A few sites have been selected to demonstrate the analysis procedures, focusing also on the comparative analysis between ASTER and Landsat7 ETM+ thermal infrared data.

Figure 4.18 shows an example of statistical analysis results for site 6 from ASTER TIR band10, band12, band13 and band14, and the relative histograms are shown in figure 4.19. In the same way, a statistical analysis of the same site of sub-image from Landsat7 ETM+ band6 nighttime data was performed, and the results are shown in Figure 4.20, the related histograms are illustrated in Figure 4.21.

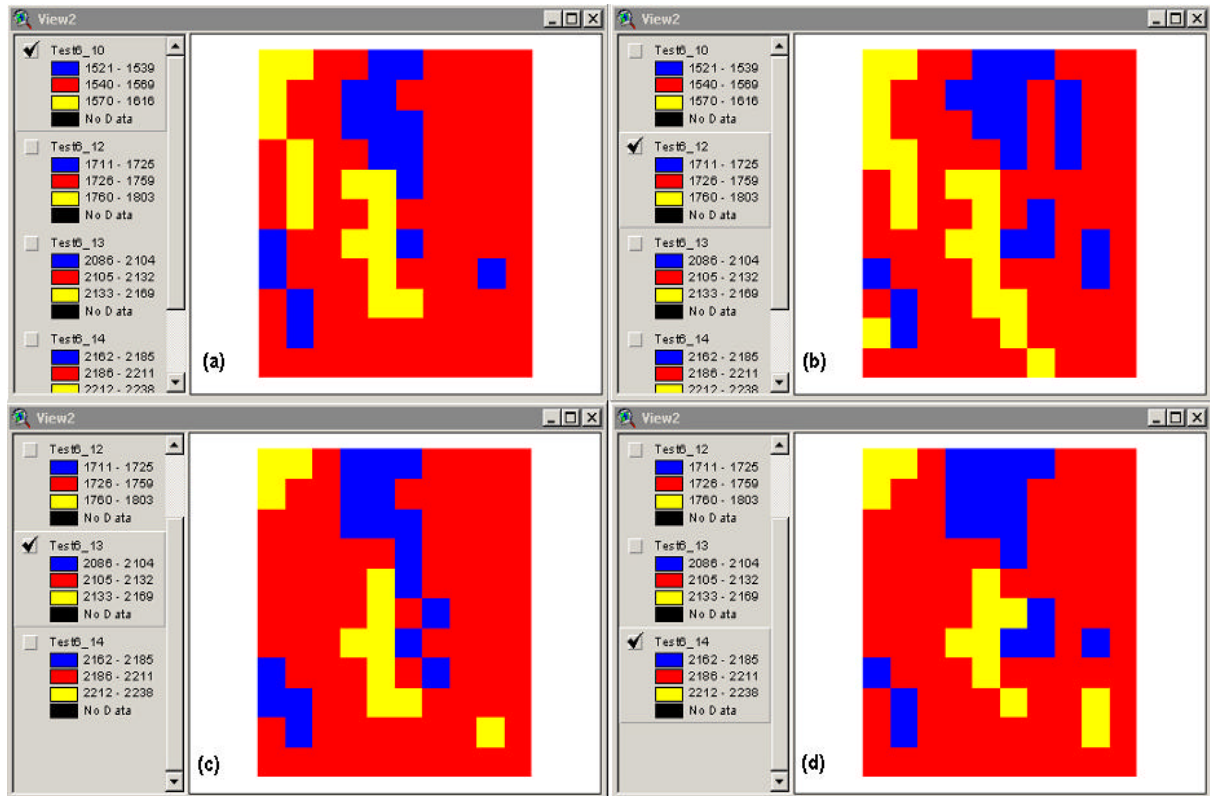


Figure 4.18 The results of classification of site 6 from ASTER TIR band10, band12, band13, and band14, from (a)- (d), respectively.

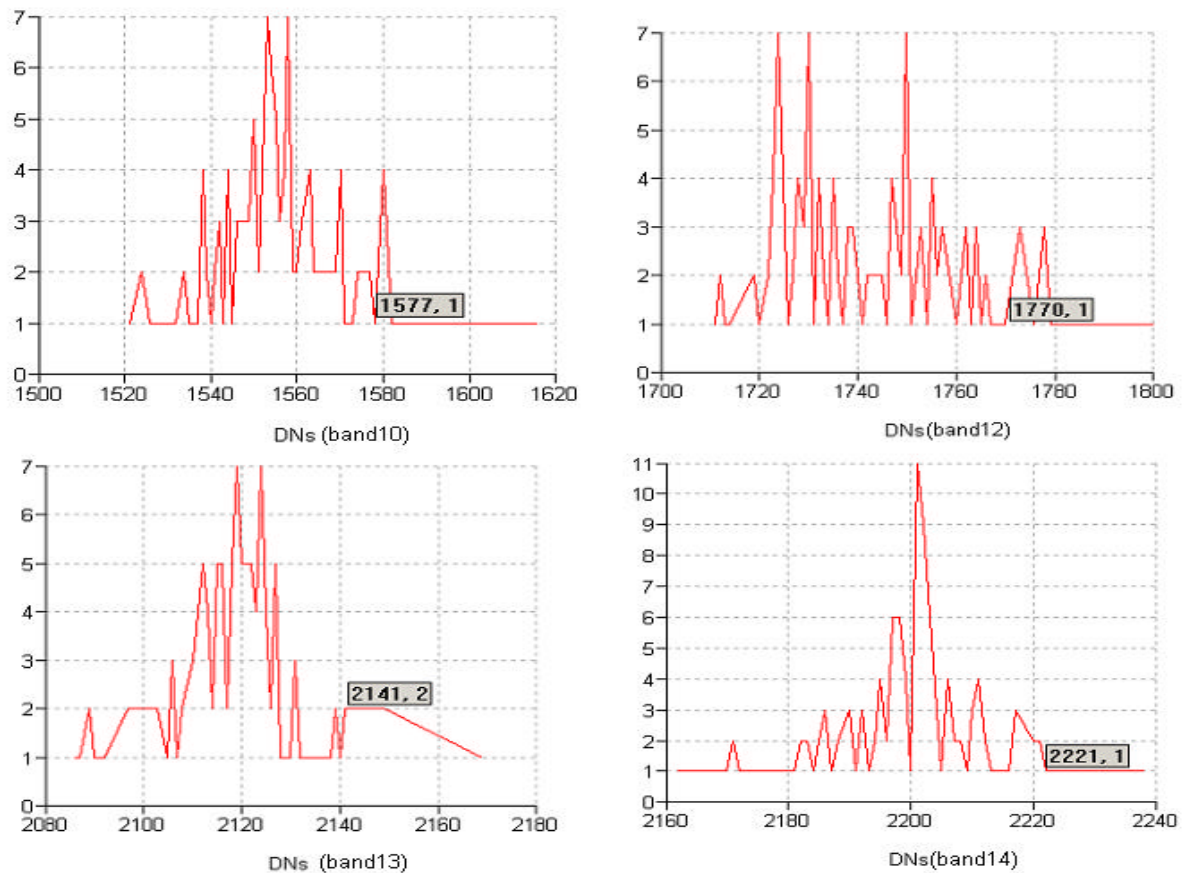


Figure 4.19 Histograms of site 6 from ASTER TIR band10, 12, 13, 14.

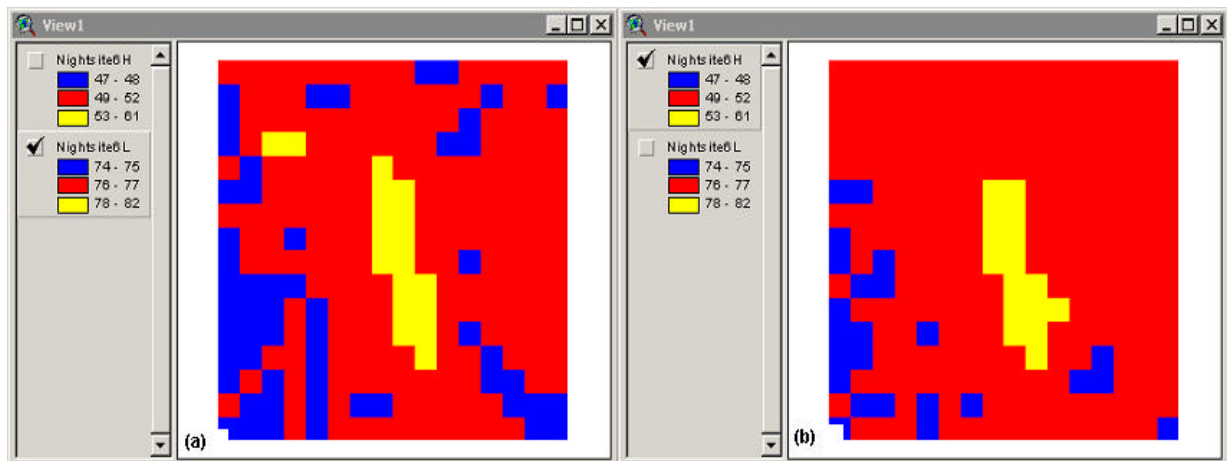


Figure 4.20 The results of classification of site 6 from Landsat7 ETM+ band 6 nighttime data, (a) low gain, (b) high gain.

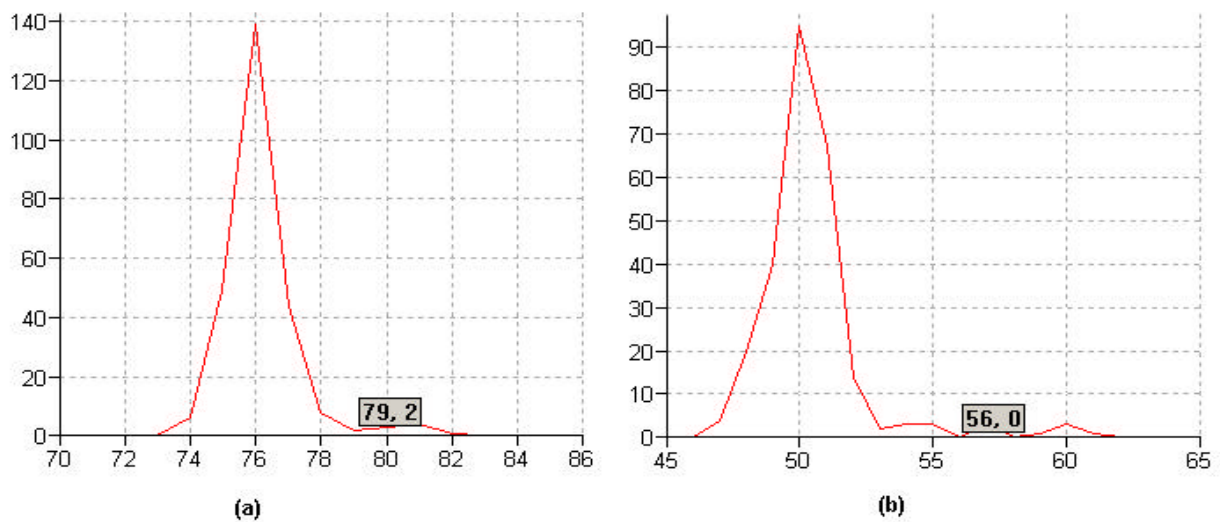
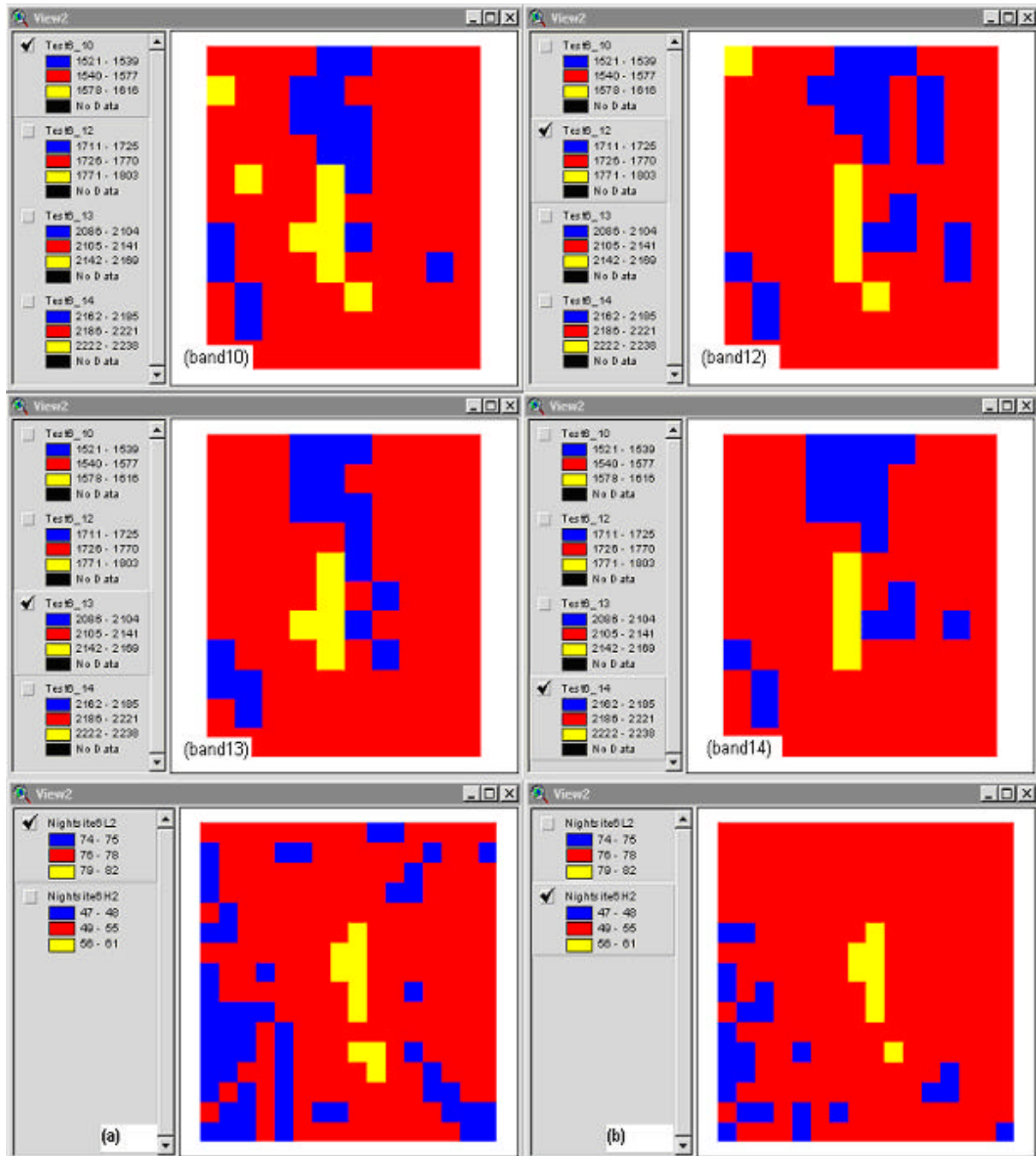


Figure 4.21 Histograms for site6 of Landsat7 ETM+ band6 data, (a) is for low gain, (b) is for high gain.

From the above results, it expresses that there are little difference in the results between ASTER and Landsat7 TIR data. After the analysis of those histogram shapes, some thresholds of coal fire are selected, whose values are illustrated in histograms (gray clor). Therefore, the final coal fire area for site6 is defined according to those thresholds and shown in Figure 4.22.



**Figure 4.22** The analysis results from ASTER TIR band13 and Landsat7 ETM+ band6 data after the correct based on the histograms.

The above comparison of statistical analyzing results shown on the image, for example the results from ASTER band13 and Landsat7 ETM+ band6 low gain data, is illustrated overlaying on an ASTER visual image in Figure 4.23. It should be noted that, (1) the results from ASTER and Landsat7 TIR data basically are accordant; (2) ASTER TIR band 10 is more affected by atmospheric absorption and emission than the other ASTER bands because it is located closest to the edge of the TIR atmospheric window (Gillespie, et al., 1998). (3) Some difference in the results from two kinds of TIR data still exist because a few factors affect the detection ability, such as the acquisition time of those two data sets (ASTER was acquired at

12:21 at daytime, on 19<sup>th</sup> of August, 2001; Landsat7 ETM+ was acquired at nighttime, on 1<sup>st</sup> of February, 2000), and the levels of DNs saturation for those two kinds of sensors are different.

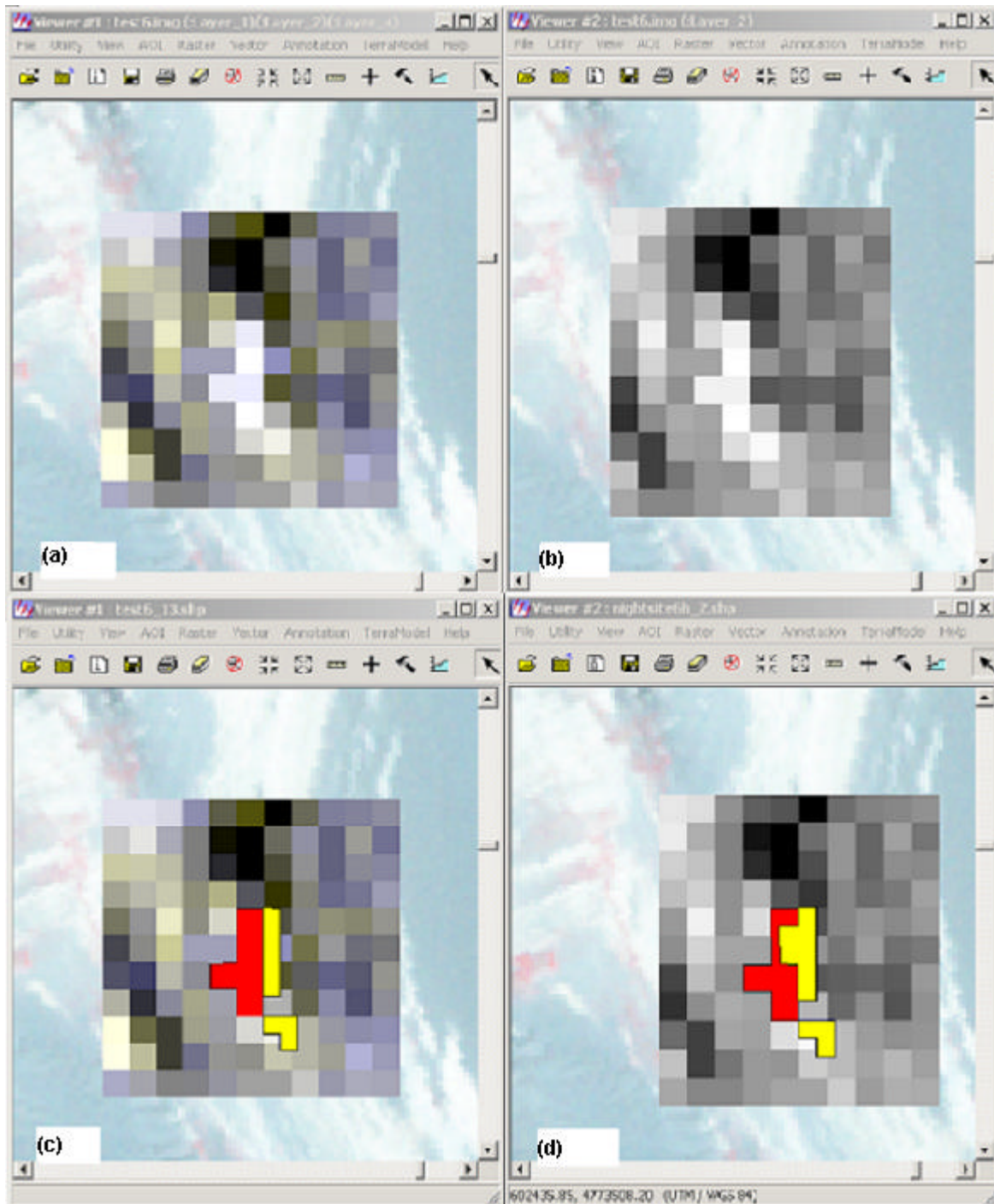


Figure 4.23 The final analysis results for site6 from ASTER TIR band13 (the red area) and Landsat7 ETM+ band6 low gain data (the yellow area) overlaying on an ASTER visual image, (a) ASTER TIR sub-image, (b) Landsat7 band6 nighttime sub-image, (c) result from ASTER band13, (d) result from Landsat7 low gain data.

The ground temperatures of the above final detection results can be calculated based on the equations mentioned in Chapter 4.4. The calculation results are listed in Table 4.7, the tem-

perature of coal fire area from Landsat7 band6 nighttime data is at  $-7.5$  to  $-9.7^{\circ}\text{C}$ , and from ASTER TIR data the temperature at about  $42^{\circ}\text{C}$ . From the surface temperature results, it indicates that the temperatures detected in site6 from those two kinds of sensed data are very different because the data acquisition time is different, Landsat7 ETM+ band6 nighttime data was acquired on 1st Feb 2000, and the ASTER data was acquired in August, 2001.

**Table 4.7 Final temperature calculation of the site 6 from Landsat7 ETM+ band6 and ASTER TIR data**

	A	B	C	D	E	F	G	H	I	J
1		DN	$L_{\lambda 1}$	$L_{\lambda h}$	$T_{R1}$	$T_{K1}$	$T_{K1}'$	$T_{Rh}$	TKh	$T_{Kh}'$
2	Landsat7	56		4.96536	#DIV/0!	#DIV/0!	#DIV/0!	261.438	263.436	9.724
3		61		5.15066	#DIV/0!	#DIV/0!	#DIV/0!	263.390	265.403	7.757
4		79	4.96878		261.474	263.473	9.687	#DIV/0!	#DIV/0!	#DIV/0!
5		82	5.16924		263.583	265.598	7.562	#DIV/0!	#DIV/0!	#DIV/0!
6	ASTER	DN	$L_{\lambda 10}$	$L_{\lambda 10}$	$\lambda 10$	$K_1$	$K_2$	$T_{R10}$	$T_{K10}$	$T_{k10}'$
7	band10	1600	6.882E-03	11.004	8.295E-06	3032.999	1735.986	308.749	311.109	37.949
8		1616	6.882E-03	11.114	8.295E-06	3032.999	1735.986	309.295	311.659	38.499
9	band12	1771	6.590E-03	11.664	9.095E-06	1913.995	1583.288	310.054	312.424	39.264
10		1803	6.590E-03	11.875	9.095E-06	1913.995	1583.288	311.139	313.517	40.357
11	band13	2142	5.69E-03	12.189	1.060E-05	890.072	1358.491	315.606	318.018	44.858
12		2169	5.69E-03	12.342	1.060E-05	890.072	1358.491	316.515	318.934	45.774
13	band14	2222	5.23E-03	11.605	1.130E-05	646.490	1274.336	315.591	318.003	44.843
14		2238	5.23E-03	11.688	1.130E-05	646.490	1274.336	316.143	318.560	45.400
15									Mean:	42.118

#### 4.5.2 Combination method of statistics and probability analysis

Another method is used for the detection based on the statistics and assessment of probability. First, it is assumed that those pixels most probably located in the coal fire area have DNs that are closest to the maximum DNs of each sub-image. This is can be defined by the following conditions:

$$P_i = (DN_i - DN_{\min}) / (DN_{\max} - DN_{\min}) \tag{4.16}$$

where,  $P_i$  is the probability of pixel locating in the coal fire area,  $DN_i = DN$  of each pixel on sub-image of each site,  $i =$  the number of site,  $DN_{\min} =$  the minimum DN on sub-image,  $DN_{\max} =$  the maximum DN on sub-image. Providing  $P_i=0.70, 0.80, 0.85,$  and  $0.90,$  the analysis results in different level of probability can be obtained. Figure 4.24 shows the analysis results in different level of probability from Landsat7 ETM+ band6 low and high gain nighttime data, and Figure 4.25 shows the results from ASTER band12 and band13. The relative probability calculation is shown in Table 4.8.

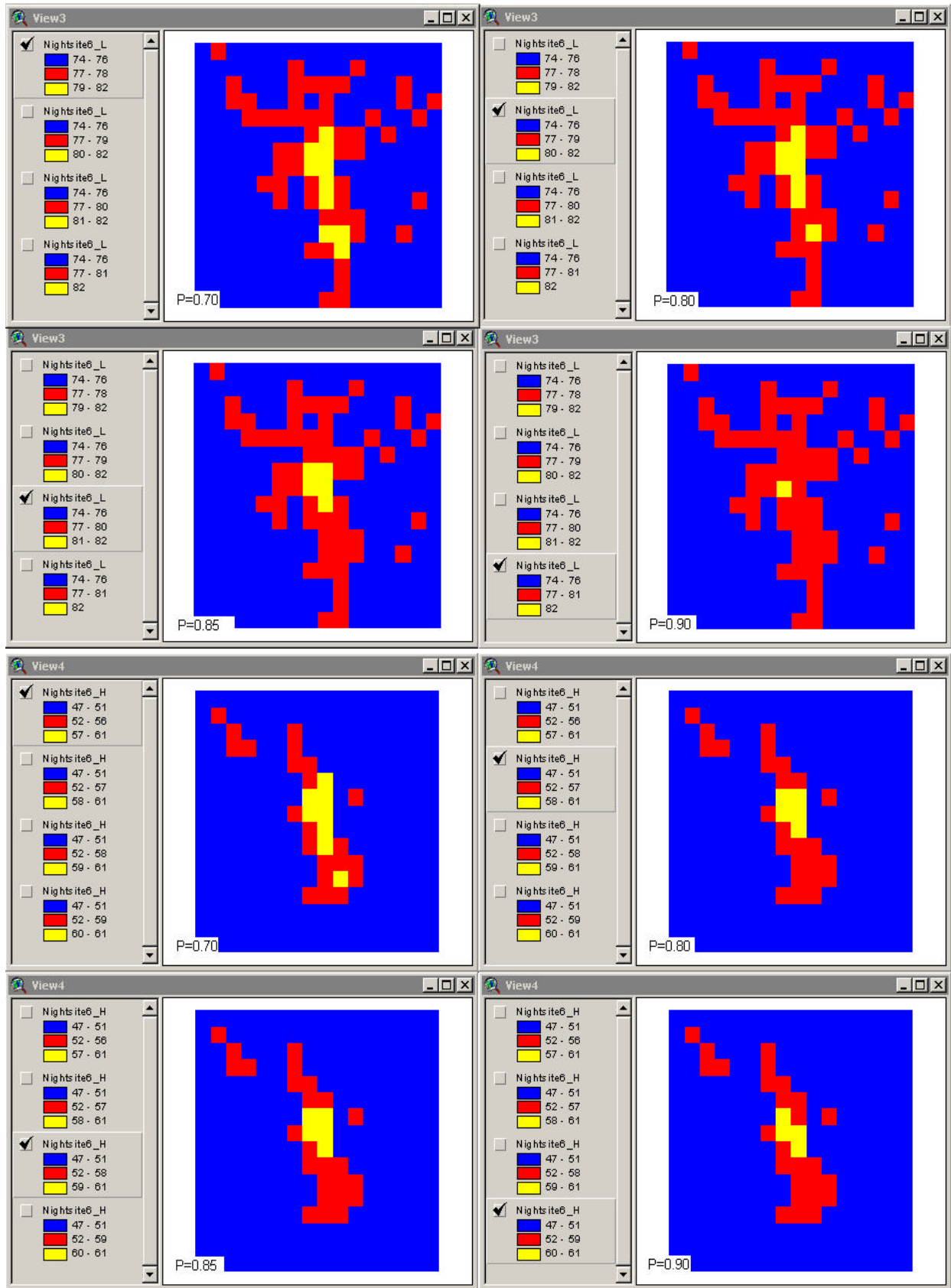


Figure 4.24 The analysis results in different level of probability from Landsat7 ETM+ band6 nighttime low and high gain data.

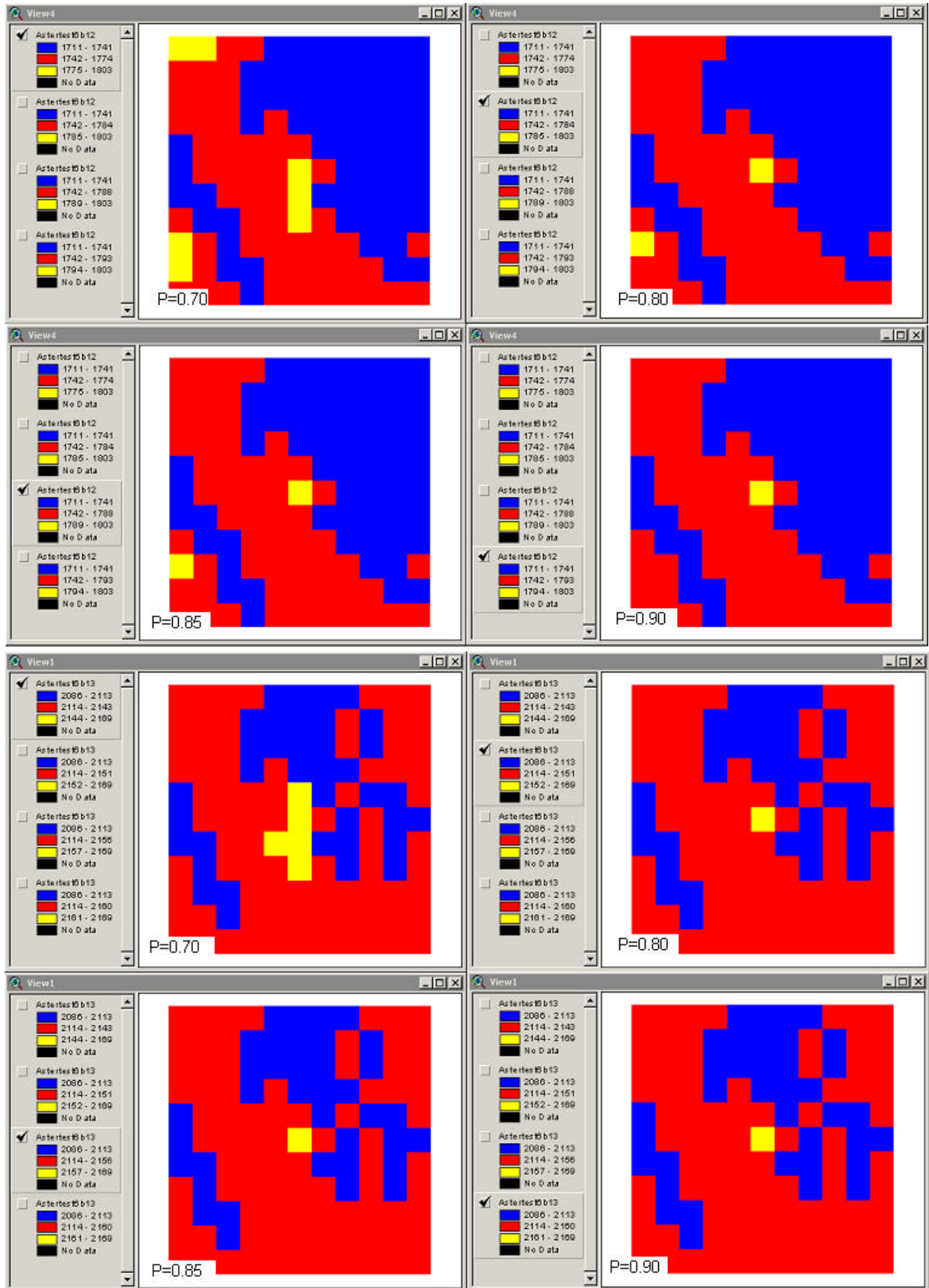


Figure 4.25 The analysis results in different level of probability from ASTER band12 and band13 data.

**Table 4.8 The results of probability calculation for site6 from Landsat7 ETM+ band6 nighttime data ASTER TIR data**

	A	B	C	D	E	F	G	H	I	J
1	Sensor	Site	DN <sub>i</sub>	DN <sub>min</sub>	DN <sub>max</sub>	Pi				
2	Landsat7	nightsite6L	79	74	82	0.63				
3			80	74	82	0.75				
4			81	74	82	0.88				
5			82	74	82	1.00				
6		nightsite6H	57	47	61	0.71		$P_i = (DN_i - DN_{min}) / (DN_{max} - DN_{min})$		
7			58	47	61	0.79				
8			59	47	61	0.86				
9			60	47	61	0.93				
10	ASTER	test6b10	1588	1521	1616	0.71				
11			1597	1521	1616	0.80				
12			1602	1521	1616	0.85				
13			1607	1521	1616	0.91				
14		test6b12	1775	1711	1803	0.70				
15			1785	1711	1803	0.80				
16			1789	1711	1803	0.85				
17			1794	1711	1803	0.90				
18		test6b13	2144	2086	2169	0.70				
19			2152	2086	2169	0.80				
20			2157	2086	2169	0.86				
21			2161	2086	2169	0.90				
22		test6b14	2215	2162	2238	0.70				
23			2223	2162	2238	0.80				
24			2227	2162	2238	0.86				
25			2231	2162	2238	0.91				

This indicates that the results with a probability of 0.70 from Landsat7 ETM+ band6 nighttime data and ASTER TIR data are similar to each other, when  $P_i = 0.80$ , the detection results from the two kinds of sensed data are almost the same.

### 4.6 Classification

The objective of image classification is to classify and categorize pixels in an image into different kinds of land cover classes or themes based on interests. Normally, multispectral data are used to perform the classification, and the spectral pattern present within the imagery for each pixel is used as the numerical basis for categorization. The term pattern refers to the set of radiant measurements obtained in various wavelength bands for each pixel instead of geometric in character. In this case, the general statistical analysis from DNs is a way of classification.

Classification is the process of sorting pixels into a finite number of individual classes, or categories of data, based on their data file values. If a pixel satisfies a certain set of criteria, then the pixel is assigned to the class that corresponds to those criteria. There are two ways to classify pixels into different categories: supervised and unsupervised classification. They are discussed below.

#### **4.6.1 Supervised classification**

In this type of classification the image analyst “supervises” the pixel categorization process by specifying, to the computer algorithm, numerical descriptors of the various land cover types present on an image. The sample sites of known cover type, called training areas, are used to compile a numerical “interpretation key” that describes the spectral attributes for each feature type of interest. For the first part of the classification process, the computer system must be trained to recognize patterns in the data. Training is the process of defining the criteria by which these patterns are recognized. The result of training is a set of signatures, which are criteria for a set of proposed classes.

First, in this study, some sample sites are selected from Landsat7 visual sub-image according to the interpretation and analysis of geology, geomorphology and topography. Then, with the help of the function of supervised classification, the image is classified the different land cover types, including coal mining areas (potential coal fire areas). Figure 4.26 shows the results of supervised classification from the Landsat7 ETM+ band 5, 4, 3(RGB). It indicates that the results are not good and helpful for the detection of coal fire areas, only are the main land covers roughly classified, such as the mountain area (blue area, the city is also shown in blue, which is shown in red on the visual image), alluvial fan (red area), and sediment area (green area). Hence, the supervised classification is worthless for the detection of potential coal fire areas.

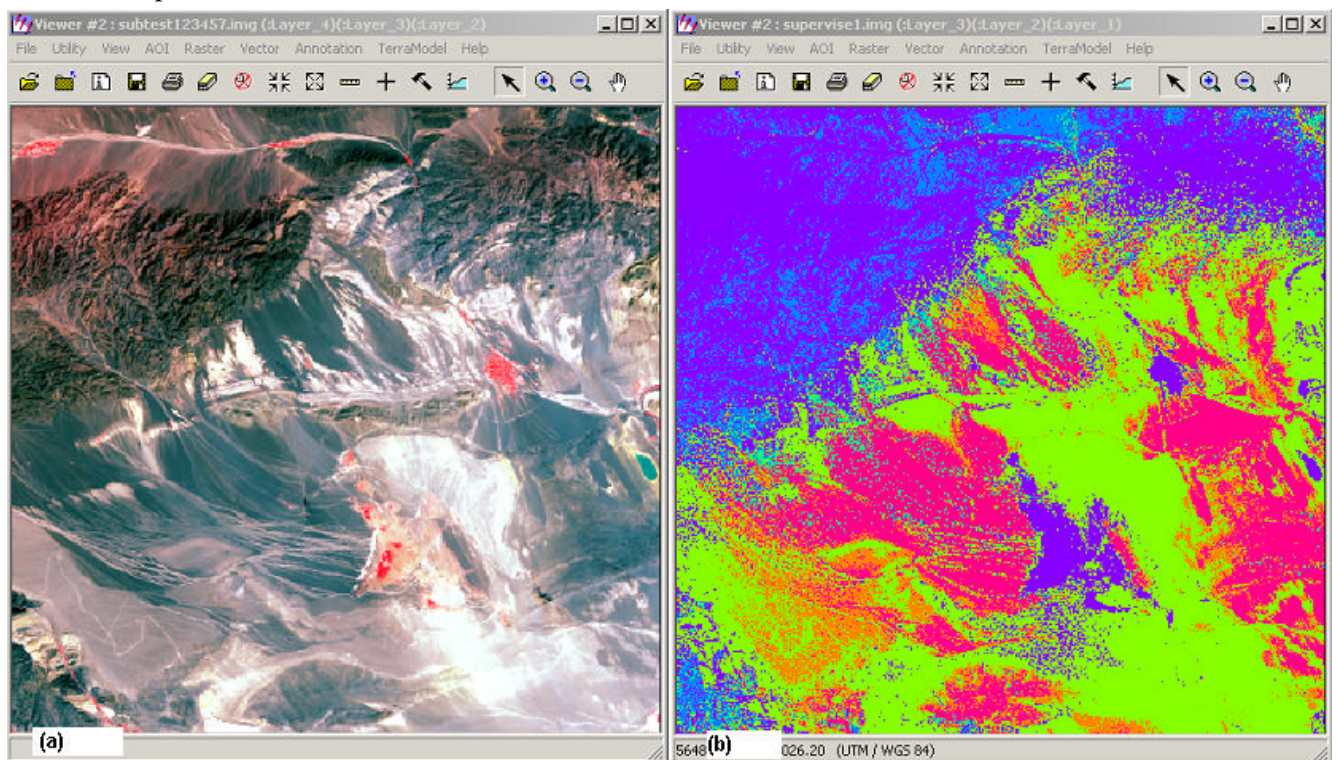


**Figure 4.26** The result of supervised classification from Landsat7 ETM+ band 5,4,3 (RGB), (a) is the visual image, (b) is the classification result.

#### 4.6.2 Unsupervised classification

In the unsupervised classification the image data are first classified by aggregating them into the natural spectral groupings, or clusters, present in the scene. The basic premise is that values within a given cover type should be close together in the measurement space, whereas data in different classes should be comparatively well separated. The classes that result from unsupervised classification are spectral classes. In the supervised approach we define useful information categories and then examine their spectral separability; in the unsupervised approach we determine spectrally separable classes and then define their informational utility.

The following example of the unsupervised classification for the same sub-image of Landsat7 ETM+ is shown in Figure 4.27. It is performed by means of the function provided in ERDAS, the parameter iteration and the number of classes are selected as 6 and 12, respectively.

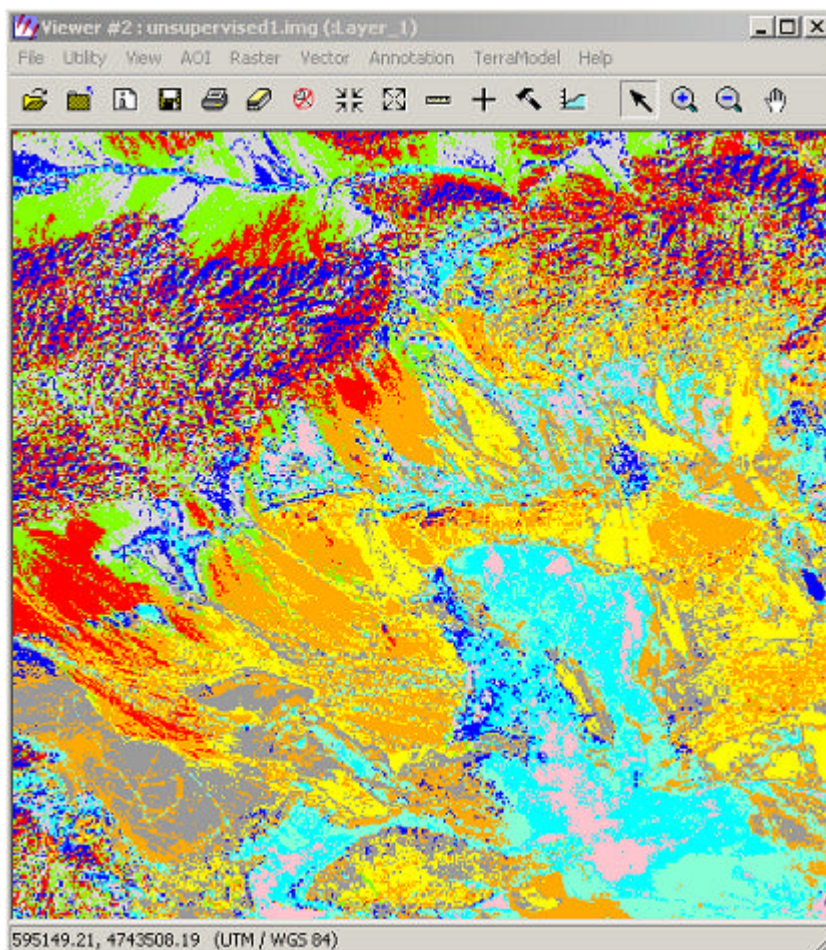


Figure 4.27 The result of unsupervised classification from Landsat7 ETM+ band 5,4,3 (RGB).

The results of both classification procedures show that the results are of no use for the detection of potential coal fire areas, whereas it is helpful for the classification of land cover types.

In this study, the ground emissivity is assumed as 0.97. From the above classification results, we can identify the different land covers, further, the different emissivities of ground materials can be obtained using the temperature and emissivity separation (TES) algorithm mentioned in Chapter 2. Therefore, the results of surface temperature calculation will be more accurate using the appropriate emissivity for each of the cover types differentiated during the supervised or non-supervised classification. Validation of the results is not possible at this stage because author does not have sufficient ground reference (ground samples).

# Chapter 5 The accuracy assessment for the detection of coal fires

## 5.1 Factors affected the detection results of coal fires

There are some errors in the detection of coal fires due to the sensor, image processing techniques applied, environmental noise and the difference of thermal anomalies between in the coal seam area and background. Therefore, the detection results of coal fires have to be assessed and quantified.

There are many factors that affect the detection of coal fires. For this study, the factors may generally be classified into three kinds and are discussed below.

### (1) The quality of raw data

The raw data is the basic data source for the detection of coal fires, errors will directly affect the detection result. The main raw data used for this study are space-borne images.

For the satellite remote sensing images, the errors can be briefly divided into two kinds of error, accidental error and systematic error. The latter one can be negligible in this accuracy assessment because their affections can be removed by means of some correction.

For this study, the factors causing the accidental error mainly include atmospheric radiance, climatologic condition, and etc. Besides, the location of the study area can also impact the quality of raw data, if the latitude is higher, the distortion on the image will be larger.

### (2) The errors in image processing

During pre-image processing, the original images have to be rectified onto a unique coordinate system. In this study, Landsat7 ETM+ and ASTER images were georeferenced to a UTM84 coordinate system based on the topographical map. The errors on topographical map and in the procedure of selecting ground control points (GCPs) on the images will influence the accuracy of the results.

For image enhancement techniques, one should be careful to use them because some will change the DN values on the image, such as brightness inversion, LUT stretch, and noise reduction. The change of DNs can impact the detection of coal fires from thermal infrared im-

ages, in which the statistical analysis of DN values will be carried out. Therefore, some image enhancement techniques are not suitable for thermal infrared images.

(3) The errors attributed by the method of detecting coal fire areas

The two methods of statistical analysis for the detection of coal fire areas from thermal infrared data were used in this study. There may be some errors produced during that analysis because of the size and location of selected sub-image, and some environmental noise, e.g. the thermal anomalies caused by non-coal fires. Hence, the identification for the detection results is necessary and important for the final results.

In order to assess the accuracy of the detection results of coal fire areas, the ground measurements are necessary to be used as “truth value”. Unfortunately, there is no accurate field data available for the accuracy assessment in this study. Hence, just the method of the accuracy assessment of the detection results of coal fire areas is discussed below.

Here, the approach of the accuracy assessment is performed in two steps. In the first step, the accuracy assessment for each site (sub-image) is applied. Then, the overall accuracy assessment for all detecting sites is carried out to obtain the assessment and confidence for the research work.

## **5.2 Assumption**

For the accuracy assessment of this research, some presumptions are given:

(1) The field temperature measurements can be used as the “truth value” during the accuracy assessment. In the area of each sub-image, the number of ground temperature measurements ( $N_g$ ) should be same or close to the number of DN values ( $N$ ).

(2) The ground temperature measurements and the calculation results of surface temperatures from space-borne remote sensed data used in the accuracy assessment are necessary to be acquired at the generally same time, the “time” means both the time of a day and the time of a year.

(3) In the temperature calculation from space-borne sensed data, the emissivity of ground materials is assumed as  $e = 0.97$ . The actual emissivity of local ground materials can be obtained using the method of temperature and emissivity separation (TES) mentioned in Chapter 2.3.

(4) In this study, for example, the detection results at the confidence level of 0.80 ( $P_i = 0.80$ ) are used for the accuracy assessment.

### 5.3 The approach of accuracy assessment for each site (sub-image)

The thermal anomalies caused by coal fires can be obtained by means of ground temperature measurements and the temperature calculation from the thermal infrared images, and they can be expressed as the following equations:

$$\Delta T_{gi} = T_{gmax} - T_{gi} \quad (5.1)$$

$$\Delta T_i = T_{max} - T_i \quad (5.2)$$

Where,  $\Delta T_{gi}$  = the thermal anomalies measured on the ground;

$T_{gmax}$  = the maximum value of ground temperature measurements;

$T_{gi}$  = the value of ground temperature measurements at point  $i$ ;

$\Delta T_i$  = the thermal anomalies obtained from the image;

$T_{max}$  = the maximum temperature value calculated from image;

$T_i$  = the temperature value calculated at pixel  $i$  on the image.

If the data were acquired at the same time and the affection caused by air and sensor itself had been corrected or removed in the temperature calculation from the sub-image, then,

$$\Delta T_{gi} = \Delta T_i \quad (5.3)$$

However, in fact, they are different because of the present of noise and errors. We can get the difference of thermal anomalies between which of the ground temperature measurements and of the temperature calculation from the sub-image. First, the mean values of thermal anomalies on the ground and on the sub-image can be calculated separately as following:

$$\Delta T_{gmi} = \frac{\sum_{i=1}^n \Delta T_{gi}}{n_{gi}} \quad (5.4)$$

$$\Delta T_{mi} = \frac{\sum_{i=1}^{n_i} \Delta T_i}{n_i} \quad (5.5)$$

and the difference of thermal anomalies mentioned above can be calculated as following:

$$\Delta T_i = T_{gmi} - T_{mi} \quad (5.6)$$

Where,  $\Delta T_i$  is the difference of thermal anomalies between which from ground temperature measurements and from the sub-image “i”. Then, it is assumed that if  $\Delta T_i < 0.20$ , the difference is acceptable, in other words, the area on that sub-image can be considered as the coal fire area. It can also be expressed as the way of probability as following,

$$P_i = 1 - \Delta T_i \quad (5.7)$$

Where,  $P_i$  is the result probability of the detection of coal fire area on each sub-image. If  $P_i = 0.80$ , then, the detected area will be defined as the coal fire area.

## 5.4 The overall accuracy assessment

After the accuracy assessment for each site performed, the overall accuracy assessment for the detection results of whole study area can be assessed based on the following equation:

$$P = N_t / N * 100\% \quad (5.8)$$

Where,  $N_t$  is the number of sites in which coal fire area is detected and identified there using above method ( $P_i = 0.80$ ),  $N$  is the number of potentially selected sites within the study area, and  $P$  is the percentage of accuracy for the detection of coal fire areas.

If the precise ground GPS points can be surveyed at each potential coal fire areas as the field temperature measuring, the method of statistical analysis can be used for the accuracy assessment. The root mean square (RMS) error can be obtained according to the following equations:

$$s = \frac{1}{n} \sum_{i=1}^n \sqrt{(T_{gi} - T_i)^2} \quad (5.9)$$

where,  $s$  = RMS error,

$n$  = number of sample points,

$T_{gi}$  = the temperature measured on the ground,

$T_i$  = the temperature calculated from the thermal infrared image.

## 5.5 The field data needed for the accuracy assessment

More field data is needed in order to performing a proper accuracy assessment. These data could not be used during this study because the author was not able to collect those in the field during satellite data acquisition. Aspects to be considered are:

(1) GPS points and DEM. Some accurate GPS points will be used as ground control points to optimize the results of image geometric correction and registration, and some of them will help to locate the position of coal fire area. The highest accuracy would be obtained if the image could be ortho-rectified. In order to do so, a DEM is needed.

(2) Temperature measurements. The ground temperatures in the area of coal fires and background have to be obtained. There are three methods used for field thermal measurements using three kinds of equipment, contact thermometer, pointing thermometer and thermal infrared frame scanner. Two sets of measurements have to be collected, one is for validation of image transformation, and the other is for validation of the transformed temperature image. For selection of the equipment also the pixel integrated temperature values obtained by satellite measurements have to be considered. Besides, these temperature measurements can also be used to obtain the accurate emissivity of coal fire areas by means of TES algorithm mentioned in Chapter 2.

(3) More accurate topographical maps (1:50,000) and elevation data. They can be used to generate a digital elevation model (DEM) with the help of ASTER data. The DEM will help to analyze and reduce the affect of solar heating so that the accuracy of detecting coal fires would be improved especially for daytime thermal recordings.

(4) Ground cover samples obtained are better to determine emissivity coefficients, which can improve the accuracy of temperature conversion.

(5) Data on temperature have to be collected during satellite overpass.

# Chapter 6 Conclusions and recommendations

## 6.1 Conclusions

### 1. The advantage of satellite remote sensing technique for the detection of coal fires.

Satellite remote sensing technique is an effective and economic way for the detection of coal fires, comparing to the borehole and geophysical methods (electrical and magnetic methods), whose shortcomings are slow, difficult to repeat, and costly to apply over a large area. However, the detection results from satellite imagery, due to the low spatial resolution of thermal infrared data, the effects of earth biosphere, lithosphere, atmosphere and hydrosphere, have to be identified and determined with the help of field temperature measurements and/or airborne remote sensed data.

With the development of space borne sensor technology, the spatial resolution of satellite imagery has improved greatly. For example, the sensor Quickbird2 was successfully launched on 18 October 2001. The imaging sensors are panchromatic and multispectral. The panchromatic, natural color, and color infrared versions of Orthorectified imagery are well suited for visual analysis and as a backdrop for GIS and mapping applications, while the multispectral version is well suited for image classification and analysis. The highest resolution available from the commercial satellite image (the ortho-rectified image), with the resolution of 65 cm for panchromatic, natural color and color infrared image, and 2.8 m for multispectral image, can be used to identify features, classify image data, and detect changes from recent global imagery. The interferometric synthetic aperture radar collection system provides a unique and complementary data source to Digital Globe's high-resolution satellite imagery from Quickbird, and the resolution of DEM is 1.25-2.5 m. In that case, the other input data needed for the detection of coal fires will be improved (URL3, 2002).

Incorporation of other satellite based thermal infrared images will also assist in the detection of coal fires. An example is the German Aerospace Center (DLR) Bi-spectral Infrared Detection (BIRD) small satellite which is a technology demonstrator of a new infrared push-broom sensors dedicated to the recognition and quantitative characterization of thermal processes on the Earth surface. The BIRD (launched in October, 2001) main sensor payload consists of a two-channel infrared Hot Spot Recognition Sensor system (HSRS) and a Wide-Angle Optoelectronic Stereo Scanner (WAOSS-B), their characteristics are given in Table 6.1. Some researchers study the detection of wildfires and coal fires using data obtained by this satellite.

**Table 6.1 The characteristics of BIRD sensors.**

	<b>WAOSS-B</b>	<b>HSRS</b>
Spectral bands	VIS: 600-670nm	MIR: 3.4-4.2 $\mu$ m
	NIR: 840-900nm	TIR: 8.5-9.3 $\mu$ m
Focal length	21.65mm	46.39mm
Field of view	50°	19°
f-number	2.8	2.0
Detector	CCD lines	CdHgTe Arrays
Detector cooling	Passive, 20°C	Stirling, 80-100 K
Pixel size	7 $\mu$ m $\times$ 7 $\mu$ m	30 $\mu$ m $\times$ 30 $\mu$ m
Pixel number	2880	2x512 staggered
Quantisation	11 bit	14 bit (for each exposure)
Ground pixel size	185m	370m
Sampling step	185m	185m
Swath width	533 km	190 km

More operational sensors provide a greater flexibility in obtaining data at proper recording times for coal fire detection purposes.

## **2. The advantage of ASTER data.**

The results of detecting coal fire areas derived from this study show that ASTER data, as satellite remote sensing data source with high spatial and spectral resolution, has many advantages in detecting and monitoring the hazards of coal fires. Its abundant electromagnetic spectral data, high spatial resolution and stereo visibility are a great asset. Besides, it is free to use and convenient to obtain for researchers who want to study the detection and for monitoring of the coal fire areas.

## **3. The comparison between Landsat7 ETM+ data and ASTER data.**

In this study it was difficult to compare ASTER and Landsat7 ETM+ data therein given the differences in acquisition time and season using a pixel-based approach. It demonstrates that through selection of proper thresholds the coal fire anomalies could be identified and a feature-based extraction could be successfully applied. Secondly given their different

spectral resolutions, and the fact that the temperature is a pixel-integrated phenomenon, feature-based extraction will be a more promising approach anyhow.

More research has to be focussed on the use of the SWIR-bands of ASTER and their suitability for coal fire anomaly extraction, especially because these bands have a higher spectral resolution (30m).

#### **4. The detection results are related to the size of sub-image.**

When analyzing the DN values of TIR data by means of statistical method, the results are closely corresponding to the size of analyzing area, namely sub-image. If the size is larger, the thermal anomalies are difficult to be identified because there are many factors to create noise for the detection of those thermal anomalies caused by coal fires, such as solar heating and other thermal sources not due to the coal fires. On the contrary, if the size of sub-image is too small, the number of DN values provided for analysis is relatively small, therefore, the statistical analysis results will lack reliability.

#### **5. The accuracy of geometric correction and registration affects the capability of detection of coal fires.**

Because coal fire areas sometimes have just a few pixels on the thermal images, although the root mean square (RMS) errors of each image was limited within 1 pixel during geometric correction, however, the precision of geometric correction and registration would be larger than 1 pixel, which means the error on the ground would be in the range of 80-100 m. For a more accurate detection of coal fire areas, some ground control points are necessary to be measured in the field, such as precise GPS control points. Recommended is a combination of GPS control points together with a topographical map at large scale (1:5,000).

## **6.2 Recommendations**

1. In this study, the feature extraction of coal fire areas was carried out artificially, and ASTER band 4 to band9 were seldom used, which include more details about geology. In order to increase the efficiency and objectivity, the method of image computerized recognition and unsupervised classification need to be further studied.
2. The correction method of solar radiant affects in detecting the coal fire areas has to be studied further.

3. A disadvantage in this study is that there is no ASTER TIR data acquired at nighttime or predawn used for the detection of coal fire areas. Using nighttime thermal data can effectively reduce the affect of solar heating and make the results more reliable.
4. Creating a DEM from ASTER data has not been done due to the absence of field control data and more accurate topographical data, otherwise, the affect of solar heating would be corrected for by subtracting the thermal anomalies caused by solar heating, which can be calculated based on the DEM.
5. If the atmospheric correction is inaccurate, the residual affects can degrade the detection of coal fires, because these will affect the DN values on the image, hence, also affect the detection of thermal anomalies caused by coal fires. ASTER band 10 is more affected by atmospheric absorption and emission than the other ASTER TIR bands, because band 10 is located closest to the edge of the TIR atmospheric window. Therefore, it is suggested that ASTER TIR band12, band13, and band14 are used in the statistical analysis to get better detection results.
6. ASTER optical high spectral resolution bands are suitable for land cover characterization and classification and can therefore assist in obtaining the necessary information, which can be used for correction of the thermal data by assigning appropriate emissivity values and therefore improve the temperature calculation accuracies.

## References

- Bhattacharya, A. and Reddy, C.S.S., 1994, Underground and surface coal mine fire detection in India's Jharia coal field using airborne thermal infrared data. *Asian-Pacific Remote Sensing Journal*, Vol.7, No.1, pp.59-73.
- DMT, 2001, Studie zur Erarbeitung von Strategien zur Loschung von Kohlebränden in der VR China, pp.17-19.
- Earth Remote Sensing Data Analysis Center (ERSDAC), 2001, ASTER User's Guide.
- ERDAS IMAGINE Tour Guides, Copyright (c) 1991-1999 by ERDAS, Inc.
- Genderen, J.L.van and Guan, H.Y., 1997, Environmental Monitoring of Spontaneous Combustion In The North China Coalfields, pp. 5, pp. 24.
- Gillespie, A., Rokugawa, S., Matsunaga, T., Cothorn, J.S., Hook, S. and Kahle, A.B., 1998, A Temperature and Emissivity Separation Algorithm for Advanced Spaceborne Thermal Emission and Reflection Radiometer (ASTER) Images.
- Gillespie, A.R., Rokugawa, S., Hook, S.J., Matsunaga, T. and Kahle, A.B., 1999, Temperature /Emissivity Separation Algorithm Theoretical Basis Document, *Version 2.4*.
- Greene, G.W. and Moxham, R.M., 1969, Aerial infrared surveys and borehole temperature measurements of coal mine fires in Pennsylvania, *Proceeding of the 6th ERIM Symposium on Remote Sensing of Environment*, University of Michigan, Oct. 13-16, 517-525.
- Guan, H.Y., 1963, On the Yaojie burnt rocks, pp. 212 (in Chinese).
- Gupta, P., 1991, Remote Sensing Geology, *Springer-Verlag, Berlin*.
- Kahle, A.B., 1980, Surface thermal properties. *Remote Sensing in Geology*, edited by B.S. Siegal and A.R.Gillespie, Wiley, New York, pp.257-273, 1991, The Advanced Spaceborne thermal emission and reflectance radiometer (ASTER), *International Journal of Imaging Systems and Technology*, Vol. 3, pp. 144-156.
- Kahle, A.B. and Alley, R.E., 1992, Separation of Temperature and Emittance in Remotely Sensed Radiance Measurements.
- Klein, R., 1993, Sensor and Data Fusion Concepts and Applications.
- Lillesand, T. M. and Kiefer, R. W., 2000, Remote Sensing and Image Interpretation, pp. 361, pp. 335-336, pp.533-535.
- Mansor, S.B., Cracknell, A.P., Shillin, B.V. and Gornyi, V.I., 1994, Monitoring of underground coal fires using thermal infrared data, *International Journal of Remote Sensing*, pp.1675-1685.
- Prakash, A., Remote Sensing-GIS Based Geoenvironmental Studies In Jharia Coalfield, India, With Special Reference To Coalmine Fires, *PhD. Thesis*, 1996.
- Reddy, C.S.S., Srivastav, S.K. and Bhattacharya, A., 1993, Application of thematic mapper short wavelength infrared data for the detection and monitoring of high temperature related geo-environmental features, *International Journal of Remote Sensing*, Vol. 14, pp.3125- 3132.
- Robinson, A.M., 1991, Fire from space: Global fire evaluation using infrared remote sensing, *International Journal of Remote Sensing*, Vol.12, No.12, 3-24.
- Rosema, A., Guan, H.Y., Veld, H., Vekerdy,Z., Ten Katen, A.M., Prakash, A., 1999, Manual of Coal Fire Detection and Monitoring, pp. 61, pp.143, pp. 203, pp. 210-211.
- Saraf, A.K., Prakash, A., Sengupta, S. and Gupta, P., 1995, Landsat TM data for estimating ground

temperature and depth of subsurface coal fire in Jharia coalfield, India. *International Journal of Remote Sensing*, 16, pp.2111-2124.

Schmugge, T., French, A., Ritchie, J. and Rango, A., 1998, The Use of Multispectral TIR Data for Observing the Spectral Emissivity of Arid Lands.

URL-1 : <http://www.xj.cninfo.net/new/20020215/default.htm> (in Chinese).

URL-2:[http://ltpwww.gsfc.nasa.gov/IAS/handbook/handbook\\_htmls/chapter11/chapter11.html](http://ltpwww.gsfc.nasa.gov/IAS/handbook/handbook_htmls/chapter11/chapter11.html).

URL3:<http://spacesensors.dlr.de/SE/bird/>.

Watson, K., 1992, Two Temperature Method for Measuring Emissivity.

Yamaguchi, Y., Kahle, A.B., Tsu, H., Kawakami, T., and Pniel, M., 1998, Overview of Advanced Spaceborne Thermal Emission and Reflection Radiometer (ASTER).

Zhang, X.M., Coal Fires In Northwest China, Detection, Monitoring, and Prediction Using Remote Sensing Data, 1998, *ITC PhD. thesis*, pp. 1-3, pp.69-70, pp. 113.